JRORS
JOURNAL OF RADAR AND
OPTICAL REMOTE SENSING

Analyzing and Evaluating the Agricultural and Garden Land Areas, and the Land Use Changes using RS and GIS Technology

Using Discrete Wavelet Transform to increase the Accuracy of Hyper Spectral and High Resolution Images Fusion

Inventory of Single Oak Trees Using Object-Based Method on WorldView-2 Satellite Images and Earth

Detecting and Calculating the Soil Moisture Using Microwave Imagery (Case Study: Miyankale, Mazandaran

Rockfall Detection Using Differential Interference Synthetic Radar Technique from Sentinel-1 Satellite Imagery (Case study: Haraz road)

Quantifying Geotechnical Changes in the Rafsanjan Plain in Time Series and Finding OutTheirCauses Using Radar Remote Sensing Techniques

Journal of Radar and Optical Remote Sensing

Permission to publish Journal of Radar and Optical Remote Sensing

With respect to the Reference Number: **96/ص/87/7**dated 1396/01/14(3th April 2017), the 104th commission session was held to evaluate and approve the scientific journal of the Islamic Azad University. The commission announced to grant permission to establish the journal entitled "Journal of Radar and Optical Remote Sensing".

Acknowledgement
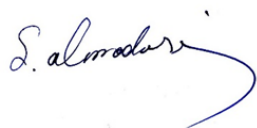
<div align="center">In the Name of God</div>

Dear Readers,

I have the enormous opportunity to share the first journal publication to the readers. The Journal of Radar and Optical Remote Sensing (JRORS) is the first radar journal and the first scientific journal in this area of Islamic Azad University (2017). The first issue will be published this year by the Islamic Azad University, Yazd Branch. The publication of the articles resulting from the scholarly research findings contributes to the advancement of knowledge and performance of remote sensing and radar. This journal focuses on original research papers that develop a basic knowledge in the field of remote sensing and radar.

Over the past years, many research articles have been received in the specialized field and just a few have been accepted for publication in each issue based on the reviewers' and the editorial team's decisions regarding the articles. This has somehow upset the authors. Therefore, an apology on behalf of the editorial team for declining and or delaying the publication of some of these inter-disciplinary scholarly articles. It is hoped to add the scientific richness of the journal by releasing articles that reflect your valuable research activities, providing us with the latest publications in the scientific community of remote sensing and radar.

Finally, I would like to sincerely thank the Editorial Board for their dedication to prepare the first issue. It was their efforts that made it possible to publish the first issue on time.

Sincerely,

Dr. Seyyed Ali Almodaresi

Editor-in-Chief

Journal of Radar and Optical Remote Sensing

www.jrors. ir

INDEX

Analyzing and Evaluating the Agricultural and Garden Land Areas, and the Land Use Changes using RS and GIS Technology

Reyhaneh Bahador[a*], Seyyed Zein-al Abedin Hosseini[b]

[a]* MSc. Student in Remote Sensing and Geographic Information System, Civil Group, Yazd Branch, Islamic Azad University, Yazd, Iran
[b] PhD in Geomorphology, Assistant Professor of Remote Sensing and GIS Group, Yazd Branch, Islamic Azad University, Yazd, Iran

Abstract

Estimating and determining the area under cultivation of agricultural products are among the important aspects in planning and decisions making. Remote sensing data can provide useful information in this regard to agricultural experts by identifying the type and determining the crop area. In this research, agricultural land and garden areas as well as the land use changes were evaluated by using Quickbird and Landsat images for 1984, 2003 and 2015 in Rudasht basin of Esfahan. The required preprocessing was done on the images and then, the educational samples were taken using GPS for classification by the maximum likelihood method and verifying the classification. The geometric correction results for 1984 and 2003 images with acceptable RMSE were 0.48 and 0.42 respectively. The image classification results of Landsat showed that the agricultural land and gardens areas are reduced by 1036.236 and 27.3146 hectares from 1984 to 2015, and Quickbird images showed the reduction of 1036.236 and 119.8833 hectares from 2003 to 2015. In estimating the Quickbird classification error for 2003 and 2015, the Kappa coefficient of maximum likelihood was 0.8576 and 0.8643 and for the years 1984 and 2015 were 0.7967 and 0.8641 respectively.

---

* Corresponding author. Tel: +98-9133333060.
Email address: reyhanebahador@gmail.com.

1. Introduction

Development of science and technology in all the domains has reduced the rate of the required activities, and from the other side, it has led to the increasing accuracy and speed of various studies. One of the most important achievements by humans has been using satellite images in all the scientific researches. Regarding their exclusive features, the use of satellite images have been considered as an appropriate tool in evaluating, analyzing, controlling and managing of soil and water resources. Such images are extensively used nowadays in different agricultural and natural resource studies and also in preparing various drawings and maps. Thus, the researchers have analyzed various observations and collected information via the field studies and satellite pictures of the past decades for finding the changes in land use due to the imposing natural and human processes. Based on the technological developments in the domain of remote sensing, the satellite images can nowadays be processed in the shortest time for more precise analysis of the environmental changes, and the final results can be modeled by illustrations. The rate of the related information is rapidly increasing by the satellite images, and many organizations and institutes are trying to utilize such images for their various aims. In this regard, preparing quality satellite images and processing these images are considered as the first step for the process. After selecting appropriate images, a suitable method of classification would be selected. The accuracy of the required data would be evaluated after the classification and determining the cultivated area with the real and received land data by GPS. In this study, the agricultural and garden areas are analyzed and determined by using the classification method of maximum likelihood and the Landsat and Quickbird images, with regards to the high potentials of the satellite images and remote sensing technology and the considered area for the study is Rudasht basin in Esfahan.

Various studies have been done both in Iran and all over the world about using remote sensing technology and satellite images. Bakhtiarifar et al. (2011) have done a research about the model development based on GIS and multi-criteria decision-making method for evaluating and identifying the existing conditions of the land uses, and also about the changes in the land use with difficulties to appropriate uses. The results indicated that proper considerations and simultaneous compatibility of the land uses are essential in allocating the land uses. In a study, Givi Ashraf and Ardakani (2011) analyzed the land use for evaluating the desertification in Marvast plain/Yazd province by using Landsat-7 images and ETM+ (Enhanced Thematic Mapper) measurement related to 2002 and 2010. The results of the research showed that the desert lands in Marvast, which are among the dry and semi-dry regions, has increased by 30% in the 8-year period, and the wet desert has decreased about 50%. Javanmardi et al. (2011) evaluated combined process of potential production and land proportions for various purposes. Then, the obtained results were compared with the results from the evaluation with the combined technique of the process of hierarchical analysis and GIS. The results indicated the existence levels of land use in the studied region, in which the 5th class with the area of 31% includes most of the area in the region. Zangiabadi and Abolhassani (2012) did a study with the aim to evaluate the management of agricultural lands by utilizing GIS and RS in a descriptive-analytical basis in Esfahan province. The results of this study indicated that the province cities are classified in four different levels with regards to the agricultural areas, in which the city of Esfahan is in the first level, and the cities of Naein, Khomeinishahr, Khansar, and Lenjan are in the fourth level, and the other cities are placed in between the cities of Esfahan and Naein. In a research, Pakpour Rabti (2013) evaluated the susceptible lands for cultivation of corn, barley, and sunflower products in Posveh and Jaldian regions in West Azerbaijan. The results showed that climatic class in the studied area for the barley was properly appropriate (considered as S1) and it was moderate (S2) for corn and sunflower due to the relative humidity limitation during the growth period. In other words, using GIS in the studies for the land proportions increases the accuracy and progress of the research. In a research Arkhi (2014) dealt with controlling the changes in land use in the past and considered the possibility of estimations for the future by using the land change modeler (LCM), the aid of Landsat-4 images (mapped ,1967), Landsat-7 ETM+ (1991) and Landsat-5 (2011) in Sarableh in Elam province. The modeling results of the transmission power by the artificial neural network showed a high rate of correctness (60-86%) in most of the sub-models. The total error in the modeling was 12.84% for 2011, indicating the high rate of conformity of the model predicted image with the land real image, which was acceptable. Pilehforoushha et al. (2014) presented a model for planning about the allocation of agricultural lands to for the best land uses by using calculation of inferring systems on the fuzzy basis, determining the demands and considering the sequence of cultivations. The results

showed that, the most appropriate product for cultivation in a definite area can be determined and useful information can be provided for the agricultural planners by using different scenarios. In another research, Davoodi Monazam et al. (2014) evaluated the change in the farm land usage in the city of Shahriar by three different methods of maximum likelihood classification (MLC), neural network classification (NNC), and supporting vector machine (SVM) in 1987-2009, by using Landsat data. Results showed that the urban development in the considered 22-year period had an increasing trend, while the agricultural lands had a decreasing trend. Moradi et al. (2016) compared the pasture land use change with the places where dry farming is done in the cities of Rabar and Arzoueieh, for a period of 15-year. The of land use change trend in the study area by (Dehsard and Kouh Sefid) was processed by the Landsat ETM+ (2000) and OLI (2014) images in the ENVI 5 software, using supervised classification. The results of the research showed that the expansion of farming activities on the pasture ecosystems transform the pastures to low efficiency lands of 9% and 20% in Dehsard and Kouh Sefid regions, respectively. Mullupattue and Sreenivasula Reddy (2013) analyzed the change in the land use using GIS in Tiropatty region in India with regards to topographic drawings and remote sensing data from LISS III, PAN, and IRSID in 2003. According to the results, reducing the water resources and agricultural lands, and destruction of forests are among the lateral effects of land use changes with regards to the accelerated trend in urbanization. Butt el al. (2015) studied the algorithm of supervised classification of maximum likelihood to identify the changes in the land use in Simley region in Pakistan, by using multi-dimensional images of Landsat-5 and Spot-5 for the years 1992-2012. The overlap of maps and drawings in Arc GIS showed the change in the land use of aquatic and plant coverage of the region towards farming and deserted lands with 74.3% and 38.2% ratios, respectively, which is a great threat for the environment. Hegazi and Kaloop (2015) analyzed the change in land use as one of the most important management cases in managing the natural resources of Egypt by using the Markov chain. The growth of urbanization in Egypt has decreased the air quality, increased the flood waters, landslide, and contamination of water resources. Changing the land use in the above mentioned cities in 1985-2010 has increased urban constructions from 28 km^2 to 255 km^2, causing a 40% reduction in agricultural lands. The results can be used by the city authorities for the sustainable development of the considered cities. The main aim of the study by Cheruto et al. (2016) was the quantitative perception of the change in land uses in Makoni region in Kenya for the years 2000-2016. The classification was fulfilled by the algorithm of maximum likelihood and the ERDAS images. The used images were received from Landsat-7 in the years 2000 and 2015-2016, and the considered area was divided into 7 sections with regards to the change in the land use, including farms, aquatic resources, forests, bushes, greenswards, and deserted lands. The results showed important changes in the land use in 2000-2016 for the mentioned area.

2. Materials and methods

2.1. Introducing the studied region

The studied area is Rudasht basin in Esfahan province. which is located in the southeast of Esfahan, in Central Iran, consisting of the two sections of north and south in the end part of Zayandeh Roud basin next to Gavkhoni lagoon. The geometrical coordinates of it are 52°-53° 52' E and 20°-34° 32' N, and the studied area of Rudasht basin is located in the altitude range of 1431.76-1538.04 m, as shown in Figures 1 and 2. Thus, it is rather a high land with regard to its altitude.
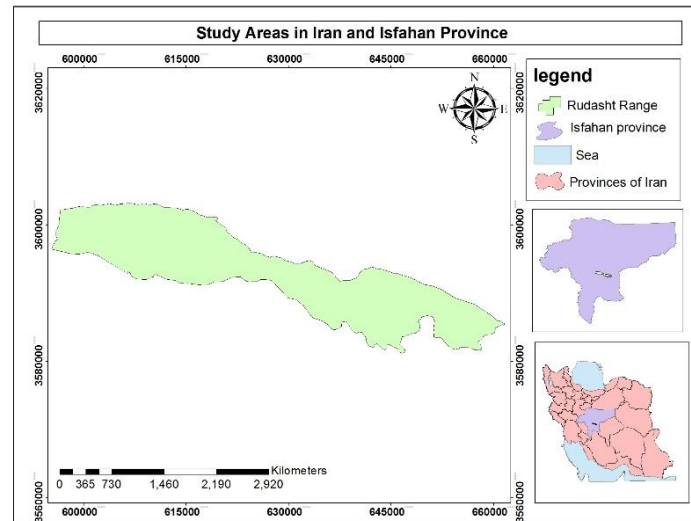
Figure 1. View of the studied area in Iran and Esfahan province.

Figure 2. View of the studied area by Google Earth.

2.2. Methodology

   The considered images are Landsat for the years 1984 and 2015 and Quickbird related to 2013 and 2015. The following stages were done for the study:

2.2.1. Geometric correction

   Geometric errors cause displacements, deformations, and change of situations on the images. Hence, it is required that the errors to be removed from the images or at least reduced.

2.2.1.1.Method of geometric correction of the images used in this study

a) Selection of benchmarks on the map and determining them on the images – At this stage, the benchmarks are determined on the satellite images, the selected points are specified at places that can easily be

identified, and also the density of points in the whole image is homogeneous. The unknowns of the models should be solved by using the land benchmarks for the relationship between the image coordinate system and the land.

b) Determining the coordinates of the benchmarks in the image and land systems – The land benchmarks are taken by GPS receivers. The benchmark coordinates on the image are also determined by the row and column coordinates.

c) Determining the transformation model and analyses of the errors and RMSE – At this stage, using ENVI software, the benchmarks are used as Ground Control Points or Check points. the check points are considered to analyze the errors, regarding the number of taken points and a fifth of them in scattered form are introduced as the check points in the software. Finally, the model remaining errors and the check point error will be obtained for the geometric corrections.

d) Calculating and finding the unknown parameters of the model – After introducing the benchmarks to the image, the software will calculate the unknown parameters of the model, and since the equations are cubic, there will be 20 unknown parameters.

e) Creating a new network of the pixels, and resampling – The simpler the sampling method, the image will encounter less distortion. "Nearest" method is used in this project that is the simplest method of resampling.

2.2.2.Creating the colored images: Combination of colors (237 and 123, 246 and 123) for the images in 1984, 2003 and 2015, and the agricultural lands with regards to its exclusive features could clearly be distinguished.

2.2.3.Image classification:

a) Identifying the existing land uses in the region – With regards to the identification of the region, analyzing the existing land uses in the area, and using the maps of the Agricultural Organization and the topographic maps (1:50000) of the Geographic Organization of the Armed Forces and related specialists, the required field analyses, assessing fallows, man-made locations, gardens, deserted lands, rivers, green areas and agricultural areas in the region are considered.

b) Selecting the classification method – Analysis pixel base-image is used in this regard; a classic method in classification of appropriate satellite images with the spectral data of the image that is in pixel-pixel form, in which each pixel can be allocated to a class. Classification of the base pixel can be done in supervised and unsupervised classifications. "Maximum likelihood" is considered so far as the most accurate and mostly used method among the supervised classification methods, which is used in this research. Maximum likelihood method evaluates the variance, and covariance of the classes. Thus, it is assumed that all the educational regions have normal transmittal. In fact, the samples of the educational classes should define the classes. Hence, as many as possible samples were used in this study in order to observe considerable changes of the spectral features in this respect.

2.2.4. Evaluation of the classification accuracy, obtained by the general accuracy and Kappa coefficient – General accuracy is a mean of classification accuracy, showing the ratio of the classified correct pixels to the total of the definite ones. Kappa coefficient calculates the classification relative to a quite random classification. Kappa coefficient has this advantage as compared to the general accuracy that uses the non-diagonal elements of the error matrix for the calculation of accuracy.

2.3. Implementation

Some benchmarks were selected by GPS for the geometric correction of the images. No correction was done on the images of 2015 due to proper conformity of the images with the road maps of the surveying organization. The results of the geometric corrections of the used images in this study were such that the

rates of RMSE for the images of 1984 and 2003 were obtained to be 0.48 and 0.42, respectively, as shown in Figures 3 and 4 as georeferenced images.
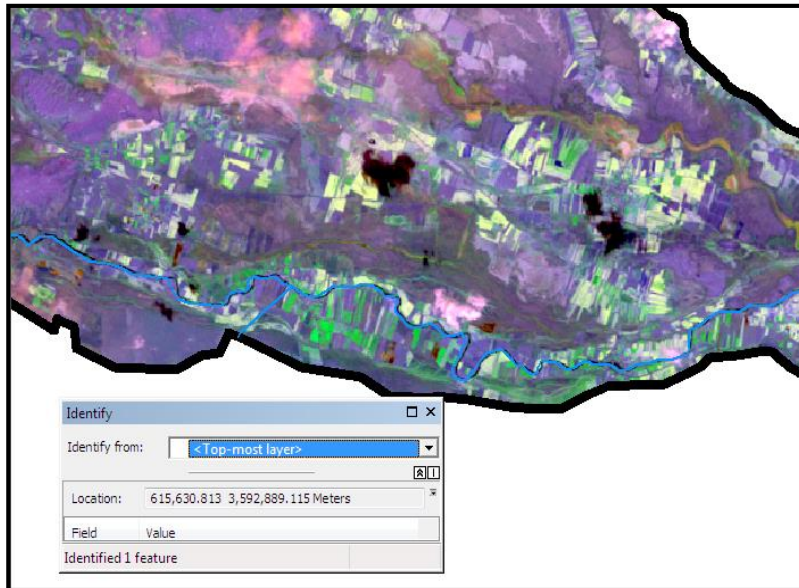
Figure 3. A view of the conformity of the image of the aphorisms with the image having coordinates by Landsat (1984)
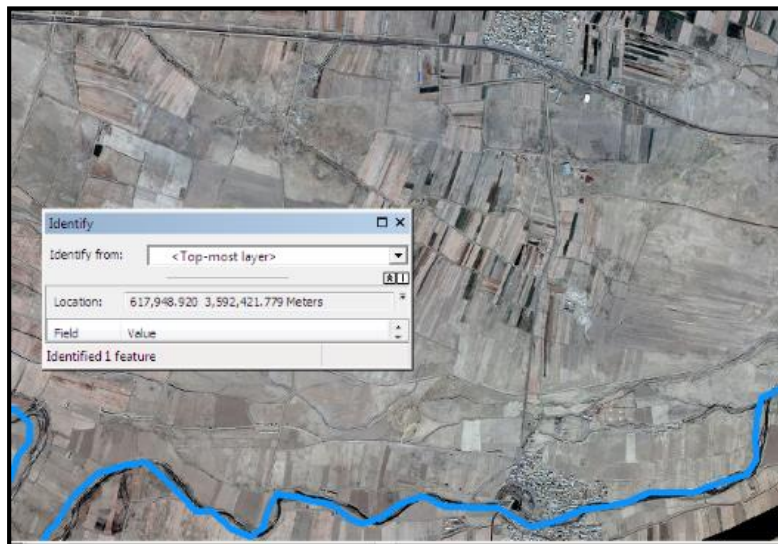
Figure 4. A view of the conformity of the image of the aphorisms with the image having coordinates by Quickbird (2003)

Among the colored images used by the combination of colors, by which the agricultural lands were quite distinguishable, were the combination of the colors (237 and 123, 246 and 123) in this study for the images taken in 1984, 2003 and 2015, as shown in Figures 5, 6, and 7.
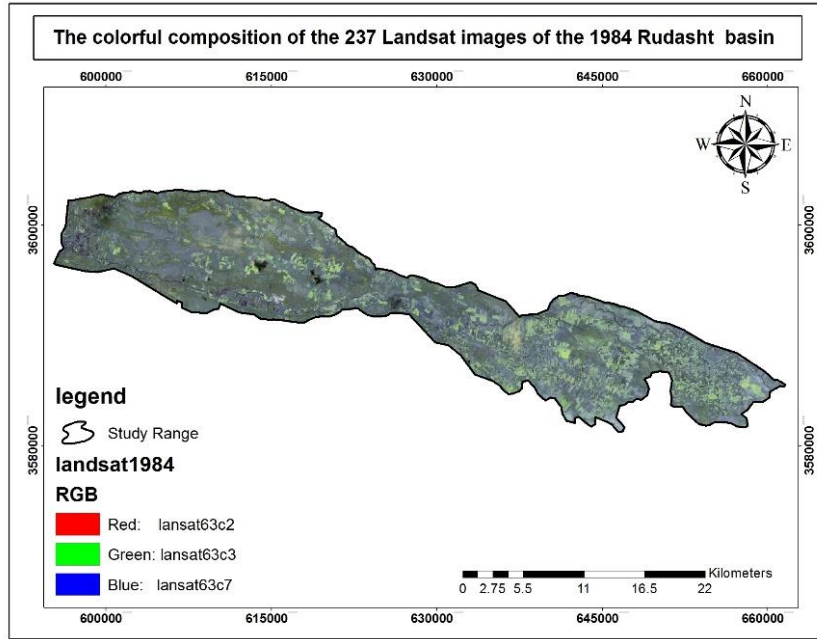
Figure 5. Color combination (237) in 1984 by Landsat
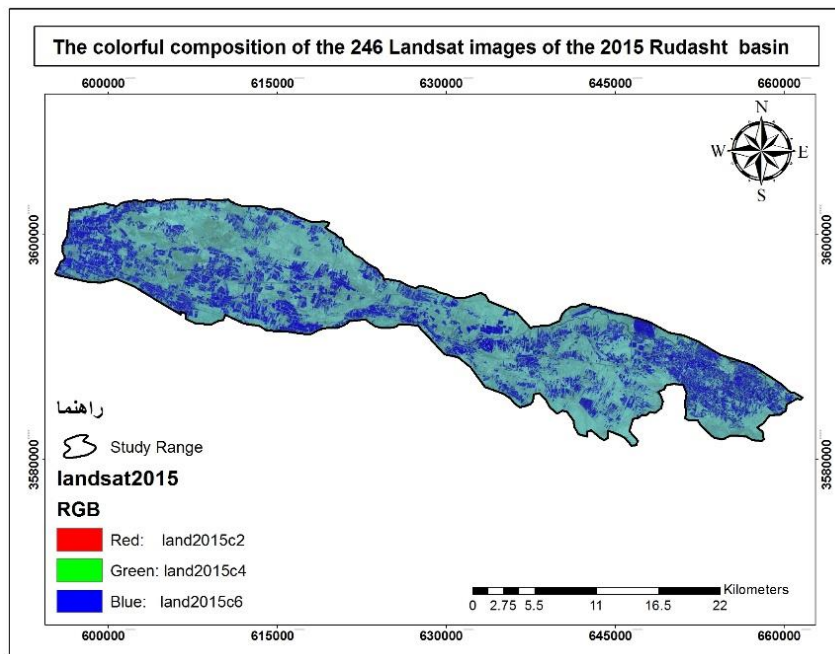
Figure 6. Color combination (246) in 2015 by Landsat
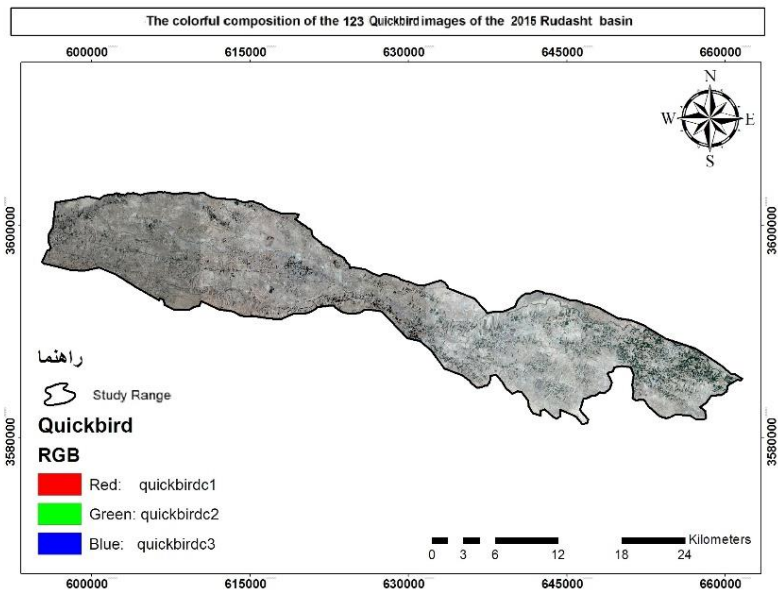
Figure 7. Color combination (123) in 2015 by Quickbird satellite

For the image of the studied area, the land use classes were defined according to the field visits and the experts' viewpoints. The land use classes included fallow land, man-made regions, gardens, deserts, rivers, green areas, and agricultural areas, the land use images of which for the years 1984, 2003, and 2015 were prepared with the maximum likelihood method, as shown in Figures 8 and 9.
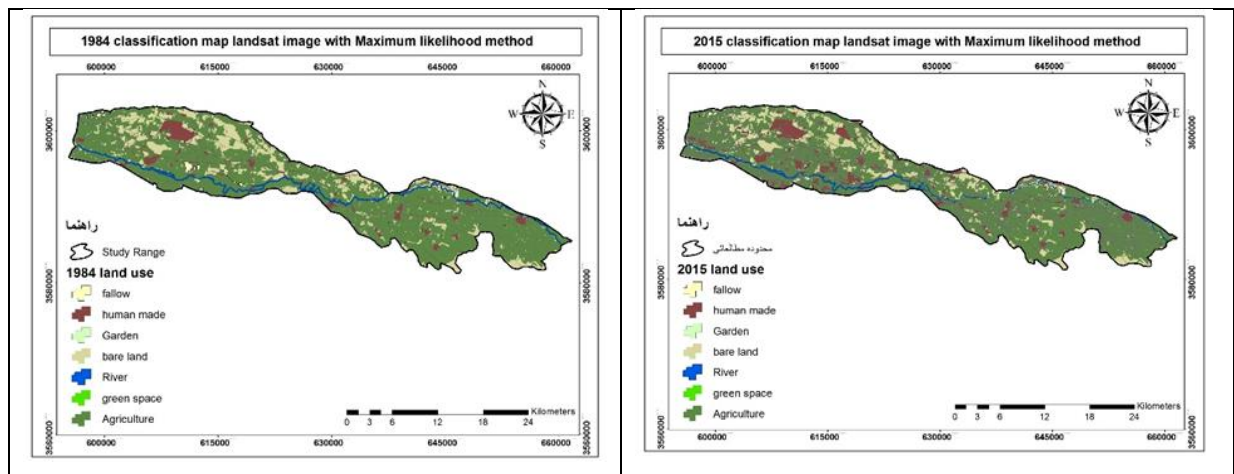
Figure 8. Classification image for 1984 and 2015 by Landsat, by maximum likelihood classification method
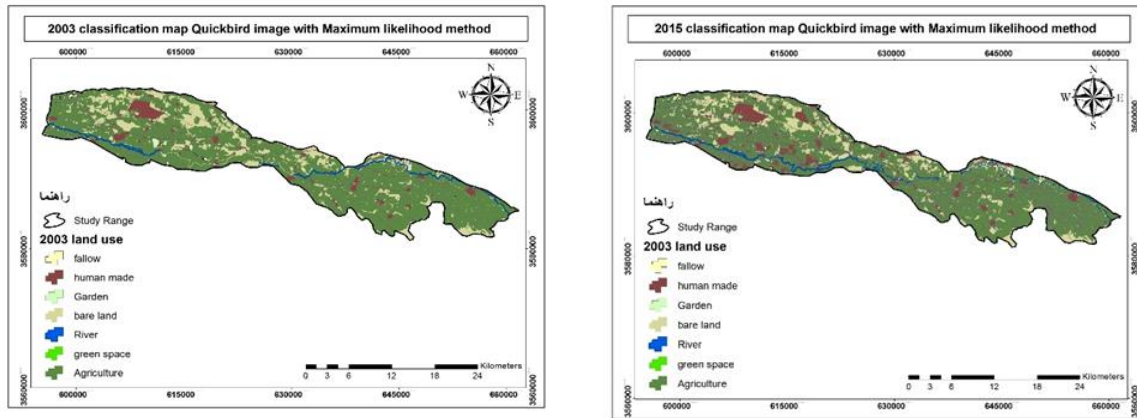
Figure 9.classification image for 2003 and 2015 by quickbird, by maximum likelihood classification method

3. Results and discussion

The Landsat and Quick bird images with the resolutions of 30 m and 2.5 m were used in this study. The required preprocesses were first done on the images, and after creating the color composition, the images for the years 1984 and 2015 were classified, and then the agricultural lands were specified. After that, the agricultural lands in the images of the studied periods were separated by the classification method and their cultivated areas were calculated. The results for the areas under cultivation of the remote sensing technique were compared with the results for the cultivated areas received by the agricultural organization and the results were considered as follows:

3.1. Analyzing the changes in the levels of land uses

After the classification of the images, the required information was entered in the GIS system, the areas of the land uses were calculated, and the changes were specified, as shown in Table 1. The rates of land use for 2003 and 2015 are shown in Graphs 1 and 2.

Table 1. Area and the changes in the land use levels according to Landsat and Quick bird images

No.	Land use	Area of land uses: Landsat 1984 (Hectare)	Area of land uses: Landsat (Hectare)	Changes in the levels 1984-2015: Landsat images (Hectare)	Changes in the levels 2003: Quickbird images (Hectare)	Changes in the levels 2015: Quickbird images (Hectare)	Changes in the levels 2003-2015: Quickbird images (Hectare)
1	Man-made	6641.3009	8390.7961	1749.5	6634.0292	8424.4121	1790.38
2	Agricultural	34043.2366	33004.7544	-1038.482	34017.0504	32980.8141	-1036.236
3	Deserted	7700.1049	7285.5078	-414.5971	7893.1654	7280.4672	-612.6982
4	River	574.114	574.114	-	388.3252	574.114	185.789
5	Green area	9.4789	8.234	-1.2449	35.6651	8.234	-27.4311
6	Fallow	453.9372	218.126	-322.7347	300.5869	224.2741	-180.3844
7	Garden	190.807	131.2025	27.3146	344.1574	120.2025	-119.8833
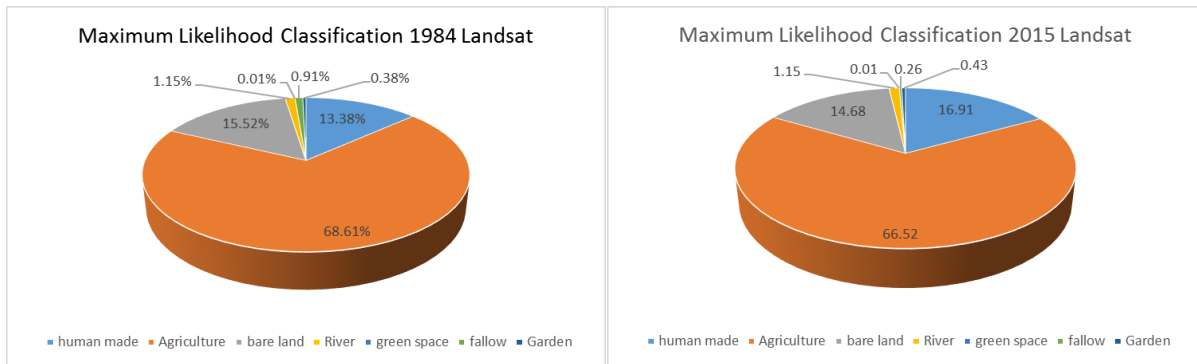
Graph 1. Classification of maximum likelihood – by Landsat images
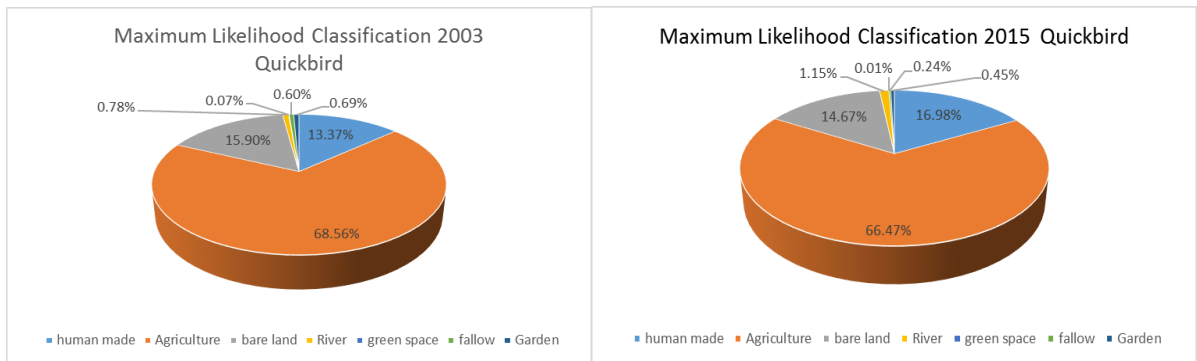
Graph 2. Classification of maximum likelihood – by Quickbird images

By analyzing the changes of the agricultural area in Rudasht region by Quickbird images from 2003 to 2015, the reducing trend with 1036.236 hectares and by Landsat images from 1884 to 2015 and the reduction by 1038.482 hectares have been observed while the lands with man-made constructions have always increased. The deserted and man-made lands have increased due to the reduction of agricultural lands (Table1).

3.2.Identifying all the agricultural lands and gardens in the studied area

After putting the satellite images and the required data in GIS software, processing, interpreting, and classifying of the images identified the agricultural lands and gardens will be done. At this stage, the agricultural lands were separated in the classified images for their areas to be determined out of the whole studied area within the studied period. The changes of agricultural lands and gardens are shown in Table 2. The areas of the agricultural lands and gardens are determined in Graphs 3 and 4.

Table 2. Changes of the agricultural lands and gardens in the studied period

Images	Area of agricultural lands	Garden areas
Classification of maximum likelihood: Landsat (1984)	34034.2346	190807
Classification of maximum likelihood: Quickbird (2003)	34017.0504	344.1574
Classification of maximum likelihood: Landsat (2015)	33004.7544	218.1216
Classification of maximum likelihood: Quickbird (2015)	32980.8141	224.2741
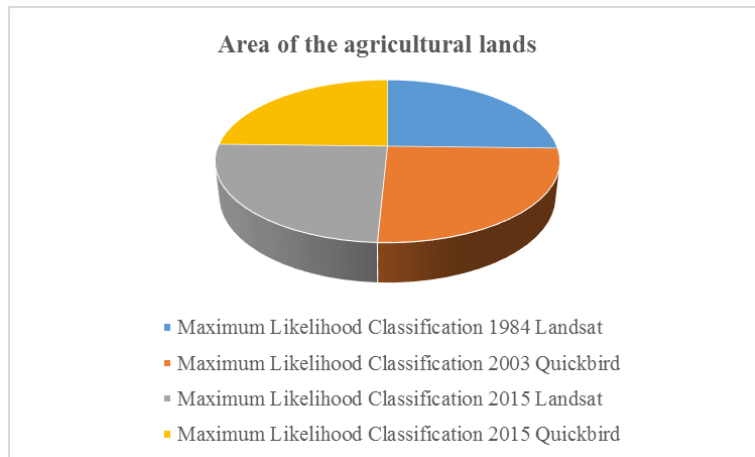
Graph 3. Area of the agricultural lands in the studied area
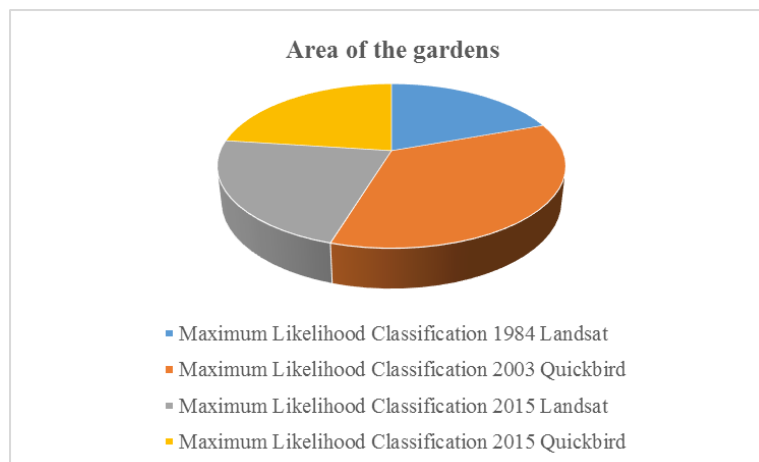
Graph 4. Area of the gardens in the studied area

3.3.Evaluation of the classification accuracy

   The prepared land use maps were compared with the GPS points and the existing situation of the region, and the Kappa coefficient as well as the general accuracy were obtained by using the matrix for the established error. Kappa coefficient and the general accuracy are acceptable in case they have a rate of over 70%. Otherwise, the classified points should be reclassified by new GCP, and the new Kappa coefficient and the general accuracy should be recalculated.
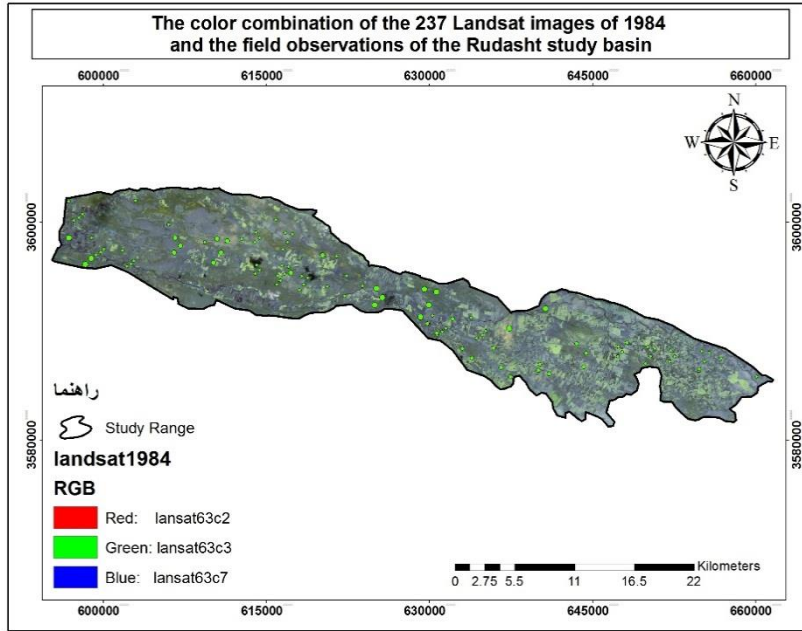
Figure. 10. Satellite image of the studied area and the taken GPS points
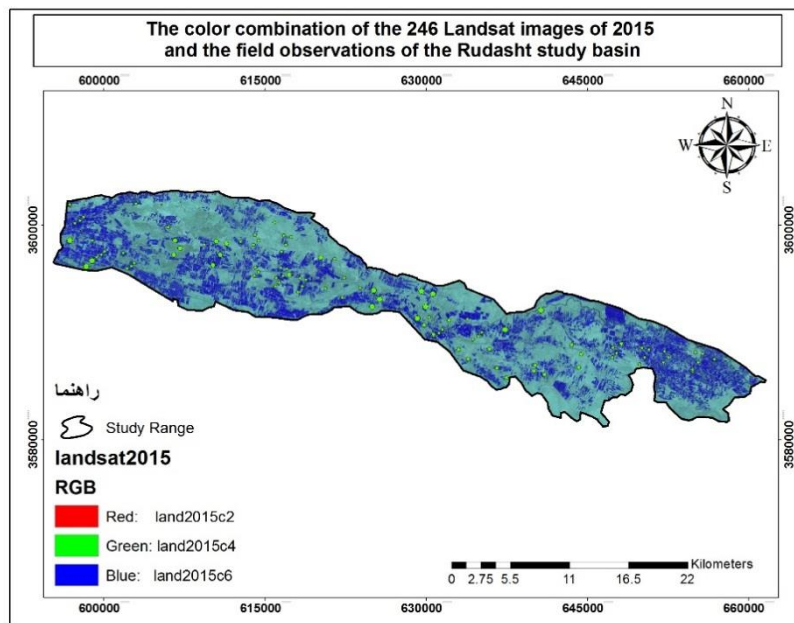
Figure 11. Satellite image of the studied area and the taken GPS points

Table 3. Kappa coefficient and the general accuracy of the land uses by separate satellites in the classification of maximum likelihood

Statistical parameter	Landsat 1984	Landsat 2015	Quickbird 2003	Quickbird 2015
Kappa coefficient	0.7967	0.8461	0.8576	0.8643
General accuracy	0.8461	0.8881	0.8709	0.8911

3. Conclusion

Preparing the land coverage maps is essential in natural resources and environmental management to study the plans for the land, identifying the capacity of the lands, and it is considered as an important information source for making principle decisions and organizing the developing programs. Preparing the land use drawings in intermediate scale from different regions without field techniques and interpretation of aerial photos is costly and time consuming, due to the wide areas of lands and impracticable passages. Since the type of land usage and coverage in the basin area are among the important features, precise determination of it as a management parameter can aid the planners in different executing sections in managing and developing water resources in the basin area. Regarding the spectral similarity of the phenomena and the unevenness of such regions, the spectral information cannot only be adequate for the classifications and precise distinguishing of different classes.

After applying the geometric corrections, different controlling technics were used for the changes. Analyzing the geometric quality of images used in this study showed that the images have appropriate quality. Proper conformity of the leveled roads and water ways on the geometric corrected images indicated the proper capability of the method of benchmarking the land for correcting the images. The geometric correction results of the 1984 and 2003 images with the RMSE for both images were obtained 0.48 and 0.42, respectively that were in conformity with the research by Weng et al. (2002) who did the geometric correction of the images by Landsat-TM by using the topographic images (1:50000) to analyze the change in the land use in Zhujiang Delta in China, reporting the rate of RMSE of three images in 1989, 1994, and 1997 to be 0.73, 0.62, and 0.58 pixels, respectively, and also with the studies by Khodakarami and Sefianian (2012), Arkhi (2014), and Moradi et al. (2016). The rates of RMSE of greater than "1" pixel for clear changes lead to higher or lower estimations than the real rate of changes. Generally, the results obtained from this study have been compatible with the obtained results by Hosseini et al. (2016), Mullupttue (2013), and Cheruto et al. (2016).

By the obtained results from the error matrix for the max. likelihood method, it can be observed that this method has high accuracy, which is indicated in Tables 2 and 3, and the optimized performance of it depends on the educational data and their normal distribution. The results from the supervised classification, which is introduced according to the educational samples and from different compacted levels with appropriate dispersion in the region, showed that the accuracy of each level was acceptable in the supervise classification, but the accuracy in all the land uses was obtained to be 75%. It can generally be said that the accuracy of the classified methods was appropriate in all the studied years. Darvishsefat et al. (1997) stated that if the region is rather even and has less unevenness, the rate of accuracy of the used methods will be increased.

Revealing the changes is one of the common applications of remote sensing, which has various technics to execute it. Selecting the appropriate method of revealing the changes depends on the aim of the study, the region specifications, and the existing data, having considerable importance in the obtained results. The comparison technique after the classification is one of the most prevalent methods of revealing the changes, which in addition to the types of changes; it also determines the change in the area of each classification. The areas of different agricultural land and garden classes were calculated according to Table 1, showing that according to the max. likelihood classification, the area of agricultural lands, based on Landsat images from 1984 to 2015, reduced by 1038.482 hectare, while the reduction shown by Quickbird satellite was 1036.236 hectares. According to the max. likelihood classification, the area of gardens, based on Landsat images from 1984 to 2015, reduced by 27.3146 hectares, while, according to Quickbird, the reduction was 119.8833 hectares from 2003 to 2015.

The general results from the present study can be classified as follows:
- The remote sensing devices can be used as an important factor in generating the information in management of natural resources and agricultural lands.
- Existence of Landsat images related to the past years can be considered as a reliable source of data.
- Comparing the images and analyzing the expressed classification verifications, the Quickbird images were determined to be more appropriate than the ones from Landsat.
- The most important problem in using satellite pictures in analyzing the land use changes is the lack of land benchmarks from the past years.

- The obtained information from comparing the maps regarding the plant coverage should be evaluated according to the lateral information.
- Field operations are essential for optimum interpretation of the images, increasing the accuracy of the results.
- The results of such studies can be used in estimating the physiologic compaction of the population, determining the distribution, and extend the land uses as well as other environmental studies.
- The values and prominence of using the satellite images can be found, in case the time factor and the estimated cost for the cultivated area by this method are compared with the land surveying data, and if the errors due to the applied field studies that are mainly by human interventions are taken into consideration.

References

Ahmadi Nadoushan, M., Safiyanian, A., & Khajeheddin, S. J. (2014). Survey of land cover changes in Arak city using remote sensing and GIS. *Journal of Environmental Technology Science*, 93.

Alavi Panah, S. K. (2006). Remote Sensing in Earth Sciences. *Tehran University Press*, p. 437.

Arkhi, S. (2014). Predicting the trend of changes in the location of land uses by using LCM model in GIS domain. *Scientific – research two-seasonal magazine of supporting and preserving the jungles and pastures*, 1(12).

Bakhtiarifar, M., Saadi Mesgari, M., Karimi, M., & Chehrqani, A. (2011). Modeling the change of land use by multi-criteria decisions and GIS methods. *Environmentology publication*, 58(37).

Butt, A., Shabbir, R., Ahmad, S. S., & Aziz, N. (2015). Land use change mapping and analysis using Remote Sensing and GIS: A case study of Simly watershed, Islamabad, Pakistan. *The Egyptian Journal of Remote Sensing and Space Science*, 18(2), 251-259.

Cheruto, M. C., Kauti, M. K., Kisangau, P. D., & Kariuki, P. C. (2016). Assessment of land use and land cover change using GIS and remote sensing techniques: *a case study of Makueni County, Kenya*.

Darvishsefat, A. A. (1998). *Text book of remote sensing. Natural resources faculty, Tehran University*, p. 164.

Davoodi Monazam, Z., Hajinejad, A., Abbasnia, M., & Pourhashemi, S. (2014). Control of the land use changes by remote sensing. *Remote sensing and GIS in natural resources journal*, 1(5).

Givi Ashraf, Z., & Sarjargar, A. (2011). Controlling the land use by remote sensing for evaluating the desertification. *Geomatic National Conference*.

Hegazi, I. R., & Kaloop, M. R. (2015). Monitoring urban growth and land use change detection with GIS and remote sensing techniques in Daqahlia governorate Egypt. *International Journal of Sustainable Built Environment*, 4(1), 117-124.

Hosseini, M., Karimi, M., Saadi Mesgari, M., & Heydari, M. (2016). Designing and implementing an integrated modeling system for changing the land use of urban areas. *Geographical science publication*, 40(16).

Javanmardi, S., Faraji Sabokbar, H., Yavari, A. R., & Pourkhabaz, H. R. (2011). Evaluating the suitability of lands for agriculture by GIS. *Environment researches*, 4(2).

Khodakarami, L., Sefianian, A. (2012) "Application of multi-time remote sensing in determining the cultivated land" *Agriculture and natural resources science and technology and water and soil sciences journal,* 59 (16)

Mahdavi, E., Kiani, M., & Daneshvar Ameri, J. (2017). Evaluation of Barriers to Agricultural Land Integration. *Iranian Journal of Agricultural Economics and Research*, 48(2).

Mallupattu, P. K., Reddy, S., & Reddy, J. (2013). Analysis of land use/land cover changes using remote sensing data and GIS at an Urban Area, Tirupati, India. *The Scientific World Journal*.

Moradi, A. R., Jafari, M., Arzani, H., & Ebrahimi, M. (2016). Evaluation of pasture land use to dry farming by satellite pictures and GIS. *Remote sensing and GIS in natural resources journal*, 1(7).

Pakpour Rabti, A., Jafarzadeh, A. A., Shahbazi, F., & Ammari, P. (2013). Evaluation of susceptible lands for crops using GIS in some regions in West Azerbaijan, *Water and soil publication*, (23).

Pilehforoushha, P., KMarimi, M., & Taleie, M. (2014). Determining the suitable lands for crops by using GIS and fuzzy inferring systems. *Remote sensing and GIS publication*, (6).

Weng, Q. (2002). Land use change analysis in the Zhujiang Delta of China using satellite remotesensing, GIS and stochastic modeling. *Journal of Environmental Management*, 64, 273-284.

Zangiabadi, A., & Abolhassani, F. (2013). Applying GIS and RS in planning for the spatial control by emphasis on agriculture sub-section. *Geographical information (Sepehr) magazine*, 86(22).

Using Discrete Wavelet Transform to increase the Accuracy of Hyper Spectral and High Resolution Images Fusion

Hasan Hasani Moghaddam[a][*], Ali Asghar Torahi[b], Parviz Zeaiean Firooz Abadi[c]

[a]*MSc of remote sensing and GIS, Kharazmi University.*
[b] *Assistant professor of remote sensing and GIS, Faculty of geography, Kharazmi University.*
[c] *Associated professor of remote sensing and GIS, Faculty of Geography, Kharazmi University.*

Abstract

In optical remote sensing, hyper-spectral (HS) image which contains color information is produced by hundreds of spectral bands. Because of the trade-off imposed by the physical constraint between spatial and spectral resolutions, the HS image has poor spatial resolution. On the contrary, the panchromatic (PAN) images have high spatial resolution but no color information. Image fusion can combine the geometric detail of PAN image and the color information of the HS image to produce a high-resolution HS image. The aim of this study is the fusion of Hyperion and OrbView-3 PAN images based on Discrete Wavelet Transform (DWT). Firstly, the preprocessing methods were applied on Hyperion and OrbView-3 images and registration method based on nearest neighbor method were applied on two dataset. In order to fit images pixel size, the resampling operation was applied. PAN image was decomposed by DWT and then fused by hyper spectral image with GST algorithm. DIV, CC, Q and RMSE accuracy assessment methods were used on final fused image to evaluate the results accuracy. The results showed that using DWT based decomposition PAN image, preserve the spatial information during fusion rule. Also this technique gains high accuracy in term of spectral information of hyper spectral image.

Keywords: Discrete Wavelet Transform (DWT), Hyperion, OrbView-3, Accuracy assessment

---

[*] Corresponding author. Tel: +98-9148396587.
   E-mail address: www.h.moghaddam@gmail.com.

1. Introduction

In real world applications where various optical sensors are used for image acquisition, it is often difficult to obtain a good quality image by a single sensor (Omar and Stathaki, 2014). Image fusion is an efficient way of retrieving the information from multiple sources into one image (Dogra et al., 2018). Fusion of two images acquired from different sources has many applications (Hasani Moghaddam., 2018): medical (Nandeesh and Meenakshi, 2015; Galande and Patil, 2013), vegetation detection and monitoring (Gasparovic et al., 2018), urban studies (Lino et al., 2018), climate (Kar and Banerjee, 2018), etc. One of the important pre-processing steps for the fusion process is image registration. Image registration is the process of transforming different sets of data into one coordinate system (Rani and Sharma, 2013). Wavelet hypothesis is an expansion of Fourier hypothesis and it is acquainted as an option with the brief span Fourier change (Bopche and Gade, 2018). Wavelet transforms provide a framework in which a signal is decomposed, with each level corresponding to a coarser resolution or lower frequency band, and higher frequency bands (Maddali et al., 2012). In discrete wavelet transform (DWT), a two channel filter band is used. When decomposition is performed, the approximation and detail component can be separated and 2-D Discrete Wavelet Transformation (DWT) converts the image from the spatial domain to frequency domain (Rani and Sharma, 2013).

Li et al., (2018), to reduce the spectral distortions of fused images focusing on optimizing the approach used to extract spatial details from the PAN band, or on the optimization of the models employed during the injection of spatial details into the MS bands. The HR, GSA and SFIM algorithms applied on images; the results showed that the proposed method offers the lowest spectral distortions and more sharpened boundaries between different image objects than other methods, especially for boundaries between vegetation and non-vegetation objects.

Xia et al. (2018), to solve the low frequency sub band coefficients obtained by the NSCT decomposition which is not conducive to maintaining the details of the source image, proposed a medical image fusion algorithm that combined with sparse representation and pulse coupling neural network. In this method, the source image was initially decomposed into low and high frequency sub band coefficients by NSCT transform, Secondly, the K singular value decomposition (K-SVD) method is used to train the low frequency sub and coefficients. The experimental results and analysis showed that the algorithm of gray and color image fusion is about 34% and 10% higher than the contrast algorithm in the edge information transfer factor QAB/F index, and the performance of the fusion result is better than the existing algorithm.

He et al. (2018), to better preserve the interesting region and its corresponding detail information, proposed a novel multi scale fusion scheme based on interesting region detection. In this method first, the Mean Shift is used to detect the interesting region with the salient objects and the background region of IR and VI. Then the interesting regions are processed by the guided filter. The results demonstrated that the proposed algorithm can integrate more background details as well as highlight the interesting region with the salient objects, which is superior to the conventional methods in objective quality evaluations and visual inspection.

Borsoi et al. (2018), introduced a novel Hyper spectral- Multi spectral image fusion strategy that combined an un-mixing-based formulation with an explicit parametric model for typical spectral variability between the two images. Simulations with synthetic and real data show that the proposed strategy leads to a significant performance improvement under spectral variability and state-of-the-art performance otherwise.

Haribadu and Bindu (2017), proposed an image fusion method based on Discrete Wavelet Transform (DWT) and visibility. In the proposed method, one level DWT applied on Gray level MRI image and color information of intensity component of PET image to get four coefficients and finally the fused image obtained after applying inverse Discrete Wavelet Transform (IDWT). The results showed that the proposed work gives good result and also improve the resolution of the image for better visual perception with respect to PSNR, MSE, Cross correlation, Mean, Standard Deviation and Entropy values.

This paper leads to fusion of hyper spectral and high resolution images based on DWT transform. For this purpose, pre-processing operations were initially applied to the hyper spectral data, and then the two sets of data were registered. The GST algorithm were applied to fusion scheme and the DIV, CC, Q and RMSE indexes were used for accuracy assessment of final fusion. The innovation of this paper is using wavelet transform decomposition of PAN image to prominent spatial information of it and using this

information for accuracy improvement of hyperspectral and high resolution image fusion. It is supposed that high accuracy results can be gained using this method.

2. Materials and Methods

2.1 Satellite Imagery and Study area

EO-1/ Hyperion is the first hyper spectral satellite in the new millennium launched by NASA in Nov. 21, 2000. Hyperion data can now be acquired from the USGS EROS data center (Figure1). OrbView-3 is a high-resolution imaging mini-satellite owned and operated by orbital imaging corporation (ORBIMAGE), which is a commercial provider of earth imagery acquired from family of imaging satellites (Figure2). Table (1), shows the technical information of used data.

Table1. Tabulation of data for used images

Satellite-Sensors	Spatial Resolution (meter)	Spectral Range (nanometer)	Band Number
EO-1 - Hyperion	30	400-2500	242
OrbView-3 panchromatic	1	450-950	1
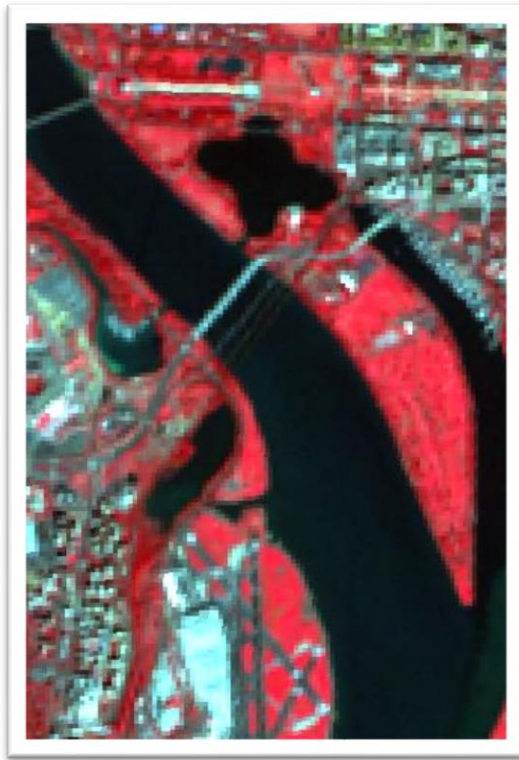
Figure1. Hyperion Image   **Figure2**. OrbView-3 Image

Because the data used for image fusion must be acquired from one scene in the same or the nearest time, such relevant data from Washington city of United States of America was found. This area is located at 38° 50ʹ N and 77° 00ʹ W to 38° 54ʹ and 77° 03ʹ geographic latitude and longitudes.

2.2 Data Preparation

Co-registration of two images has been done using the high-resolution image (OrbView-3 pan) as master and Hyperion as slave. The amount of RMSE in the registration processes was about 0.83 RMSE. The final pixel size of 4 meter was used to fit two dataset. This spatial resolution was chosen based on SF (ratio of high spectral resolution pixel size to high spatial resolution pixel size), method. After preparation of images, the DWT decomposition applied on PAN image and results fused with hyper spectral image by GST algorithm.

2.3 Discrete Wavelet Transform (DWT)

Wavelet transform is a mathematical tool developed originally in the field of signal processing. It can also be applied to fuse image data following the concept of the multi-resolution analysis (Jagruti, 2014). The scaled and translated basis elements of the 2D wavelet transform are given by (Adelson et al., 1987). Wavelet transforms provide a framework in which a signal is decomposed, with each level corresponding to a coarser resolution or lower frequency band and higher frequency bands. The Discrete Wavelet Transform (DWT), which applies a two channel filter band (with down sampling) iteratively to the low pass band (initially the original signal). The wavelet representation consists of the low-pass band at the lowest resolution and the high-pass bands obtained at each step. This transformation is invertible and non-redundant. In wavelet analysis, wavelet transform divides the image signal into wavelets representing each pixel of the original image as coefficients.
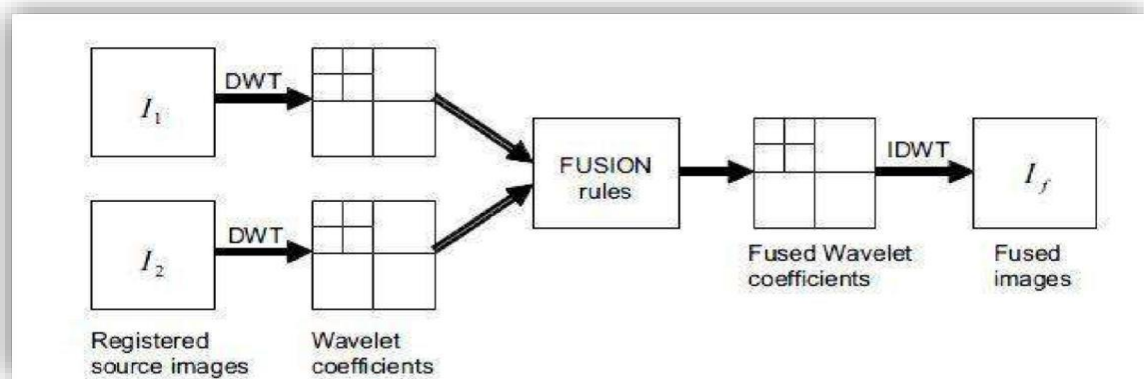
Figure3. Wavelet Transform based image fusion (Hasani Moghaddam, 2018)

The 2D image signals are broken down through layer by layer decomposition process. Four frequency bands, named (A) Low-Low, (B) Low-High, (C) High-Low and (D) High-High are obtained after first level of decomposition. The next level of decomposition is obtained by applying a recursive decomposition procedure applied to the Low-Low band of the current decomposition stage. Thus, N-level decomposition will finally result into 3N+1 different frequency bands including 3N high frequency bands and one Low-Low frequency band (Deepika and Sindhuja, 2014).
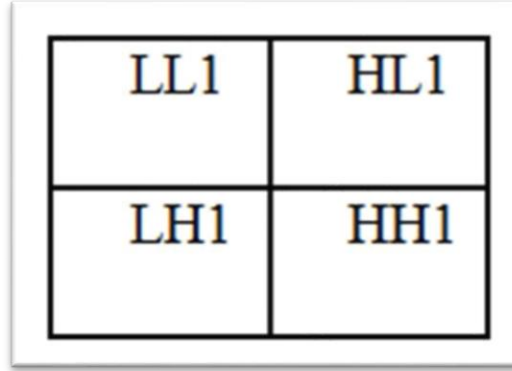
Figure4. Sub-band distribution of Discrete Wavelet Transform for level (Hasani Moghadda, 2018)

2.4 Gram-Schmit Transformation (GST)

The GS procedure makes a set of random variables uncorrelated or orthogonal to each other, assuming knowledge of the cross-correlations between them. For instance, with three random variables x_1, x_2 and x_3 with known correlations:

$$p_{ij} = E\left[x_i, x_j\right], ij \in [1,2,3]$$ (1)

This equation is obtained first.

$$\begin{bmatrix} V_2^1 \\ V_3^1 \end{bmatrix} = \begin{bmatrix} -q_2^1 & 1 & 0 \\ -q_3^1 & 0 & 1 \end{bmatrix} * \begin{bmatrix} x_1 \\ x_2 \\ x_3 \end{bmatrix}$$

(2)

where $q_j^1 = p_{j1}p_{11}, j = 2,3$

This operation produces random variables v_2^1 and v_3^1 which are orthogonal to x_1 but correlated with x_2 and x_3, respectively. The next step is to find a random variable which is correlated with x_3 x but orthogonal to both x_1 and x_2. This is accomplished by defining:

$$v_3^2 = v_3^1 - \frac{E\left[v_3^1 v_2^1\right]}{E\left[v_2^1\right]} * v_2^1$$

(3)

The expectations on the right-hand side can be computed by cross-correlations of the original variables. The variables x_1, v_2^1 and v_3^1 are orthogonal to each other, while spanning the probability space of x_1, x_2 and x_3 the task of orthogonal the input is complete. The procedure is easily extended to an arbitrary number of random variables (Darvishi et al., 2005).

2.5 Accuracy Assessment of Fusion Method

Image fusion methods are evaluated by comparing the fused image and reference image which is assumed to be ideal. Generally, the reference image is not available in practice. Hence these methods are evaluated by comparing the original low resolution HS image and fused image (Mamatha et al., 2015).

A. Root mean square

It is a frequently used parameter to compare the difference between original HS image and pan-sharpened image by directly calculating the changes in pixel values. It is defined as:

$$RMSE = \sqrt{\frac{1}{i*h*n}\left(\sum\sum\sum(F(i,j) - H(i,j))\right)^2} \tag{4}$$

$i*h*n$ represent the size of the fused image. H(i, j) is the pixel value of HS image and F (i, j) is the pixel value of fused image at i, j location .

B. Correlation Coefficient

It measures the similarity of two images. It ranges from -1 to +1. +1 indicates that two images are highly similar and -1 indicates highly dissimilar. It is calculated as:

$$CC(\text{F},H) = \frac{\sum(F - \overline{F})(H - \overline{H})}{\left(\sum(F - \overline{F})^2\right)(\sum(H - \overline{H})^2)} \tag{5}$$

F, H represent fused image and Hyper spectral image.

C, Universal Image Quality Index (Q)

It is calculated as:

$$Q = \frac{4\sigma_{fh}\overline{FH}}{\sigma_f^2\sigma_h^2\left(\overline{F^2} + \overline{H^2}\right)} \tag{6}$$

Where σ_{fh} is covariance between fused image and HS image. $\sigma_h^2 and \sigma_f^2$ are variance of HS and fused images respectively and $\overline{H}, \overline{F}$ are mean of HS and fused images respectively.

D. Differences in variances (DIV):-

It is calculated as:

$$DIV = 1 - \frac{var\,iance\left(Fused\,\text{Im}age\right)}{var\,iance\left(Original\,\text{Im}age\right)} \tag{7}$$

3. Results and Discussion

The result of image fusion based on DWT decomposition showed that implementation of DWT coefficient on PAN image have a high accuracy in terms of hyper spectral and high-resolution images fusion.

Spatial quality evaluation of the fused image is a complex task usually based on perceptual inspection. It can be clearly observed from the fused images as all the image fusion methods sharpen the respective hyper-spectral bands. Regarding the preservation of spatial resolution, all discussed image fusion methods behave similarly. However, a greater resemblance between the panchromatic and the intensity image doesn't mean better preservation of spatial resolution. Therefore, RMSE method is used for solving this issue. Due to the high correlation between the visible bands, the relation between one of the fused visible wavelength range images and the high resolution band must be calculated for accuracy assessment of image. Figure (5), showed final fused image of Hyperion and Orbview-3 pan images based on DWT.
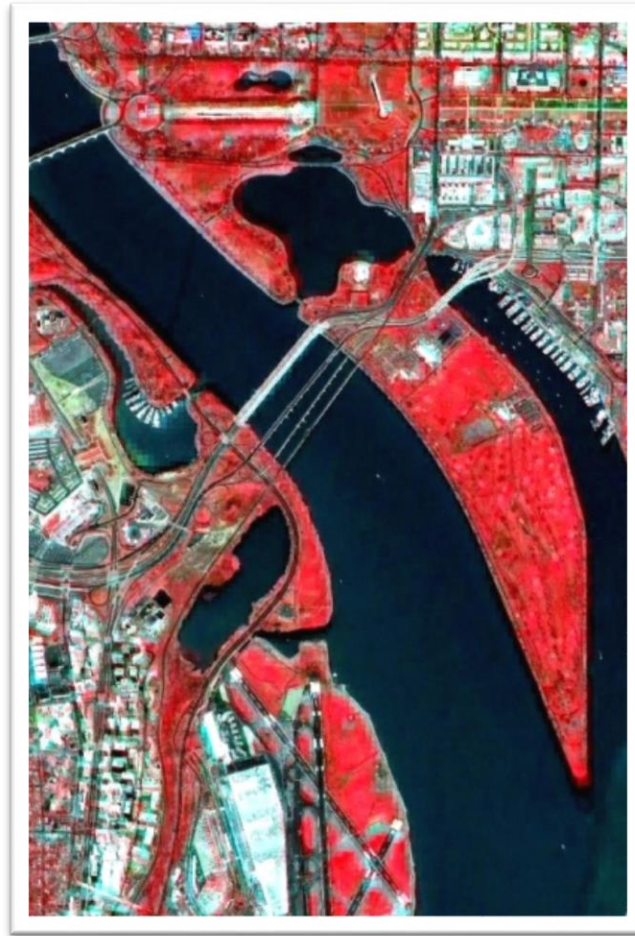
Figure5. Hyperion and Orbview-3 pan images fusion based on DWT

DIV, CC, Q and RMSE methods applied on fused image for accuracy assessment of it.

Table2. Accuracy assessment

	DIV	CC	Q	RMSE
Fused Image	0.0406	0.920	0.854	2.438

Based on the results, it can be clearly observed that the DWT based fusion technique has high accuracy. In all of the accuracy assessment methods, fusion images have high results and it showed the high quality of fused images in terms of spatial and spectral feature presentation.

4. Conclusions

The image fusion methods are used to generate high resolution images that attempts to preserve the spectral characteristics of the original data. There are no generalized criteria for the selection of a particular fusion technique. The selection of the fusion method for an application depends largely on the dataset. For image fusion methods, spatial enhancement and spectral preservation are all critical issues. In this paper, DWT based hyper spectral and high-resolution image fusion was used and its performance evaluated by several accuracy assessment methods was shown. Applying the DWT coefficient on PAN image, preserve its spatial detail as well as the original image. This method in terms of hyper spectral and high-resolution image fusion, preserve high frequency information beside of low frequency information. Spectral and spatial information may be changed during fusion role, but by the use of DWT based image decomposition, this feature is transformed to fused images and showed in results. The results of this study were approved by (Mamatha et al., 2015) and (Bopche and Gade, 2018).

References

Adelson, E. H., Simoncelli, E., & Hingorani, R. (1987). Orthogonal pyramid transforms for coding, *SPIE*, Vol (845), 50-58.

Borsoi, R. A., Imbiriba, T., & Bermudez, J. C. M. (2018). Super-resolution for hyperspectral multispectral image fusion accounting for seasonal spectral variability. *arXiv preprint arXiv:* 1808. 10072.

Bopche, S., & Gade, A. (2018). Implementation of image fusion using DWT and PCA, *IJFRCSCE*, (4), 507-510.

Darvishi, A., Kappas, M., & Erasmi, S. (2005). Hyper-Spectral/High-Resolution Data fusion: *Assessing the Quality of EO1-Hyperion/Spot-Pan & Quickbird-MS Fused Images in Spectral Domain*.

Deepika, L., & Sindhuja, N. M. (2014). Performance analysis of image fusion algorithms using HAAR wavelet, *IJCSMC*, (3), 487-494.

Dogra, A., Goyal, B., & Agrawal, S. (2018). Medical image fusion: A brief introduction, *Biomedical and pharmacologhy,* (3), 1209-1214.

Galande, A, & Patil, R. (2013). The art of medical image fusion: A survey. *In 2013 International Conference on Advances in Computing, Communications and Informatics (ICACCI)*, IEEE, 400-405.

Gasparovic, M., Medak, D., Pilas, I., Jurjevic, L., & Balenovic, I. (2018). Fusion of Sentinel-2 and Planet scope imagery for vegetation detection and monitoring. In *Volumes ISPRS TC I Mid-term Symposium Innovative Sensing-From Sensors to Methods and Applications*.

Haribadu, M., & Bindu, C. H. (2017). Visibility based multimodal image fusion with DWT. In *2017 IEEE International Conference on Power, Control, Signals and Instrumentation Engineering (ICPCSI),* IEEE, 1561-1566.

Hasani Moghaddam, H. (2018). Performance evaluation of wavelet transform with decision level algorithms in fusion of Hyperspectral and High spatial resolution images, *MA thesis of Kharazmi University, Tehran. Iran.*

He, K., Zhou, D., Zhang, X., & Nie, R. (2018). Infrared and visible image fusion combining interesting region detection and non-subsampled contourlet transform, *Journal of sensors*, pp. 18-33.

Jagruti, V. (2014). Implementation of discrete wavelet transform based image fusion, *IOSR-JECE*, (9), pp. 107-109.

Kar, C., & Banerjee, S. (2018). An image processing approach for intensity detection of tropical cyclone using feature vector analysis. *International journal of image and data fusion*, (9), pp. 338-348.

Li, H., Jing, L., Tang, Y., & Wang, L. (2018). An image fusion method based image segmentation for high resolution remotely sensed imagery. *Remote sensing*, (5), pp. 790.

Lino, Sh., Ito, R., Doi, K., Imaizumi, T., & Hikosaka, Sh. (2018). CNN-based generation of high-accuracy urban distribution maps utilising SAR satellite imagery for short-term change monitoring. *International journal of image and data fusion*, (9), pp. 302-318.

Maddali, R., Prasad, K. S., & Bindu, C. H. (2012). Discrete wavelet transform based medical image fusion using spatial frequency technique, *IJSAA*, (2), pp. 43-47.

Mamatha, G., Lakshmaiah, M. V., & Sumalatha, V. (2015). Evaluation of DWT based image fusion with three resampling methods, *IARJSET*, (2), pp. 10-14.

Nandeesh, M. D., & Meenakshi, M. (2015). Image fusion algorithms for medical image- A comparision, Bonfring. *International Journal of Advances in Image Processing*, (5), pp. 23-26.

Omar, Z., & Stathaki, T. (2014). Image fusion: An overview. *Fifth International Conference on Intelligent Systems, Modeling and Simulation*, TNO human factors research.

Rani, K., & Sharma, R. (2013). Study of image fusion using discrete wavelet and multi wavelet transform. *IJIRCCE*, (1), pp. 795-799.

Rani, K., & Sharma, R. (2013). Study of different image fusion. *Emerging technology and advanced engineering*, (3), pp. 288- 291.

Xia, J., Chen, Y., Chen, A., & Chen, Y. (2018). Medical image fusion based on sparse representation and PCNN in NSCT domain. *Computational and mathematical methods in medicine*, pp. 1-12.

Inventory of Single Oak Trees Using Object-Based Method on WorldView-2 Satellite Images and Earth

Yousef Taghi Mollaei [a*] , Abdolali Karamshahi [b] , Seyyed Yousef Erfanifard [c]

[a] *Ph.D. Student of forestry in Ilam University*
[b] *Associate Professor and Faculty Member of Forest Sciences Department in University of Ilam*
[c] *Associate Professor, Department of Natural Resources and Environment, College of Agriculture, Shiraz University, Shiraz, Iran*

Abstract

Remote sensing provides data types and useful resources for forest mapping. Today, one of the most commonly used application in forestry is the identification of single tree and tree species compassion using object-based analysis and classification of satellite or aerial images. Forest data, which is derived from remote sensing methods, mainly focuses on the mass i.e. parts of the forest that are largely homogeneous, in particular, interconnected) and plot-level data. Haft-Barm Lake is the case study which is located in Fars province, representing closed forest in which oak is the valuable species. High Resolution Satellite Imagery of WV-2 has been used in this study. In this study, A UAV equipped with a compact digital camera has been used calibrated and modified to record not only the visual but also the near infrared reflection (NIR) of possibly infested oaks. The present study evaluated the estimation of forest parameters by focusing on single tree extraction using Object-Based method of classification with a complex matrix evaluation and AUC method with the help of the 4th UAV phantom bird image in two distinct regions. The object-based classification has the highest and best accuracy in estimating single-tree parameters. Object-Based classification method is a useful method to identify Oak tree Zagros Mountains forest. This study confirms that using WV-2 data one can extract the parameters of single trees in the forest. An overall Kappa Index of Agreement (KIA) of 0.97 and 0.96 for each study site has been achieved. It is also concluded that while UAV has the potential to provide flexible and feasible solutions for forest mapping, some issues related to image quality still need to be addressed in order to improve the classification performance.

Keywords: Separation of single trees, Canopy, Remote sensing, Classification, Zagros forests, Haft-Barm of Shiraz.

---

* *Corresponding author. Tel: +98-9176515623.*
  E-mail address: taghimollaei@yahoo.com.

1. Introduction

Forest inventory was traditionally a useful and accurate way of monitoring forest coverage, but updating cycle is relatively expensive Extra, if it's not direct quoting (Franklin, 2001; Zoèhrer, 1980; Gillis and Leckie, 1993). Wide range of forest can change rapidly, forest inventory traditionally Did not respond adequately to the development of change (Wulder et al., 2008). The climate warming and recent severe droughts have resulted in vegetation mortality in various woody biomasses across the globe (Allen et al., 2010; Breshears et al., 2005; Carnicer et al., 2011; Phillips et al., 2009; van Mantgem et al., 2009).

The separation of single trees and the extraction of tree-related structural data from remote sensing data has been a prominent application in a variety of activities e.g. detailed information on the level of individual trees can be used to monitor forest regeneration (Gougeon and Leckie, 1999; Clark et al., 2004a and 2004b). The reduction of fieldwork is required for surveying (Gong et al., 1999) and damage assessment to be used in the forest (Leckie et al., 1992; Levesque and King, 1999; Kelly et al., 2004).

Forest data, which is derived from remote sensing methods, mainly focuses on the mass (such as parts of the forest that are largely homogeneous, in particular, interconnected) and plot-level data. However, forest level variables are mainly average or aggregate of the combination of trees in the mass. In calculating forest variables such as volume and biomass of the growing population, model at single-tree level are mainly used today (Laasasenaho, 1982; Repola, 2009). Remote sensing data allows us to move from the surface of the mass to the level of single trees, which has a clear interest in precise forestry, forest management planning, biomass assessment and forest modeling (Koch et al., 2006).

The reasons for single-tree extraction from high-resolution satellite imagery are the importance of single trees and their maintenance such as the difficulty in single tree mapping in vulnerable areas, the need for quick access to quantitative characteristics estimation and the importance of remote sensing in statistics for single trees (spatial resolution and satellite data capability has been increasingly enhanced).

So far, no research has been done to estimate the single-tree feature on WV-2 images. In previous studies, the accuracy of estimating the crown area is made using field data, in which the crown shape of the trees is generally considered circular and the crown area is obtained from the mean diameter, provided that the trees, according to the possible vegetative conditions, has crowns with non-hinged shapes. Therefore, it is necessary to assess the accuracy of crown areas in satellite data using more reliable data such as UAV aerial imagery.

Today, remote sensing data provides accurate and reliable information of single-tree biophysical properties in forest lands. In addition, the object-based classification has a particular advantage over other classification methods for extracting crowns and identifying species in a variety of ecosystems. Few study has been done to examine the efficiency of the object-based, which is highly desirable for users.

Remote sensing is a useful tool for forest mapping as it provides data and resources. Today, one of the most commonly used applications in forestry is the identification of single trees and tree species comparison using object-based analysis and classification of satellite or aerial images. Sedliak et al. (2017) identified groups of trees (leaf-leaf needles) in individual structures of massive mixed grass, spruce, and pine forests in WV-2 images. The object-based classification with WV-2 multispectral images was done in eCognition software. The Lidar data has been used for the identification of single tree with overall high accuracy of 87.42 percent. The accuracy of needle calves had risen from 82.93 to 85.73 percent and broadband ranged from 84.79 to 90.16 percent.

Basic object classification method is a useful method to identify the wild plants in numerous habitats. Niphadkar et al. (2017) used WV-2 images to identify shrubs in the tropical forests. The object-based method separates the features with the help of spatial characteristics. As a result, there has been the possibility to isolate the shrub in a complex tropical forests environment, with a non-parametric classification algorithm.

The accuracy of the tree species map allows more detailed analyzes of forest biophysical variables. Raczko and Zagajewski (2017) compared the support vector algorithms, random forest and neural network for the tree species class on aerospace aerial imagery. The results showed that the ANN classification had the highest classification accuracy of (77%), and SVM with 68% and RF with 62% respectively.

Juniati and Arrofiqoh (2017) compared the base pixel and base object classification using parametric and nonparametric methods for pattern matching in Indonesian forests with WV-2 images. They concluded that classifying the base object the best results in segmentation and classification and has the best kappa coefficient, after which the neural network and the Maximum Likelihood Classifier were ranked in the mean of accuracy.

Wen et al. (2017) concluded that the method of classification of piece-based and object based on other methods in extracting urban trees in WV-2 images is superior. They used three levels of classification (pixel, object and piece) to classify trees. The results showed 85% overall accuracy for all methods. In addition, user and producer accuracy reaches over 80% for the tree floor. The method of classification of the base unit was placed in the first priority, then the classification of the object based and in the third stage of the base pixel for the Kappa coefficient.

Okojie (2017) paid for extraction of single tree crowns and evaluated forest structure parameters using airborne UAV images. Accuracy assessment was performed using the root mean square error method. As a result, the crown of the trees and the height of the trees were extracted. The results of the baseline image analysis showed that the segmentation accuracy is significantly related to the spatial resolution of the images, but the internal parameters of the segmentation algorithm should also be appropriate and calibrated.

Thanh and Kappas (2018) compared the random forest tree classifier, the nearest neighbor and vector of support for land use classification using Sentinel-2 multispectral images around the Red River Delta of Vietnam. The accuracy of all classifications was between 90% and 95%. Among these classifications, using different training samples ranging from 50 to 1250 pixels, SVM created a higher overall accuracy. After that, the random forests were ranged with the nearest neighbor.

Estimating forest structural parameters is expensive and time-consuming with ground-based data collection methods. Remote sensing data is a low cost option in modelling and mapping structural parameters in large forest areas.

4. Materials and Methods

4.1. Study Area

The Haft-Barm Lake is located in the geographical location of N294921 E520227 in Fars province. These lakes are located 55 kilometers to the west of Shiraz and northeast of the protected areas of Arjan and Parishan and 2150 meters above sea level. The lakes have beautiful panoramic views of the hillocks and wetlands. The weather in the region is cold and dry in the winter and temperate in the summer. The area has an almost cold and semi-desert climate and its catchment area is 16.9 km^2 and the average annual precipitation is 1010 mm. The various plant species forms the forest and pasture and the vegetation cover. Oak trees are the major forest species in the region that are densely covered by the area. Regarding the range of Arjan between the tropical region of southern Iran and the dry region of the south-east, the cold and semi-humid part of the northwest is an intermediate or ecotone region and very diverse in terms of plant species diversity. This study was conducted on two different sites in the Haft-Barm area of Shiraz. The area of the first site (Baleh Zar village) is 106 hectares, and the second site of the Abe Anar village is 150 hectares (Figure 1).
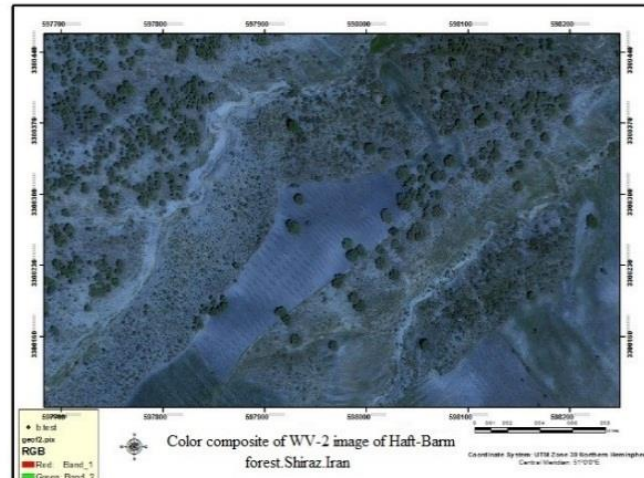
Figure 1. Study area location

4.2. Data

The data used in this study included the image of the WorldView-2 satellite on May 21, 2015 with a resolution of 1.8 m, and panchromatic bands (spatial resolution of 0.5 m) and UAV aerial imagery with a resolution of 3 cm. Topographic maps of the survey organization with a scale of 1:25,000 and points taken by three-frequency GPS. Also, the SPSS25; Excel version 2016; eCognation v. 8.7; ENVI, 5; Erdas Imagine and Google Earth were used. The flowchart is shown in Figure 2.
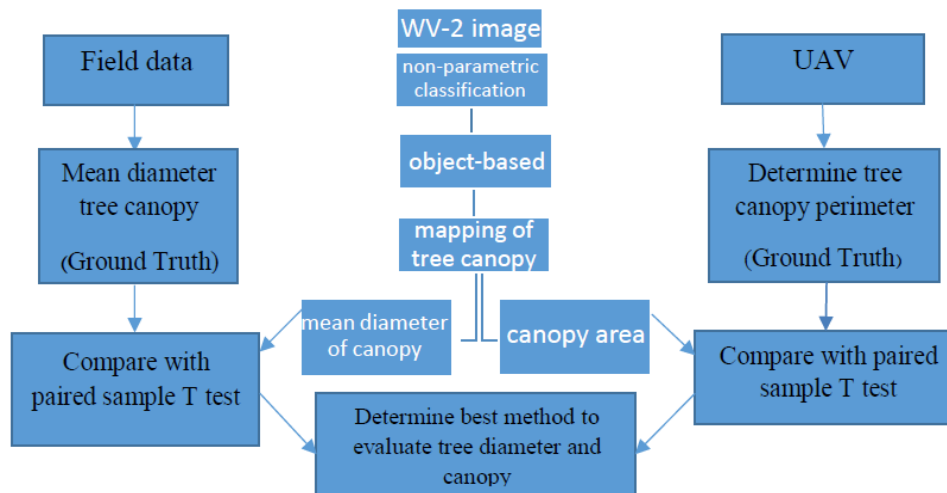
Figure 2. Flowchart of work levels

The Worldview-2 images were georeferenced using the 9-point of three-frequency GPS tracking RTK and static ground reference and the UTM image system was considered. The cloud computing points were taken from ArcGIS10.4 and PCI Geomatica16 software. with an accuracy, the average mean square root (RMSE) of 0.65 pixels was georeferenced using the equation of degree three (ST order polynomia3). Then,

Pan sharpening images with a resolution of 0.5 m were created with a combination of polygonal and panchromatic quadrants (Table 1).

Table 1. Characteristics of sensor and four standard bands of WV-2

Wavelength nm	Bands of WorldView-2 sensor
450-800	panchromatic
450-510	blue
510-580	green
630-690	red
770-895	NIR1

In order to inventory the trees perimeter in the forest area, we took pictures of drone images from Phantom 4 Pro. The Phantom 4 Peru is equipped with a one-inch CMOS camera that can capture 20-megapixel quality (Dji, 2016) (Figure 3).

Figure 3. The commercial "ready-to-use" Micro-drones MD 4-200. Payload includes IMU, GPS receiver, downward pointing CIR-modified digital Canon IXUS 100 camera, radio downlink and microprocessor controlled flight control units

4.3. The Nearest neighbor classifier

Classifier of the nearest neighbor (Schowengerdt, 1997): Lists of nonparametric classifications of unknown pixels in accordance to the labels of the neighboring educational vectors in the image space include:

The best neighbor: Labels the nearest pixels surrounding the training pixel.

Nearest k: Assemblies are based on the majority of the training pixel tags near the neighbor k.

The nearest neighbor k is the weighted distance: assigns weights to the closest neighbor k, based on the label of the closest neighboring k instructional pixels, in the opposite proportion to the Euclidean distance of the unknown pixel, and assigns the label to the highest weight of the set.

4.4. Object Based Classification

Pixel Based analysis is usually simple and operates in a comprehensive and general way on the sensors. Although pixels are often not a favorite unit, Measuring is not possible without them. For example, the canopy of separate trees and gap between crowns involves several pixels and creates a spatial self-regulation within objects that we can easily detach in high-resolution images (Woodcock and Strahler, 1987). OBIA

seems to search for a "mean" for objects. It searches for objects by segmenting the image into groups of pixels with similar characteristics based on spatial and spatial properties (Benz et al., 2004).

The purpose of the image segmentation is to extract the image objects in the best case according to the scale features, the weight of the inhomogeneity of softness and the compression weight that was performed in the software. These parameters were obtained with ESP and with test and error. Later, the obtained objects enter the classification methods. Multi-resolution segmentation was done by segmentation process. Using the approach of the nearest neighbor and identifying suitable training samples, the image was classified into two general forest and non-forest classes (Table 2).

Table 2. Weighting for segmentation

Hierarchy	Scale parameter	Color factor	Shape factor	Compactness degree	Softness degree
Level1	10	0.8	0.2	0.7	0.3
Level2	20	0.8	0.2	0.7	0.3

The most basic of the multi-resolution segmentation algorithms is the scale parameter. For the first time Dragut et al. (2010) based on local variations in the multi-scale segmentation algorithm at the time of segmentation and pixel integration used the ESP (Estimation of Scale Parameter), which is the extension of eCognition, and the most appropriate scale for determining the segmentation. If two pixels or the same object are merged, the rate of local variation will decrease, but if two pixels or non-sex objects are merged, the process of local variation changes will increase.

The graph represents the points where the ROC-LV has increased when the pieces were merged and new larger parts were created, which is an appropriate scale for image segmentation. The best scales for our image were 24, 26, 30, 34, 37, 31, 41, 45, 47, 49, 51, 54, 57, 60, 71, 75, 79, 88, and 94 (Figure 4).
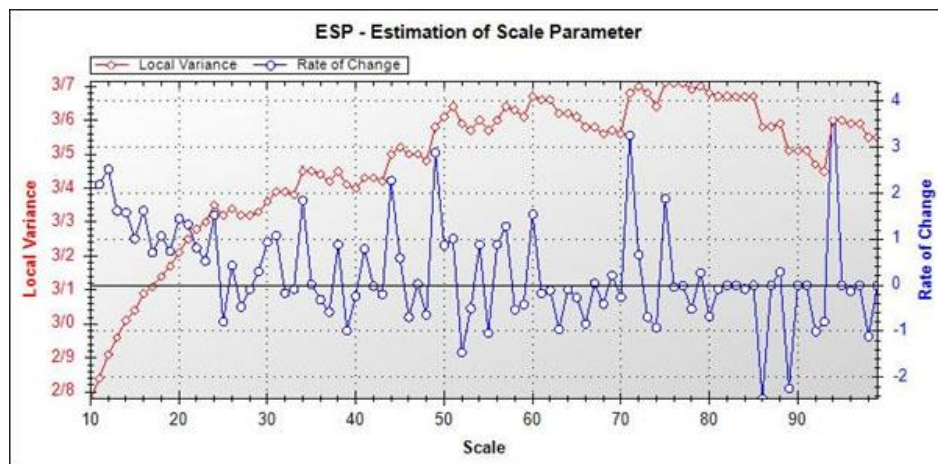
Figure 4. ROC-LV schematic

After selecting the training data, they were arranged in a thematic layer, the TTA mask layer, in the software to be used during the process. The same training data was used for different classification methods and Classification was performed in three ways.

After extracting the forest feature in the three methods, the results were assessed. For this, 100 points were created randomly on the images, and the canopy boundary of these trees was determined from UAV images (Figure 5).

Figure 5. Canopy of 100 determined trees on UAV image for Ground truth

4.5. Accuracy assessment

Accuracy assessment was done in two ways: the usual method, which used Kappa coefficient, and the second method was performed using the AUC method.

4.6. Sampling method for quantitative and qualitative forest characteristics

The study sampling method has been carried out in a systematic approach. A 200 * 200-meter rectangular grid was overlaid in the image of the region, with 40x40 m rectangular sample pieces discharged into the area. A total of 63 sample plots (36 plots of AbeAnar village and 27 villages of BalehZar village) were measured at each site. In each plot, the considered characteristics of the vegetation included: Recording the diameter of large and small trees, the diameter at breast height (DBH), the tree crown cover, and the health of the tree.

The estimated canopy cover area for BalehZar forest trees on WV-2 and UAV images, the sampling with 200×200 square meter network on the ground and satellite images of WV-2 was carried out. In the village of BalehZar 27 plots of 1600 square meters (40×40 m) were collected on site 1, and site 2 the village of AbeAnar with 33 plots. In each sample piece, the large and small diameters, the diameter of the breasts and then the crown cover area (equation 1) were measured. The quantitative statistics in the forests of the BalehZar village including the number of samples, mean, standard deviation and standard error in two methods of land cover and WV-2 depiction were presented in Table 1. The results of this study showed that, the sample area was calculated on the basis of equation 1. Then analysis of the canopy cover areas was carried out to the SPSS25 environment (Table 1).

Covering the crown surface = π / 4 ×Medium crown diameter   (1)

5. Results and discussion

In Figure 6, the results were derived from three types of vector support vector, decision tree, and object-based. As you can see, the quality of the classifications is almost the same. But there are differences in accuracy. The accuracy assessment was done in two ways: the usual method of Kappa coefficient and AUC

method. In the accuracy assessment tables, error matrix, overall accuracy, kappa coefficients, manufacturer accuracy, and user precision of each method is presented.
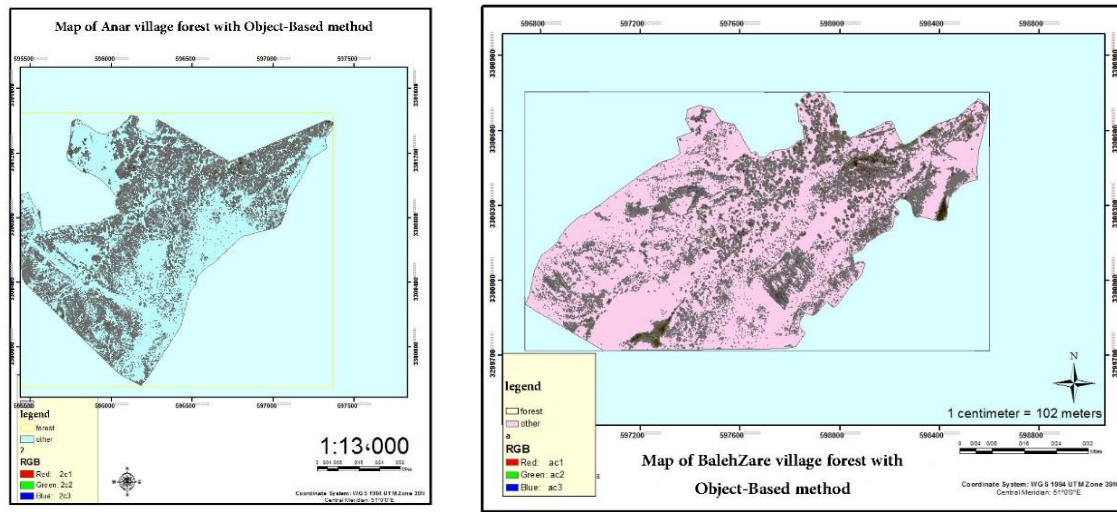

Figure 6. Classification results of the forest feature with object-based algorithm in BalehZare (right image) and Abe Anar sites (left)

5.1. Accuracy assessment of WV-2 canopy cover area with UAV cover

5.1.1. Regression of canopy cover area in BalehZar forests

Data analysis

At first, the normal distribution of data was investigated by Kolmogrov-Smirnov test. The result of the test showed that all data had normal distribution and were significant at 99%level.

To compare the canopy coverage obtained from WV-2 satellite imagery and groundbreaking, T-pair test was used at 95% confidence level. The results of the Paired Sample t test between measured forest and image data showed that there was no significant difference between the measurement of canopy coverage in two methods at a significant level of 95% (df = 99, t = 1.984). Figure 8 shows the correctness of the item.

The regression analysis results showed that satellite imagery with an approximate magnitude of 0.95 (R^2 =95%) illustrates the potential for high-resolution WV-2 satellite images (Table 3 and 4 of the statistical model).

In Table 4 of the statistical model, the area of canopy on the ground as an associated variable and canopy area on satellite images is considered as an independent variable. The results of analysis of variance and coefficient test showed that WV-2 satellite images can be used to estimate the canopy surface. The point cloud is plotted in Figure 7. In which the X axis is the crown surface on the satellite image and the Y axis is the crown surface on the ground.

As a result, the WV-2 images can be used instead of land surveying to calculate the area of the canopy of forests, which is consistent with the results of the researchers.

Table 3a. Statistical data of the canopy cover of trees in the forests of BalehZar

Variable of canopy cover percent in forest inventory of BalehZar	Inventory method with UAV	Object-based WV-2 satellite images
Samples number	100	100
Mean (m^2)	68.48	66.70
Standard deviation (m^2)	41.63	40.84
Standard error (m^2)	4.16	4.08

Table 3b. Statistical data of the canopy cover of trees in the forests of AbeAnar

Variable of canopy cover percent in forest inventory of BalehZar	Inventory method with UAV	Object-based WV-2 satellite images
Samples number	100	100
Mean (m^2)	44.62	44.89
Standard deviation (m^2)	28.9	28.68
Standard error (m^2)	2.89	2.87

Table 4. Statistical model of the canopy surface covering the satellite imagery of WV-2 and UAV of forests of the village of Balehazar and AbeAnar

Name	Model	Coefficient R^2	Coefficient r	Model of statistic
Object-based of Balehazar	Linear	0.953	0.976	Y = 2.11 + 0.995X
Object-based of AbeAnar	Linear	0.998	0.999	Y = -0.579 + 1.007X
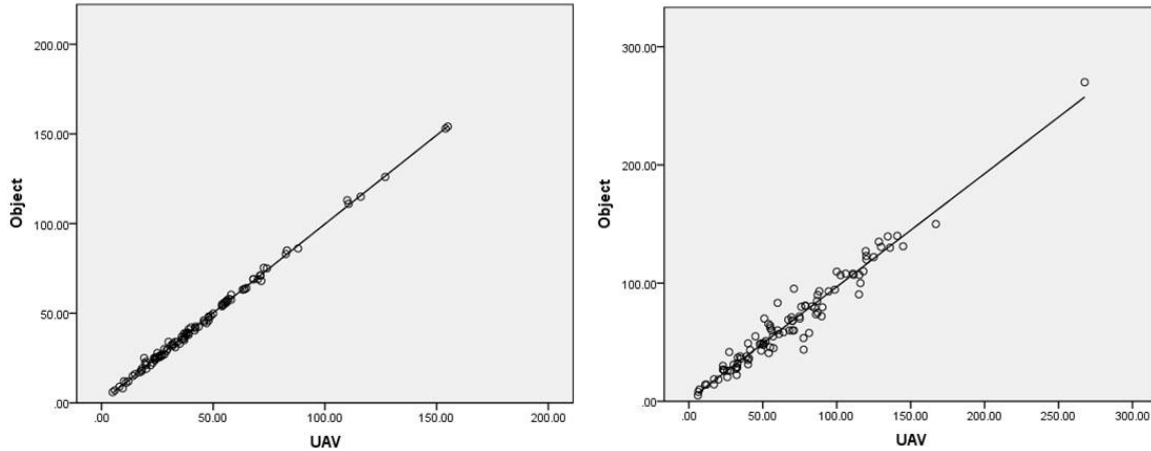
Figure 7. Evaluation of the accuracy of the canopy in Object-Based classification in satellite imagery WV-2 and UAV image in the forests of the village of Balehazar and AbeAnar

5.2. Evaluation of the accuracy of the diameter of the canopy in satellite imagery WV-2 with the ground in the forests of the village of Balehazar and AbeAnar.

For accuracy evaluation of the diameter of the canopy in satellite imagery WV-2 with ground points in the forests of the village of Balehzar and AbeAnar, initially, the normal distribution of data was investigated by Kolmogrov-Smirnov test. The result of the test showed that all data were normal distribution and are significant at 99% level.

To compare the average diameter of the canopy obtained from WV-2 satellite imagery and ground-level random sampling, t-test was used at 95% confidence level. The results of Paired Sample t test between measured forest and image data showed that there was no significant difference between the measurement of canopy coverage in two methods at a significant level of 95% (df = 99, t = 1.984). Figure 8 shows the correctness of the item.

The regression analysis results showed that satellite images with an approximate coefficient of 0.95 (R^2 =95%) indicate that the average diameter of the trees canopy can be obtained with high accuracy from WV-2 satellite images of (Table 5 and 6 of the statistical model).

Table 5a. Statistical data of Medium diameter of canopy of trees in BalehZar forest

	Mean(m)	Samples number	Standard deviation (m)	Standard error (m)
Medium diameter of canopy on ground	9.1279	100	2.959	0.295
Medium diameter of canopy in object-based	8.9876	100	2.733	0.273

Table 5b. Statistical data of Medium diameter of canopy of trees in AbeAnar forest

	Mean (m)	Samples number	Standard deviation (m)	Standard error (m)
Medium diameter of canopy on ground	7.3707	100	2.324	0.232
Medium diameter of canopy in object-based	7.2800	100	2.281	0.228

Table 6. Statistical model of the medium diameter of canopy surface covering in the satellite imagery of WV-2 and ground of forests of the village of Balehazar and AbeAnar

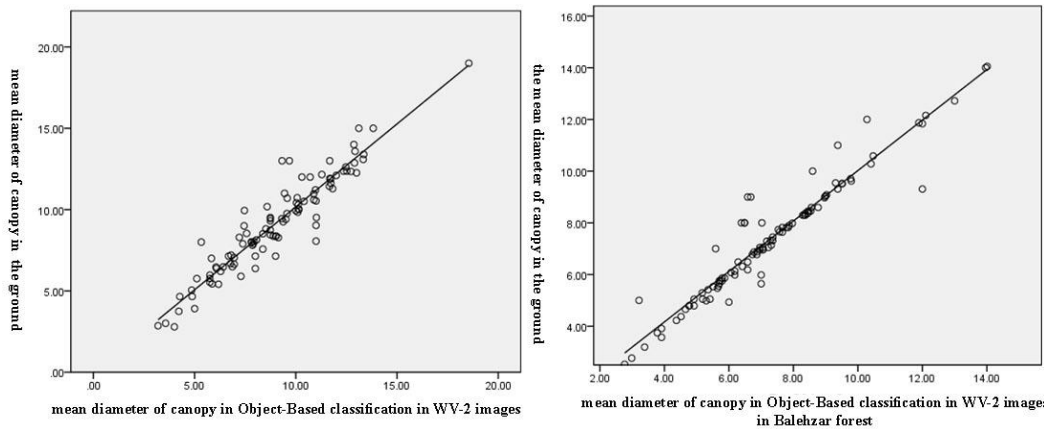| Name	Model	Coefficient R^2	Coefficient r	Model of statistic
Object-based of Balehazar	Linear	0.942	0.888	Y = -0.028 + 1.020X
Object-based of AbeAnar	Linear	0.958	0.918	Y = 0.256 + 0.976X

Figure 8. Assessing the accuracy of the mean diameter of canopy in Object-Based classification in WV-2 images and the ground of the trees in the forests of the village of Balehazar and AbeAnar

5.3. Assessing the accuracy of the crown cover in WV-2 images with the height of the trees in the forests of the village of Balehazar and AbeAnar

At first, the normal distribution of data was investigated by Kolmogrov-Smirnov test. The result of the test showed that all data had normal distribution and are significant at 99% level.

The regression analysis results showed that satellite images with a good explanation coefficient of 0.68 ($R^2 = 68\%$) indicated that height can be obtained with proper accuracy from satellite images of WV-2 (Table 7 of the statistical model and Figure 9).

Table 7. Statistical model of canopy surface in WV-2 images and tree height in the forests of the village of Balehzar and AbeAnar

Name	Model	Coefficient R^2	Coefficient r	Model of statistic
Object-based of Balehazar	Linear	0.696	0.828	Y = 5.117 + 0.056X
Object-based of AbeAnar	Linear	0.686	0.826	Y = 4.112 + 0.069X
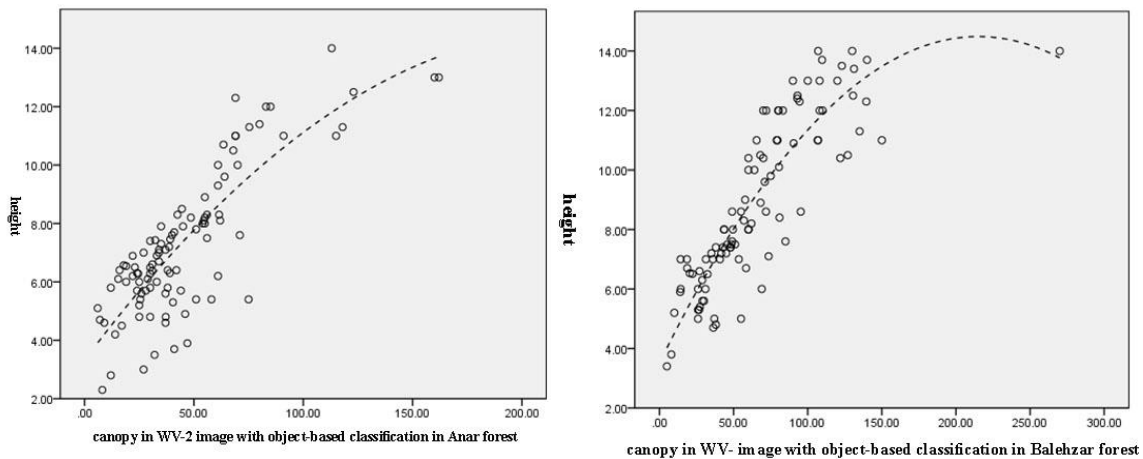
Figure 9. Assessing the accuracy of the crown cover in Object-Based classification in WV-2 images and the height of the trees in the forests of the village of Balehazar and AbeAnar

This study is one of the first studies to estimate and extract single-tree parameters from high-resolution satellite imagery. A high level of accuracy was obtained in estimating canopy cover, canopy diameter and height of trees with satellite imagery. In the object-based method, the training samples were taken as TTA mask (Training & Test Area MASK) in order to evaluate the accuracy of the classification using spectral data, and the Kappa coefficient was 0.974 (0.967 in the AbeAnar village and 0.981 in the village of BalehZar), with an overall accuracy of 98.82% (99.14% in the AbeAnar village and 98.51% in the village of BalehZar) was obtained in the classification error matrix. Therefore, the base object method, the support vector method, and decision tree method were respectively the highest classification accuracy in the study area (Table 8).

Table 8. Comparison of Object-Based classification in sites with matrix

Object-Based	Classification / accuracy
0.974	Kappa coefficient
98.82	Overall accuracy (%)

6. Conclusions

The study found that WV-2 data can be used to predict the tree parameters such as crown cover, bream diameter, tree height, tree number and biomass in the Zagros forests of Iran. The height of the trees can be obtained directly from the digital surface model using drone images. The crown cover and canopy diameter have a very high correlation with the terrestrial data. The combination of drone data with the satellite data from WV-2 has been useful to describe the biodiversity and monitoring the forest biodiversity. OBIA is widely used for forest remote-sensing research (Chubey et al., 2006; Desclee et al., 2006; Hay et al., 2005 and Wulder et al., 2008). It has been successful in forest tree studies (Conchedda et al., 2007; Myint et al., 2008 and Wang et al., 2004a). The object-based method in the extraction of single forest trees using spectral data is more potent than pixel-based methods.

According to the obtained results using WV-2 satellite spectral data in estimating the canopy surface, it was determined that these data are capable of estimating the quantitative characteristics of the crown cover of oak forests and extraction of single trees in the study area with proper accuracy.

There is a good correlation between the diameters of the crown of trees with ground measurements which indicates that extracting of the data using drone is excellent. The R coefficient result for the crown diameter of the forest trees was 0.85 in average, which is consistent with the results of Shrestha and Wynne (2012). They also obtained a correlation coefficient of 0.9 for the crown diameter.

As Pande-Chhetri et al. (2017) found in the estimation of wetland vegetation with WV-2 images, the object-based method was superior to the pixel-based method. In the current research, the object-based classification is better than other classifications, as the study results indicates that the SVM classification has a superior performance over the tree. The results obtained is compatible with Thanh Noi (2018), Raczko et al. (2017), Pande-Chhetri et al. (2017), Qian et al. (2015), Shafri and Ramle (2009), Shao et al. (2012), Kim et al. (2012), Amami et al. (2015), Ghasemian and Akhondzadeh (2016).
The very high correlation between the estimation of the canopy of the satellite images and terrestrial shows that one can estimate The canopy parameter from the images. The comparison between the estimated crown cover with the crown covering the ground surface in all the three methods shows that there is no significant difference between ground data and satellite image estimation at 5% significance level. This indicates that the nonparametric models used in the study have no significant difference with ground reality.

Considering other researchers' research on the extraction of features using algorithms, it is shown that the present study is of desirable accuracy.

Forecast models of this study, although they are surveyed for trees in Zagros forests, can be used for other forest levels with similar climate and species composition. This kind of forecast with drone images will help to properly assess the quality of carbon stored trees on the level of single trees. Further studies should be developed to predict biophysical parameters such as leaf area index, stem volume, etc. Management tables for forest planners such as forestry activities, disaster vulnerability, and age class are useful for forest trees. The functionality of these models can improve inappropriate data from other forest levels and if the area is not accessible, these equations can estimate trees from forest levels instead of being present in the field.

References

Amami, R., Ayed, D. B., & Ellouze, N. (2015). An Empirical comparison of SVM and some supervised learning algorithms for vowel recognition. *International Journal of Intelligent Information Processing (IJIIP)*, 3(1).

Allen, C. D., Macalady, A. K., Chenchouni, H., Bachelet, D., McDowell, N., Vennetier, M., & Gonzalez, P. (2010). A global overview of drought and heat-induced tree mortality reveals emerging climate change risks for forests. *Forest Ecology and Management*, 259(4), 660–684.

Benz, U. C., Hofmann, P., Willhauck, G., Lingenfelder, I., & Heynen, M. (2004). Multi-resolution, object-oriented fuzzy analysis of remote sensing data for GIS-ready information. *ISPRS Journal of Photogrammetry and Remote Sensing*, 58(4), 239-258.

Breshears, D. D., Cobb, N. S., Rich, P. M., Price, K. P., Allen, C. D., Balice, R. G., & Andrson, J. J. (2005). Regional vegetation die-off in response to global-change-type drought. *Proceedings of the National Academy of Sciences*, 102(42), 15144–15148.

Carnicer, J., Coll, M., Ninyerola, M., Pons, X., Sánchez, G., & Peñuelas, J. (2011). Widespread crown condition decline, food web disruption, and amplified tree mortality with increased climate change-type drought. *Proceedings of the National Academy of Sciences of the United States of America*, 108, 1474–1478.

Chubey, M. S., Franklin, S. E., & Wulder, M. A. (2006). Object-based analysis of Ikonos-2 imagery for extraction of forest inventory parameters. *Photogrammetric Engineering and Remote Sensing*, 72(4), 383-394.

Clark, D.B., Castro, C.S., Alvarado, L.D.A., & Read, J.M. (2004a). Quantifying mortality of tropical rain forest trees using high spatial- resolution satellite data, *Ecological Letters*, 7:52–59.

Clark, D.B., Read, J.M., Clark, M.L., Cruz, A.M., Dotti, M.F., & Clark, D.A. (2004b). Application of 1-m and 4-m resolution satellite data to ecological studies of tropical rain forests, *Ecological Applications*, 14:61–74.

Conchedda, G., Durieux, L., & Mayaux, P. (2007). Object-based monitoring of land cover changes in mangrove ecosystems of Senegal. *In 4th International Workshop on the Analysis of Multi-Temporal Remote Sensing Images*, Louvain, Belgium, IEEE. 44-49.

Desclee, B., Bogaert, P., & Defourny, P. (2006). Forest change detection by statistical object-based method. *Remote Sensing of Environment*, 102(1-2), 1-11.

Dji. (2016). PHANTOM 4 User Manual. Chine.

Drăguţ , Dirk Tiede & Shaun R. Levick. (2010). ESP: a tool to estimate scale parameter for multiresolution image segmentation of remotely sensed data. *International Journal of Geographical Information Science.*

Franklin, S. E. (2001). Remote sensing for sustainable forest management. *CRC press*. Lewis Publishers, New York, 296–300.

Ghasemian, N., & Akhondzadeh, M. (2016). Comparison of Methods of Artificial Neural Networks, Support Vector Machine and Decision Tree to Identify Clouds in Landsat 8 Satellite Images. *GEJ*. 2016, 7(4), 25-36. (In Persian).

Gillis, M. D., & Leckie, D. G. (1993). Forest inventory mapping procedures across Canada (Vol. 114).

Gougeon, F. A., & Leckie, D. G. (1999). Forest regeneration: Individual tree crown detection techniques for density and stocking assessment. In Proceedings of the International Forum on Automated Interpretation of High Spatial Resolution Digital Imagery for Forestry. *Canadian Forest Service, Pacific Forestry Center Victoria, BC*, 10-12.

Gong, P., Biging, G. S., Lee, S. M., Mei, X., Sheng, Y., Pu, R., Xu, B., Schwarz, K., & Mostafa, M. (1999). Photo ecometrics for forest inventory. *Geographic Information Science*, 5(1), 9–14.

Hay, G. J., Castilla, G., Wulder, M. A., & Ruiz, J. R. (2005). An automated object-based approach for the multiscale image segmentation of forest scenes. *International Journal of Applied Earth Observation and Geoinformation*, 7(4), 339-359.

Juniati, E., & Arrofiqoh, E. N. (2017). Comparison of Pixel-Based and Object-Based classification using parameters and non-parameters approach for the pattern consistency of multiscale land cover. The International Archives of the Photogrammetry, *Remote Sensing and Spatial Information Sciences*, Volume XLII-2/W7, 2017.

Kim, J., Kim, B. S., & Savarese, S. (2012). Comparing image classification methods: K-nearest-neighbor and support-vector-machines. *Applied Mathematics in Electrical and Computer Engineering. Harvard, Cambridge. USA*.

Kelly, M., Shaari, D., Guo, Q. H., & Liu, D. (2004). A comparison of standard and hybrid classifier methods for mapping hardwood mortality in areas affected by "sudden oak death," *Photogrammetric Engineering & Remote Sensing*, 70(11), 1229–1239.

Koch, B., Heyder, U., & Weinacker, H. (2006). Detection of individual tree crowns in airborne lidar data. *Photogrammetric Engineering & Remote Sensing*, 72(4), 357–363.

Laasasenaho, J. (1982). Taper Curve and Volume Functions for Pine, *Spruce and Birch. Commun. Inst. Forest Fenn*. 108, 1–74.

Leckie, D. G., Yuan, X., Ostaff, D. P., Piene, H., & Maclean, D. A. (1992). Analysis of high spatial resolution multispectral MEIS imagery for spruce budworm damage assessment on a single tree basis. *Remote Sensing of Environment*, 40(2), 125–136.

Levesque, J., & King, D. J. (1999). Airborne digital camera image semivariance for evaluation of forest structural damage at an acid mine site. *Remote Sensing of Environment*, 68(2), 112–124.

Myint, S. W., Giri, C. P., Wang, L., Zhu, Z. L., & Gillette, S. C. (2008). Identifying mangrove species and their surrounding land use and land cover classes using an object-oriented approach with a lacunarity spatial measure. *GIScience & Remote Sensing*, 45(2), 188-208.

Niphadkar, M., Nagendra, H., Tarantino, C., Adamo, M., & Blonda, P. (2017). Comparing Pixel and Object-Based approaches to map an understory invasive shrub in tropical mixed forests. *Frontiers in Plant Science*, 8, 892.

Okojie, J. (2017). Assessment of forest tree structural parameter extractability from optical imaging UAV dataset, *In Ahaus Germany*.

Pande-Chhetri, R., Abd-Elrahman, A., Liu, T., Morton, J., & Wilhelm, V. L. (2017). Object-based classification of wetland vegetation using very high-resolution unmanned air system imagery. *European Journal of Remote Sensing*, 50(1), 564–576.

Phillips, O. L., Aragão, L. E. O. C., Lewis, S. L., Fisher, J. B., Lloyd, J., López-González, G., … & Van Der Heijden, G. (2009). Drought sensitivity of the Amazon rainforest. *Science*, 323(5919), 1344–1347.

Qian, Y., Zhou, W., Yan, J., Li, W., & Han, L. (2015). Comparing machine learning classifiers for Object-Based land cover classification using very high resolution imagery. *Remote Sensing*, 7(1), 153-168.

Raczko, E., & Zagajewski, B. (2017). Comparison of support vector machine, random forest and neural network classifiers for tree species classification on airborne hyperspectral APEX images. *European Journal of Remote Sensing*, 50(1), 144-154.

Repola, J. (2009). Biomass equations for Scots pine and Norway spruce in Finland. Silva Fenn. 43, 625–647.

Schowengerdt, R. A. (1997). Remote Sensing: Models and Methods for Image Processing. *Academic, San Diego, USA*.

Sedliak, M., Sačkov, I., & Kulla, L. (2017). Classification of tree species composition using a combination of multispectral imagery and airborne laser scanning data. *Central European Forestry Journal*, 63(1), 1–9.

Shrestha, R., & Wynne, R. H. (2012). Estimating biophysical parameters of individual trees in an urban environment using small footprint discrete-return imaging Lidar. *Remote Sensing*, 4(2), 484-508.

Shafri, H. Z. M., & Ramle, F. S. H. (2009). A Comparison of Support Vector Machine and Decision Tree Classifications Using Satellite Data of Langkawi Island. *Information Technology Journal*, 8(1), 64-70.

Shao, Y., & Lunetta, R. S. (2012). Comparison of support vector machine, neural network, and CART algorithms for the land-cover classification using MODIS time-series data. *ISPRS Journal of Photogrammetry and Remote Sensing*, 70, 78-87.

Thanh Noi, P., & Kappas, M. (2018). Comparison of random forest, k-nearest neighbor, and support vector machine classifiers for land cover classification using Sentinel-2 imagery. *Sensors*, 18(1), 18.

Van Mantgem, P. J., Stephenson, N. L., Byrne, J. C., Daniels, L. D., Franklin, J. F., Fulé, P. Z., & Veblen, T. T. (2009). Widespread increase of tree mortality rates in the western United States. *Science*, 323(5913), 521–524.

Wang, L., Sousa, W. P., & Gong, P. (2004a). Integration of object-based and pixel-based classification for mapping mangroves with IKONOS imagery. *International Journal of Remote Sensing*, 25(24), 5655-5668.

Wen, D., Huang, X., Liu, H., Liao, W., & Zhang, L. (2017). Semantic Classification of Urban Trees Using Very High Resolution Satellite Imagery. *IEEE Journal of Selected Topics in Applied Earth Observations and Remote Sensing*, 10(4), 1413-1424.

Woodcock, C. E., & Strahler, A. H. (1987). The factor of scale in remote sensing. *Remote Sensing of Environment*, 21(3), 311-332.

Wulder, M. A., White, J. C., Hay, G. J., & Castilla, G. (2008). Towards automated segmentation of forest inventory polygons on high spatial resolution satellite imagery. *The Forestry Chronicle*, 84(2), 221-230.

Zoehrer, F. (1980). Forstinventur. Ein Leitfaden fu¨ r Studium und Praxis. Pareys Studientexte 26. Verlag Paul Parey. *Hamburg und Berlin*. 207.

Detecting and Calculating the Soil Moisture Using Microwave Imagery (Case Study: Miyankale, Mazandaran)

Abolfazl Rahimabadi[a] [*], Ali Akbar Jamali[b]

[a]Department of GIS & RS, Yazd Branch, Islamic Azad University, Yazd, Iran
[b]Associate Professor, Department of GIS-RS and Natural Engineering, Maybod Branch, Islamic Azad University, Yazd, Iran

Abstract

Almost one third of the earth is covered by soil, which has several essential parameters. The soil moisture content is one of the essential parameters. The current research calculates the soil moisture content. There are known methods to calculate soil moisture; however, a new method has been chosen for this research. Microwave imagery is a novel appropriate way to detect and calculate the amount of moisture in soil. The SENTINEL-1 with SAR sensor has been a good satellite for research purpose. The microwaves sent by the satellite to the earth receives the backscatters which has been directly related to the amount of moisture. Thus four images were obtained at different time intervals of the year; 21st November 2015, 1st May 2016, 5th June 2016 and 29th September 2016. The study area of Miyankale is covered by four images. Furthermore, to calculate the moisture in Miyankale which was done by another method the results were finally compared with the percentage measured by satellite imagery. The accuracy of satellite data is confirmed by measuring the soil moisture by two different methods. The coefficient of determination R^2 has been chosen to compare the data and check the microwave imagery. The R^2 coefficient is able to compare two independent data. The R^2 coefficient is 0.82, 0.82, 0.78 and 0.81 for different time periods. The R^2 ranges from 0 to 1, as the R^2 values are closer to 1 the moisture obtained from SAR images is confirmed

Keywords: Backscatter Coefficient, Soil Moisture, SAR, Sentinel-1

---

[*] Corresponding author. Tel:.+98-9359405245.
   E-mail address: rahimabadi_abolfazl@yahoo.com.

1. Introduction

One of the soil parameters that would affect other parameters is moisture thus the focus of this research is calculating the amount of moisture of the soil. Although soil moisture has been measured through other researches, this research proposes and examines a novel method. The application of satellite data to measure the amount of moisture in the soil is a new method in Iran. The satellite sends the microwaves to the earth and receives the backscatters which are directly related to the amount of moisture. Few radar practical examinations are there which dedicates the soil parameters such as moisture (Altese et al., 1996). Among various satellite data, radar data is an appropriate data to extract the moisture percent in the soil (Behyar et al., 2014). In other words, radar spectrum is more capable than other electromagnetic spectrum to detect moisture in the soil. Therefore, radar satellite has been chosen to detect the soil moisture (Bao et al., 2018). The Sentinel-1 with SAR sensor, which produces and sends radar waves to the earth and receives the backscatter in return from earth features (Thain et al., 2011). This research choses a new method of radar imagery by downloading several images of Sentinel-1, to calculate the soil moisture. Determination of soil moisture is important for agricultural products (Potin et al., 2011).

The method employed to extract soil moisture will be explained. The images were processed to map soil moisture parameters of the case study and to determine the amount of moisture in each image.

In order to retrieve the soil surface parameters, an algorithm has been investigated and implemented. Soil parameters such as moisture and roughness are used in various fields (Lievens et al., 2017). SAR (Synthetic aperture radar) capability to measure the soil parameters is known for more than 30 years however, scientists are still searching for appropriate sensors and applicable algorithms to restore the soil parameters (Mirmazlumi, 2014). For instance, European Space Agency (ESA) scientists have used radar wavelength with the SMOS (Soil Moisture and Ocean Salinity), in order to measure two variables: soil moisture and salinity of the oceans (Mecklenburg, 2015). Radar images have two sections included power and phase (backscatter), which are used to determine the moisture content of the soil. Literally, the hypothesis of the research is the relation of backscatter and moisture where humidity is expected to be directly related to backscatter. This research has modeled the changes in radar images. Radar wavelengths are able to detect the difference content of the moisture in soil. The main purpose was to employ a new method with a high resolution data, while it benefited the research by decreasing time and cost. Finally, the results obtained with these wavelengths will be analyzed and mapped in the case study of Miyankale.

1.1. Soil Surface Parameters

Generally, soil surface parameters can be subdivided into three categories:

1. Surface roughness parameters: These parameters include the distribution of ground targets, surface profile height, autocorrelation function and surface roughness criteria.
2. Soil properties: Surface roughness, water capacity, depth of penetration and macro-level structure are included in this category.
3. Vegetation characteristics: The vegetation structure and geometry of the plant, along with the water capacity of the plant are the most important parameters of this category (Mirmaslomi, 2014).

1.2 Literature Review

Ebrahim Babayan et al. (2013) used ASAR images to estimate soil moisture content and also TDR humidifier to validate the data. It was concluded that the GM mode of ASAR images is more appropriate to be used in semi-arid and undercoats conditions to estimate soil moisture content. Dr. Entekhabi's methodology was developed in 1994. Dual soil moisture model and heat loss model are employed to measure moisture and surface temperature. These measurements were processed and used to estimate the moisture and then were generalized to the depths of surface. Foson Balik et al. (2008) used the backscatter waves of ASAR, PALSAR and RADARSAT-1 radar sensors, to measure soil moisture 86%, 76% and 81%, respectively. Balik compared different polarizations of three sensors and concluded that in spite of better

spatial resolution 30*30 meter of ASAR image, the results are almost the same in the study area Izmir of Turkey. Also, Saloni et al. (2008) compared the accuracy of ASAR images (band C, HH and VV polarization), RADARSAT-1 and PALSAR (L band, HH polarization) to estimate soil moisture content in agricultural land in western Turkey. According to their results, the relationship between soil moisture content and backscatter coefficient of soil was $R^2 = 0.77$, 0.81 and 0.86, respectively. In another study, Brocka et al. (2011) used the passive microwave data of the AMSR-E sensor of Aqua satellite and ASCAT sensor of MetOP Satellite to measure moisture content of the soil surface, with correlation coefficients of (R) 0.71 and 62.2, respectively. Baghdadi et al. (2012) estimated the soil moisture content in vegetation-free conditions with a precision of 3% using the TERRASAR-X test data. Lyons and Verhoest (2012) detected the correlation between RADARSAT-2 data in HH and VV polarizations. The IEM[*] model estimated the soil moisture content, with the RMSE equal to 0.04 (cubic centimeter per cubic centimeter). Kulas et al. (2016), found improvements in detecting soil moisture in the ranges of 5 to 19 percent. In an investigation which they worked on microwave satellite data for the assessment of soil moisture, it was found that if active satellite (ASCAT) and passive (AMSR) data were used complementarily, a significant improvement would be obtained. Lyons et al. (2017) did the same study by two observations. Both active radar (ASCAT) and passive (SMOS) considered to observe backscatter coefficient and lighting temperature. Lyons found out that combining these parameters would estimate the soil moisture in depth of 0-10 cm with a great accuracy of 0.548.

2. Materials and Methods

The research is based on two types of data; field data and satellite data. The field data examined soil in the case study in order to measure the amount of soil moisture. These field measurements were necessary to be done to compare with the moisture obtained by radar images. In further section would be cleared the relationship between field data and satellite data First of all, the case study has been introduced.

2.1 Study Area

Behshahr city is located in the mountainous foothills of Alborz Mountains with two mountainous and plain areas. It extends from 36 degrees, 45 minutes to 36 degrees and 88 minutes longitude, and 53 degrees and 21 minutes to 54 degrees 13 minutes latitudes. Miyankale Peninsula is located in this city as a plain district next to the Caspian Sea. The Miyankale is a narrow Peninsula where reached to the Caspian Sea from the north, and reached to the narrow, shallow Gorgan Gulf from the south. It restricted by Raghmarz wetland from the west and narrow strait of less than one kilometer in the neighboring port of Turkmen from the east.

The area of Miyankale is a unique area of about 68 thousand hectares. The average altitude of this area is 30 meters below the sea level, and its annual rainfall is 717 mm. Miyankale is located in a warm, humid climate. The terrestrial ecosystem consists of sandy hills of the Pomegranate trees, berry bushes, Sazil (Local vegetation) bushes and grassland region. These various vegetation areas are not uniform and are dense in some hectares but thin in others.
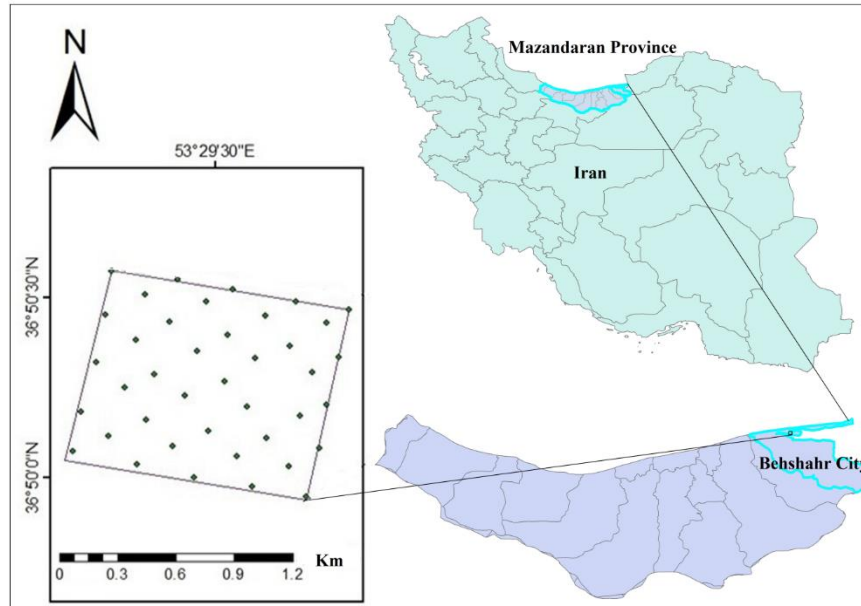
Figure 1. Case study of Behshahr

2.2. Field Data

Besides processing satellite data, the field data were collected in 1 km^2 area, considered to be checked in soil moisture. The observed moisture content was calculated in depth (1-10) centimeters. Forty samples were obtained in different location. The samples were kept in specific metal dish in order to transfer to the soil laboratory. The soil laboratory measured the percentage of moisture content. The location of each sample point was recorded by the GPS device Figure 2. Another point to be noticed is the different types of sampling. The soil differed from sand to gravel and vegetation types in sampling positions varied from thin to dense grass to a height of 10 centimeters. It should be considered that, during software processing, the effect of vegetation was removed.
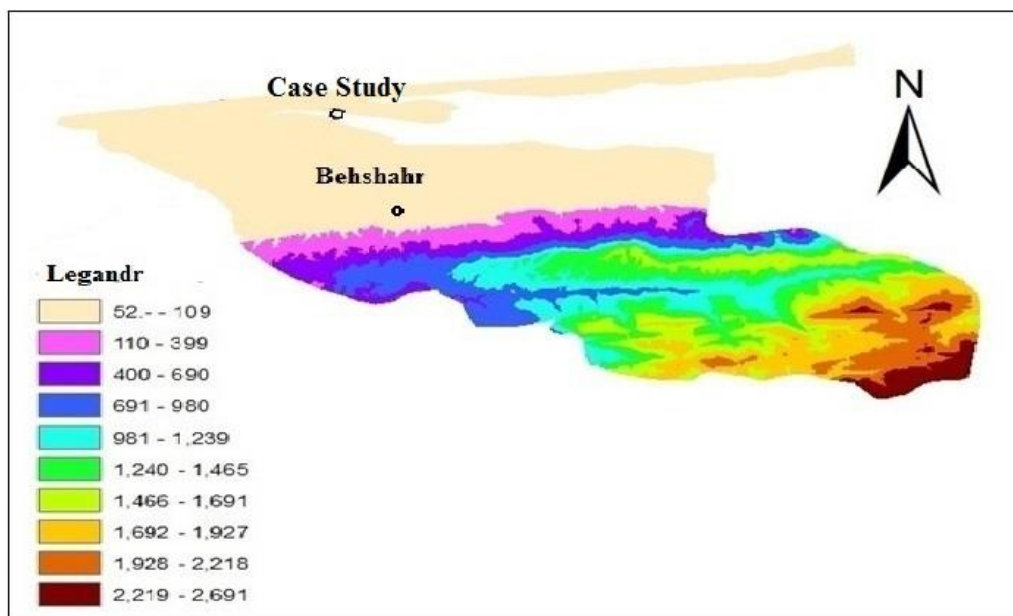

Figure 2.DEM of Behshahr; (Authors)

2.3. Satellite Data

Two satellites were considered to employ their images; LANDSAT-8 and SENTINEL-1. As long as SENTINEL-1received all the radar backscatters from the ground, it was necessary to delete the vegetation backscatter. The impact of vegetation had to be eradicated then the radar images were processed to measure the soil moisture. The NDVI (Normalized Difference Vegetation Index) is a vegetation index which obtained by LANDSAT-8. Three Landsat-8 images were downloaded in approximately the same date of the radar images. LANDSAT-8 images were preprocessed then processed to calculate the vegetation density in the case study of Miyankale Peninsula. The NDVI index was calculated in order to measure, the LAI (Leaf Area Index) equation (1):

$$LAI = 0.57 * \exp(2.33 * NDVI)) \tag{1}$$

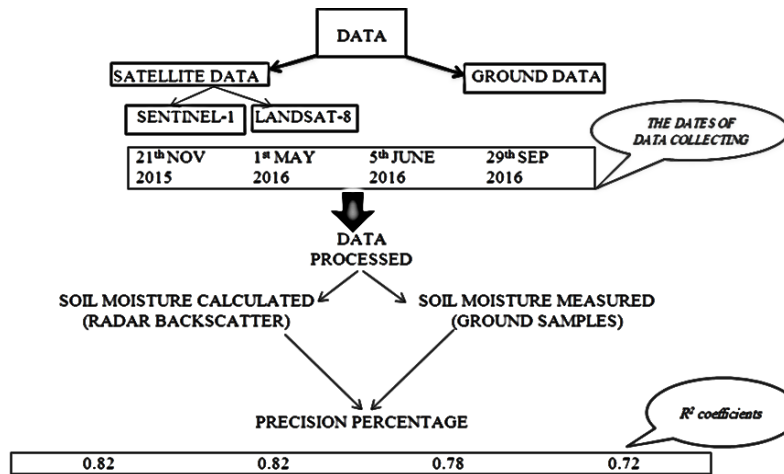In Figure 3 the methodological flowchart of this research is indicated

Figure 3. Flowchart of the research (author)

2.4. Methodology

The European Space Agency is an open source to get the Sentinel-1 images. These are high resolution images with a large frame size of 40,000 pixels * 40,000 pixels. First of all orbital correction is exerted to the image. There are two types of correction files, POEORB, RESORB. The RESORB file is easier to access rather than other file. It could be downloaded in less than a day; however, the POEORB orbit took longer period but it was more accurate. Thus the POEORB file was used in this research. The next step was to remove the thermal noise and then the image was calibrated by Sigma0 band. As long as the pixel size is half of the SAR image resolution, the image's speckle was removed by making multilook of the image.

Each pixel is the result of a total of backscatter to the satellite, and each backscatter has a different phase. Therefore, the interference of these waves causes the formation of dark or bright spots in the final image. This created noise, such as salt and pepper, is sprayed on the images; it is an unavoidable error in coherent systems Figure 4.

For each pixel, γ (x, r) is equal to the sum of the backscatter (2):

$$|u(x_0, r_0)| = |\gamma(x_0, r_0) * u_0(x, r)| = |\Sigma \gamma_i(x_0, r_0) * u_0(x, r)| \tag{2}$$
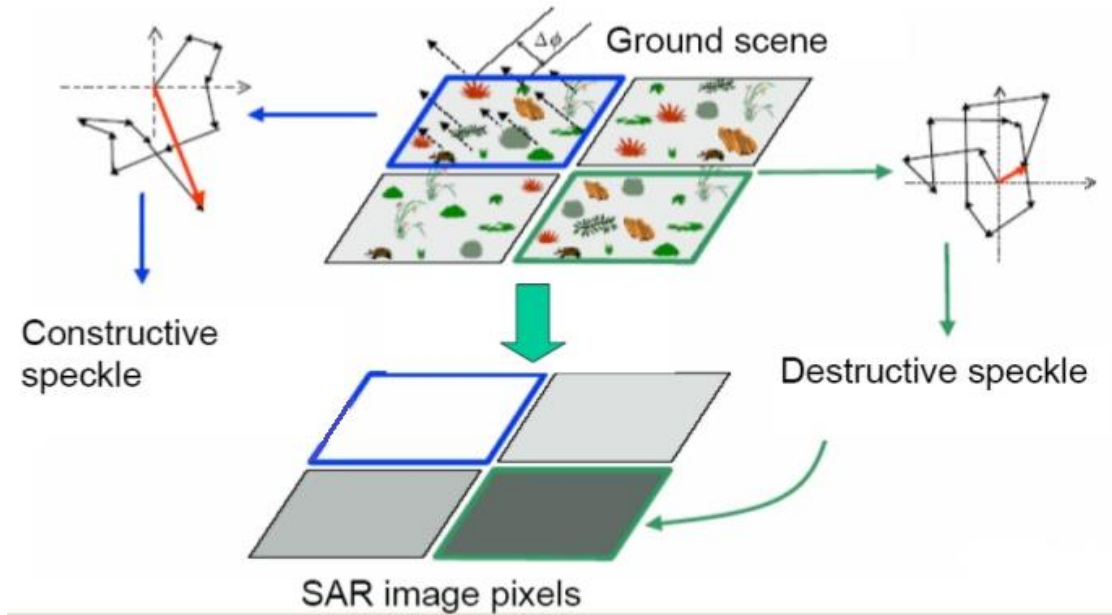
Figure 4. Backscatter of each pixel (Mincla, 2016)

The effects of speckles on the image degraded the quality hence making it more difficult for the interpretation. According to the Figure 5, as the backscatter increased, the speckle would increase too.
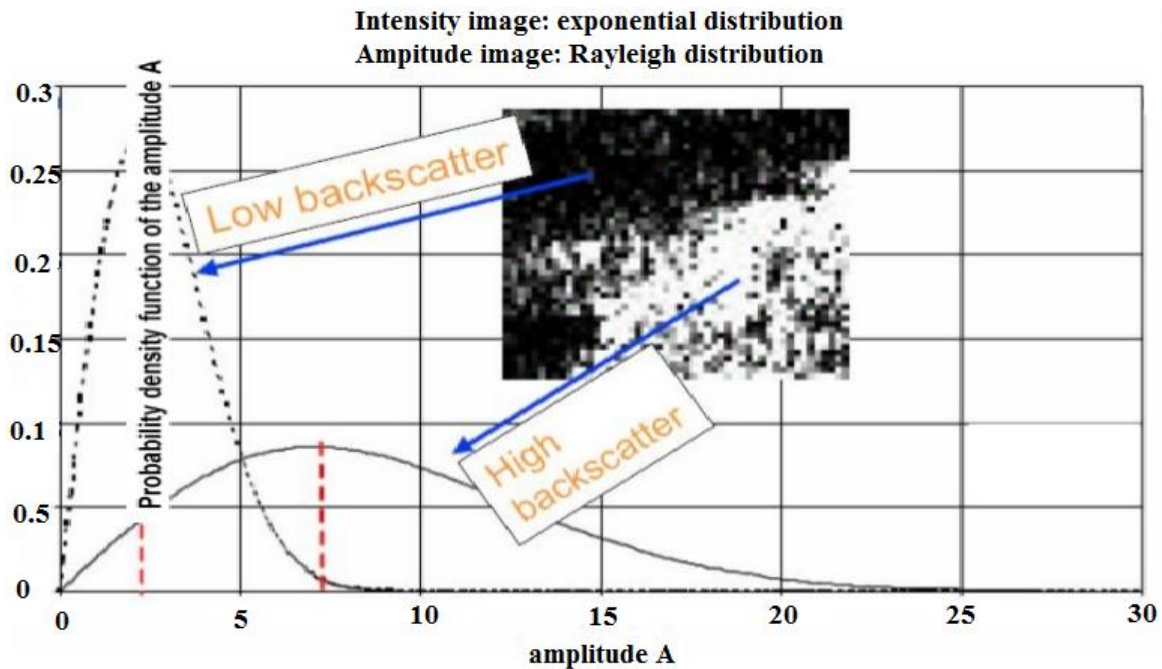
Figure 5. Relationship between word and image and postback (Mincla, 2016)

In this paper, the Moody's filter was used (Babayan, 2013) to remove speckles. As the multilook increased, the probability distribution function narrowed. The narrow function corresponds to the speckle reduction in the image (Mincla, 2016). The speckles of the images were removed using different date of imagery of the same place. In other word, various images of the case study at different time were the solution for detecting speckles. In the next procedure geometric correction, georeference and normalization of the

slope of the area were exerted. The slope is corrected by the Band Math operator shown in quotation (3). Now the sigma zero (Sigma Nought) (σ °) of the region is calculated by multiplying backscatter of the reference ellipse to the sinusoidal fraction in Figure 6. The θ_{DEM} is the angle of the radar wave with the digital elevation model and θ_{ELL} is the angle of the wave with the reference ellipse.

$$\text{Area:} \sigma°\text{Norm} = \sigma°\text{Ellipsoid} * \frac{\text{Sin}\theta\text{DEM}}{\text{Sin}\theta\text{Ell.}} \tag{3}$$
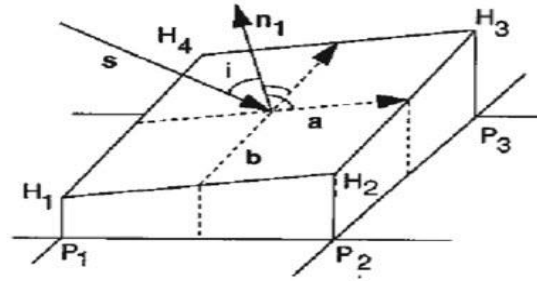

Figure 6. Reflection related with the gradient of its reflection surface (Mincla, 2016)

The radar image is composed of phase or power that should be converted to a user-friendly image. How to display the Sentinel image depends on the received geometry. After processing the image data in Figure 7, it was time to estimate the moisture content and the backscatter relationship with the moisture content of the studied area and vegetation density.
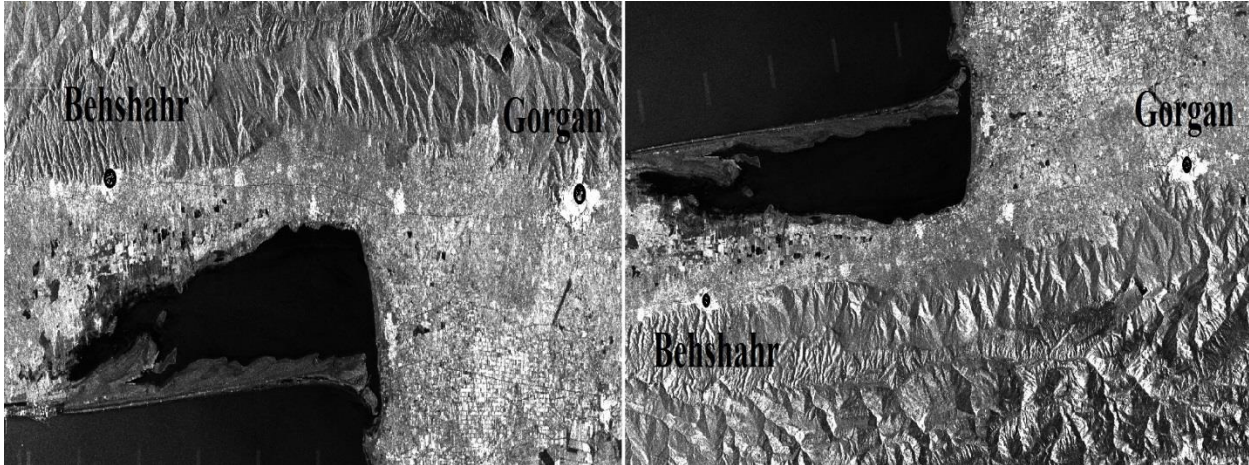
Figure 7. Right image is the final processing (Authors)

The backscatter of the earth surface was obtained using equation (4); Where $\sigma_s°$ soil backscatter and $\sigma_{dv}°$ plants backscatter, and also $\sigma_{int}°$ is the backscatter of the plant and soil. The plant backscatter is derived from equations (5) and (6) where τ^2 is the portion of light which transferred of the vegetation surface and LAI is the leaf area index. The angle θ is declination of the sensor (Moren, 2005).

$$\sigma° = \tau\sigma_s° + \sigma_{dv}° + \sigma_{int}° \tag{4}$$

$$\tau^2 = \exp(-2\text{LAIsec}\theta) \tag{5}$$

$$\sigma_{dv}° = \text{LAIcos}\theta(1 - \tau^2) \tag{6}$$

3. Results and Discussion

The coefficient of determination, denoted R^2 "R squared", is used to compare independent variable(s). The research had two types of data which were also independent; first group were field measurements and the second one were images calculation. It should be considered that these two types of data were prepared independently in order to be compared. The calculation of R^2 coefficient is an appropriate method to compare these data. The research chose this method to examine the correctness of moisture percent extracted form SAR imagery. Since the field moisture was measured correctly, the R^2 coefficient determined the correctness of moisture measurements on SAR images. In other words, R^2 is capable of determination of SAR imagery whether it detected the soil moisture in a correct way or not. The coefficient of determination ranges from 0 to 1. As the R^2 value became closer to 1, the moisture obtained from SAR images was confirmed.

3.1. Comparison of Surface Reflection Coefficients and Observation of Humidity

The coefficient (R^2) is 0.82, 0.82, 0.78, 0.72, and 0.81 for different time periods were obtained as shown in Table 1. The difference between these two variables can be due to the backscatter received by the sensor, which included the polarization and the soil's types (Altis, 1996).

The coefficient (R^2) obtained from the diagrams indicated that the coefficient of determination differed from 0.72 to 0.82 due to the moisture content and backscatter in different time series. The least amount of R^2 is for VH polarization. Also, for the coefficient of determination, different results were obtained, which will be described below.

Table 1. Results of RMSE and R^2 coefficient and moisture variables observed in different time series (Authors).

R^2	RMSE	Polarization	Date
0.82	0.35	VV	11/21/2015
0.82	1.06	VV	5/1/2016
0.78	1.49	VV	6/5/2016
0.72	1.75	VH	6/5/2016
0.81	0.68	VV	9/29/2016

3.2. Comparison of Backscatter Coefficient with Vegetation (NDVI)

The relationship between vegetation and wavelength is important in detecting soil moisture, as the wavelength must pass through vegetation as the main obstacle and reach the soil. According to Babaeiyan et al, if the plant biomass is less than 0.5 kg / m^2, the vegetation effect can be ignored on the total backscatter coefficient (Das, 2008). In hot seasons, when the dehydration is high, vegetation is noticeably reduced and less correlated with backscatter. Thus it was proved that C band was affected by vegetation. In the studied area, the effect of vegetation was eliminated due to a variety of vegetation and its effects on backscatter.

3.3. Distribution of Backscatter in Time-Spatial Dimension

The normalized total backscatter was shown in 15 meters pixels during the study period. As seen, the total backscatter was affected by vegetation area. It should be noticed that the backscatter is obtained from the northern, northeastern and western parts of the region as it is shown in Figure 8, where there were more vegetation and thus more soil moisture (Mesri, 2013).
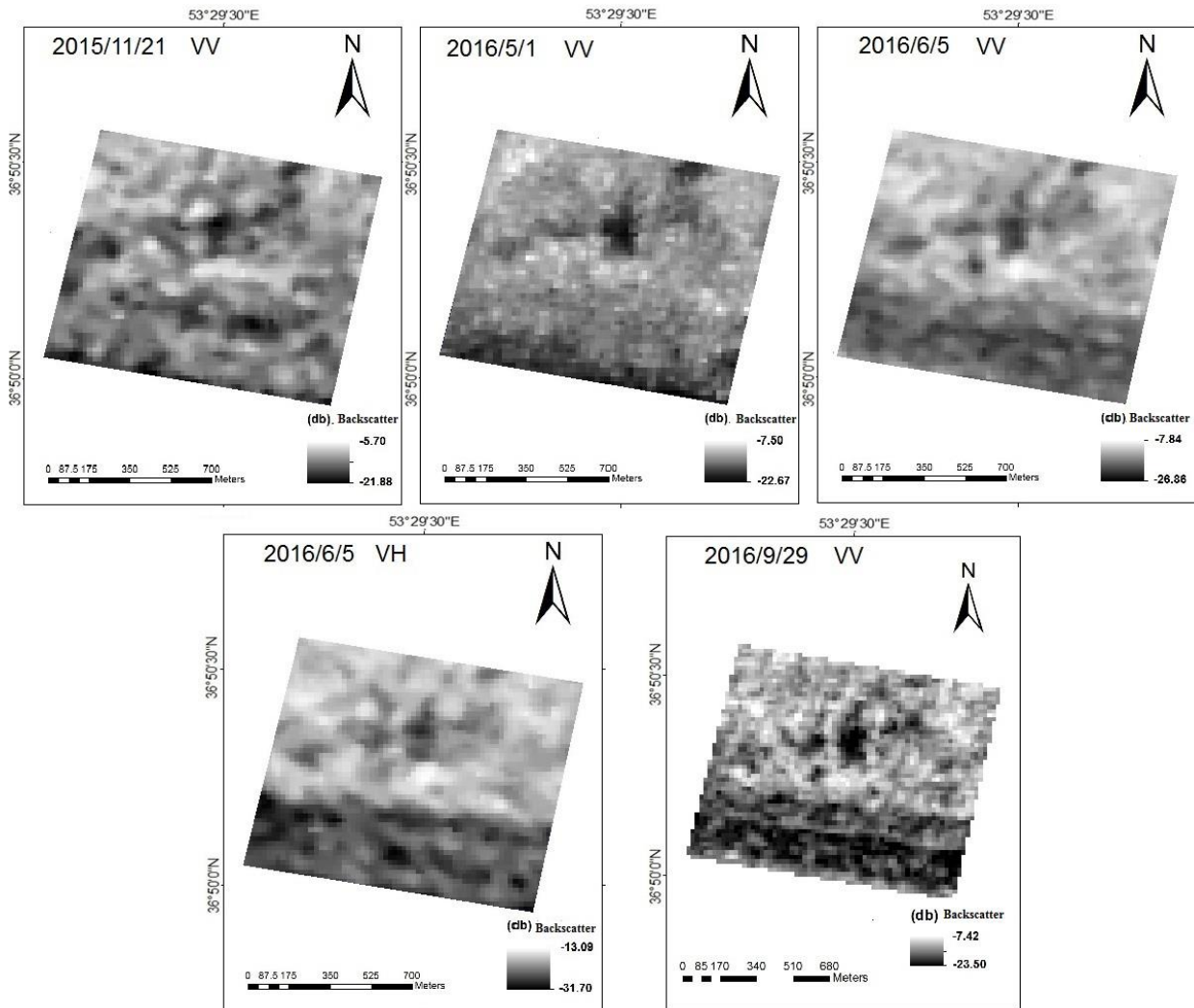
Figure 8. Time-spatial distribution of the total backscatter (1 * 1 km) (Authors)

3.4. Precision Testing

Based on the results, the R^2 value was between 0.72 and 0.82, as well as RMSE between 1.75 and 0.35. The RMSE value was approximately dependent on the month or season of the year. In other words, during low rainfall season, RMSE is somewhat diminished, as the effect of vegetation on backscatter. While Babaian et al. calculated 0.68 for R^2 based on surface soil moisture with ASAR images and HH polarization, the current research results in the VH and VV polarization, were above 0.70%. In addition, Salon et al. calculated moisture content using C-band with HH and VV polarization then reached to R^2 coefficients equal to 0.77, 0.81, and 0.88, which was approximately the same as this research.

In general, region vegetation diversity was very crucial and determined the accuracy of R^2 coefficient. In the study of Nazari Aghdam, with satellite optic data, there was a high correlation between soil moisture content and NDVI. Therefore in this study, there were no needs for images in visible wavelengths. In Khanmohammadi's research, vegetation indices such as NDVI, NDMI and LST employed using MODIS satellite data to extract soil moisture content. Although measuring soil moisture in Khanmohammadi's research definitely affected by vegetation areas; its precision was not good enough compared to this research. According to Figure 9, the moisture content of the whole Mmiyankale Peninsula was mapped based on each image on SAR sensor.
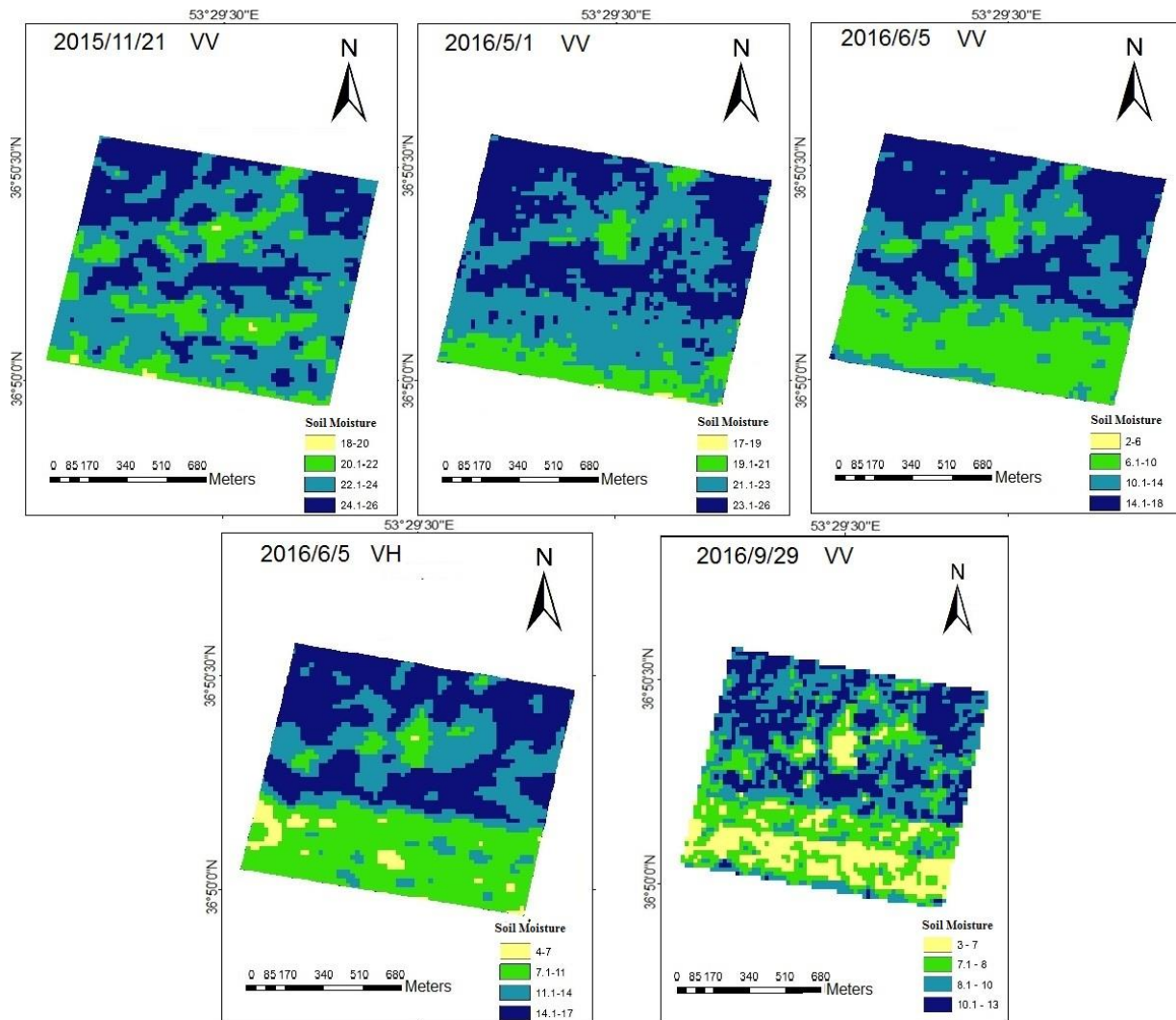
Figure 9. Time-Spatial distribution of soil moisture content 1 * 1 km (Authors)

4. Conclusion

There were a few radar practical examinations which dedicated the soil parameters such as moisture. The radar data is an appropriate data to extract the moisture percent in the soil. In this research, a simple experimental model proposed which was based on the backscatter data in GM mode of the Sentinel satellite. Balik et al. (2008) used the backscatter waves of ASAR, PALSAR and RADARSAT-1 radar sensors, to measure soil moisture 86%, 76% and 81%, respectively. Also, Saloni et al. (2008) compared the accuracy of ASAR images, RADARSAT-1 and PALSAR then figured out the relationship between soil moisture content and backscatter coefficient of soil was $R^2 = 0.77$, 0.81 and 0.86, respectively. Baghdadi et al. (2012) estimated the soil moisture content in vegetation-free conditions with a precision of 3% using the TERRASAR-X test data. Babayan et al. (2013) used ASAR images to estimate soil moisture content and also TDR humidifier to validate the data. It is concluded that the GM mode of ASAR images is more appropriate to be used in semi-arid and undercoats conditions to estimate soil moisture content. Behyar and Mirmazlumi have done in two independent researches in 2014. Also, Bao has done the same in 2018 by radar satellite to detect the soil moisture.

The current research chose the radar method based on SAR sensor capability to measure soil parameters. The time-spatial model was proposed to retrieve, monitor, and mapping soil moisture of the earth surface. The regression model estimated the soil moisture content in the study area through the R^2 coefficient and RMSE calculations. The results of the evaluation and validation of the model showed that there is slight difference between the soil moisture content and the measured values. Due to the lack of coherent data of soil moisture in Iran country, especially in crucial agricultural sites, employing the SAR data from the GM model would be an effective novel method. In this regard, it is recommended to use long-wavelength bands for vegetation areas. The coefficient (R^2) is 0.82, 0.82, 0.78, 0.72, and 0.81 for different time periods were obtained as shown in Table 1. The difference between these two variables can be due to the backscatter received by the sensor.

References

Altese, E., Bolognani, O., Mancini, M., & Troch, P.A. (1996). Retrieving soil moisture over bare soil from ERS1 Synthetic Aperture Radar data: sensitivity analysis based on theoretical surface scattering model and field data. *Water Resources Research Journal*, *32*(3), 653-661.

Babayan, A., Homaei, M., & Nowruz, A.S. (2013). Estimation of surface soil moisture using ENVISAT / ASAR radar images. *Water Research in Agriculture Journal*, *(27)*4, 622-611.

Baghdadi, N., Aubert, M., & Zribi, M. (2012). Use of TerraSAR-X data to retrieve soil moisture over bare soil agricultural fields. *IEEE Geoscience and Remote Sensing Letters, 9*(3), 512-516.

Bao, J., Hou, Z., Ray, J., Huang, M., Swiler, L., & Ren, H. (2018). Soil moisture estimation using tomographic ground penetrating radar in a MCMC–Bayesian framework. *Stochastic environmental research and risk assessment, 32*(8), 2213-2231.

Behyar, M. B. (2014). Evaluation of Soil Moisture in Isfahan Province by AMSR-E. *Geographical Research (1017-4125), 29*(1).

Brocca, L. S., Hasenauer, T., Lacava, F., Melone, T., Moramarco, W., Wagner, Dorigo, w.(2011).

Assimilation of the ASCAT soil moisture product for flood prediction and forecasting. *EUMETSAT/ESA scatterometer science conference.*

Das, N. N., Mohanty, B. P., & Njoku, E. G. (2008). A Markov chain Monte Carlo algorithm for upscaled SVAT modeling to evaluate sattelite-based soil moisture measurements. *Water Resources Research, 44*(5).

Entekhabi, D., Nakamura, H., & Njoku, E. G. (1994). Solving the inverse problem for soil moisture and temperature profiles by the sequential assimilation of multifrequency remotely sensed observations. *IEEE Transactions on Geoscience and Remote Sensing, 32*(2), 438-448.

Khanmohammadi, F., Homaei, M., & Nowruz, A. S. A. (2014). Estimation of soil moisture using vegetation indices and soil temperature and normalized moisture index using MODIS Images. *Journal of Soil and Water Resources Conservation*, *2*(4), 1-9.

Kolassa, J., Gentine, P., Prigent, C., & Aires, F. (2016). Soil moisture retrieval from AMSR-E and ASCAT microwave observation synergy. Part 1: Satellite data analysis. *Remote Sensing of Environment, 173*, 1–14.

Lievens, H., & Verhoest, N. E. C. (2012). Spatial and temporal soil moisture estimation from RADARSAT-2 imagery over Flevoland, The Netherlands. *Journal of Hydrology*, *456*, 44-56.

Lievens, H., Martens, B., Verhoest, N.E.C. Hahn, S. Reichle, R.H., & Miralles, D.G. (2017*).* Assimilation of global radar backscatter and radiometer brightness temperature observations to improve soil moisture and land evaporation estimates. *Remote Sensing of Environment 189,* 194–210.

Mecklenburg, S., Drusch, M., Kaleschke, L., Rodriguez-Fernandez, N., Reul, N., Kerr, Y., Font, J., Martin-Neira, M., Oliva, R., Daganzo-Eusebio, E., Grant, J.P., Sabia, R., Macelloni, G., Rautiainen, K., Fauste. J, de Rosnay. P, Munoz-Sabater. J, Verhoest. N, Lievens, H., Delwart, S., Crapolicchio, R., de la Fuente, A., & Kornberg, M. (2015). ESA's Soil Moisture and Ocean Salinity mission: From science to operational applications. *Remote Sensing of Environment, 180,* 3-18.

Minchella, A. (2016). SNAP Sentinel-1 in a Nutshell, – "ESA SNAP-Sentinel-1 Training Course" *Satellite Applications Catapult - Electron Building, Harwell: Oxford.*

Mesri, A., Kamkarrowhani, A., & Arab Amiri, A. (2013). Determination of Soil Moisture Content Using GPR Method and Comparison of Results with Laboratory Results, Case Study: Shahroud University Agricultural University Campus. *8th Conference of Engineering and Environmental Geology of Iran, Ferdowsi University of Mashhad*, p.7.

Moran, M. S., Peters-Lidard, C. D., Watts, J. M., & McElroy, S. (2004). Estimating soil moisture at the watershed scale with satellite-based radar and land surface models. *Canadian journal of remote sensing, 30*(5), 805-826.

Myrmzlomi, S.M., & Sahebi, Mrs. (2014). Estimation of soil moisture content using SAR data with emphasis on surface re-diffusion models. *PhD thesis of Civil Engineering, Mapping Engineering, Khaje Nasir-e-Din Tusi University of Technology*, P.110.

Nourouzi, A. E., Behbahani, S., Rahimi, K. A., & Aghighi, H. (2008). Surface Soil Moisture Model with NDVI (Case Study: Rangelands of Khorasan Province), *Journal of Environmental Studies*, *48*, 127-136.

P., Matgen, J., Martínez-Fernández, P., Llorens, J., Latron, C., & Martin, M., (2011). Soil moisture estimation through ASCAT and AMSR-E sensors: An intercomparison and validation study across Europe. *Remote Sensing of Environment, 115*(12), 3390–3408.

Potin, P. (2011). Sentinel-1 Mission Overview Advanced Course on Radar Polarimery*, ESRIN, Frascati*.

Sanli, F.B., Kurucu, Y., Esetlili, M. T, & Abdikana, S. (2008). Soil moisture estimation from RADARSAT-1, ASAR and PALSAR data in agricultural fiels of Menemen plain of western Turkey. *The International Archives of the Photogrammetry, Remote Sensing and Spatial Information Sciences*. Part B7, Beijing.

Silva, A. T., Portela, M. M., Naghettini, M., & Fernandes, W. (2017). A Bayesian peaks-over-threshold analysis of floods in the Itajaí-açu River under stationarity and nonstationarity. *Stochastic environmental research and risk assessment*, *31*(1), 185-204.

Thain, C., Barstow, R., Ramsbottom, D., Lim, P., & Wong, T. (2011). Sentinel-1Product Specification, Ref: S1-RS-MDA-52-744, *Issue/Revision*: 2/2.

Rockfall Detection Using Differential Interference Synthetic Radar Technique from Sentinel-1 Satellite Imagery (Case study: Haraz road)

Omid karimi[a], Seyyed Ali Almodaresi[b]*

[a]*MS in GIS, Remote Sensing, Yazd Branch, Islamic Azad University, Yazd, Iran*
[b]*Associate professor, GIS and RS Department, Yazd Branch, Islamic Azad University, Yazd, Iran*

Abstract

Massive material movements are natural geomorphic processes. This process refers to separation and downward transportation of soil and rock materials under the influence of gravity and causes the transfer of a large amount of material, such as pebbles. In Iran, the given climate, geology and topography, massive movements, debris, conditions results in low altitude areas, significant casualties, financial and environmental damages. Modeling physical processes of rockfall calls for examining the fracture of rocky elements, dimensional fall or jump, crushing, rotation, or slipping and the final subsidence, regardless of the volume constraints of rockfall which are defined by their high energy and mobility. Dynamic processes of rockfalls are overshadowed by spatial and temporal distribution properties, including the disruption conditions, geometric and mechanical properties of the rock blocks and rocky slopes. One of the most suitable methods for identification of rockfall phenomenon is using radar interferometry (D-INSAR) technique. The study examined Haraz road with twelve Sentinel 1 sensor images from March to May 2016. Then, using an interferometry technique of radar with artificial aperture, the rockfall rate of SAR data related to Sentinel 1 sensor was measured, obtained in high and low pass modes. In addition, three rockfalls registered on March 20, 2015, March 31, 2015, and May 10, 2015 were examined in this study. The results showed that the rockfall times in all three pilot maps of displacement have significant changes compared to the unchanged times in the images. Using radar satellites and differential interferometry techniques, one can detect the amount of rockfall and its location.

Keywords: INSAR, Rockfall, Hezar Road, Sentinel 1, Ascending, Descending

---

* Corresponding author. Tel: +98-9131526455.
  E-mail address: almodaresi@iauyazd.ac.ir.

1. Introduction

The incidence of natural disasters causes significant damage to life, financial and environmental impacts throughout the world every year. Massive motions are specific forms of nature and incidents of range processes caused by geomorphologic, hydrologic and local geological conditions. These conditions along geodynamic processes, vegetation, land use, amount, intensity, and continuity of rainfall and earthquakes can end in the formation of rockfall (Madaldost, 2008).

Rockfall involves the sudden or rapid movement of loosen blocks or a set of hard stones separated from sloping rocky walls that usually occurs along the layers of the joints and fault zones or fault surfaces (Chayo, Tang and Wang, 2004). Rockfall is one of the most common forms of slopes in mountainous areas with its distinction from other instabilities being high and sudden incidence. Thus, rockfall is among the most devastating massive movements ending in loss of life and heavy damages.

In most cases, the hazards of rockfall cannot be nullified as the occurrence of such dangers are diverse spatially and temporally. Basic statistics methods, are mostly done with the help of computer modeling, has become a standard tool for evaluating the risk of rockfall and designing protective measures. The modeling of the physical processes of rockfall needs examination of the fracture of the rocky elements, falling or jumping, and dimensional jump, crushing, rotation, or slipping and final subsidence Hutchinson (1998), Evans and Hanger 1993, and Gazeti et al. (2002). Regardless of the volumetric constraints, rockfalls are characterized by their high energy and mobility. Dynamic processes of rockfalls are overshadowed by spatial and temporal distributions, like fracture conditions, geometric and mechanical features of rocky blocks and rocky slopes (Jaboudov et al., 2005).

The rockfall causes damages, blocks roads and razes the villages and fields to the ground. Among 368 rockfalls in Hong Kong from 1984 to 1996, 35% have caused obstruction or damage to roads, 22% damage or evacuation of buildings, 21% roadside obstruction and 6% damage to the car and public services. Only 15% of these incident occurred on the open ground, leading to negligible effects on human activities. The studies on rockfalls and evaluation of their danger in various areas can be found in the studies of Batterson et al. (2006), and Binal and Ercanoglu (2010). In Iran, in his master thesis, Gholami (2004) located rockfall risk using geographic information and remote sensing along Haraz Road from Vana to Plor. The study considered four factors of petorolgy, gradient, elevation relative to the road surface, and distance between driver's view to make decisions and react to falling rocks. Ghazipour et al. (2006) used the theory of cone of depression in evaluating the risk of rockfall. In the study of Chalus road (Zangouleh Bridge to Marzanabad), it was shown that the risk of rockfall has a direct relationship with the slope of the rocky slopes and its topographic conditions. Moreover, the type of the rock has an important role in the expansion and formation of rockfall.

In Iran, studies on the zoning of slopes are recent and their serious start dates back to the early 90s and 2000. Here are some of the studies in Iran. Gholizadeh (2010) examined the rockfall potential in Zangbar of Macau using 18 parameters and field observations and using the fuzzy model. Golizadeh concluded that gamma operator 0.7 is the most suitable operator in determining the capability of falling in the studied basin. Using cluster analysis method, Esfandiari Dorabadi and Hashemi (2012) tried to map the risk of fall in Paveh communication pathway, stating that human factors such as land use change, vegetation decline, change in slope geometry, and communication paths on the slopes cause fall in the region.

Lan, Martin, Julio and Leim (2010) used a three-dimensional LIDAR data model to evaluate the risk of fall along the Canadian Iron Canal and used microscopic records to calibrate physical processes. They introduced a high-resolution digital model based on LIDAR data comprehensively. Dauart and Marquauens (2002) studied the spatial distribution of regional scale loss using topographic data in the GIS, and concluded that the combination of falls with geological map and digital land model led to a strong correlation between the fall and petrology, altitudes, altitudes, slopes, rock walls and waterways. Regarding this, it is necessary to provide suitable measures for environmental and regional planning in the study area by identifying the risk of collapse hazard assessment with radar interferometry, while providing solutions to reduce damage.

Radial differential interferometry is an effective method for measuring the displacement of ground surface. Thus, using this technology, it is possible to closely monitor the movements of the ground surface continuously, with high precision and in a wide range. Given the extensive coverage of satellite images, synchrony and being low cost compared to other field methods, the use of this technology is very common in the study of natural hazards of the ground like landslides, subsidence, quakes and volcanic activity. Radar

interferometry capability in landing detection and tracking have already been reported by Gabriel et al. (1989) and Massonnet and Feigl (1998). Indeed, recent progresses in radar surveillance such as differential interferometry (DInSAR) have attracted the attention of many researchers and experts involved with landslide monitoring and assessment of environmental hazards, and the ability of this technique to detect and monitor landslide motions in various studies has been reported by Rott et al. (1999) Strozzi et al. (2005). In this paper Rockfall detection using differential interference synthetic radar technique from Sentinel-1 satellite imagery is investigated.

2. Materials and Methods

2.1. The Study Area

Road 77 or Haraz Road, along Road 59 (Karaj-Chalous), is the main road of Tehran-Mazandaran. This road passes through the valley of the Haraz River and is the closest main road to Damavand summit. This road describes the history of the enormous Alborz, Damavand, Amol and Iran. Moreover, the road is the shortest route between Tehran and Amol. It is estimated that only in Nowruz festival, the road hosts 5 million passengers. The Haraz road has 14 tunnels, with the longest one being over 1500 meters long. The construction of this road took 23 years (Figure 1).
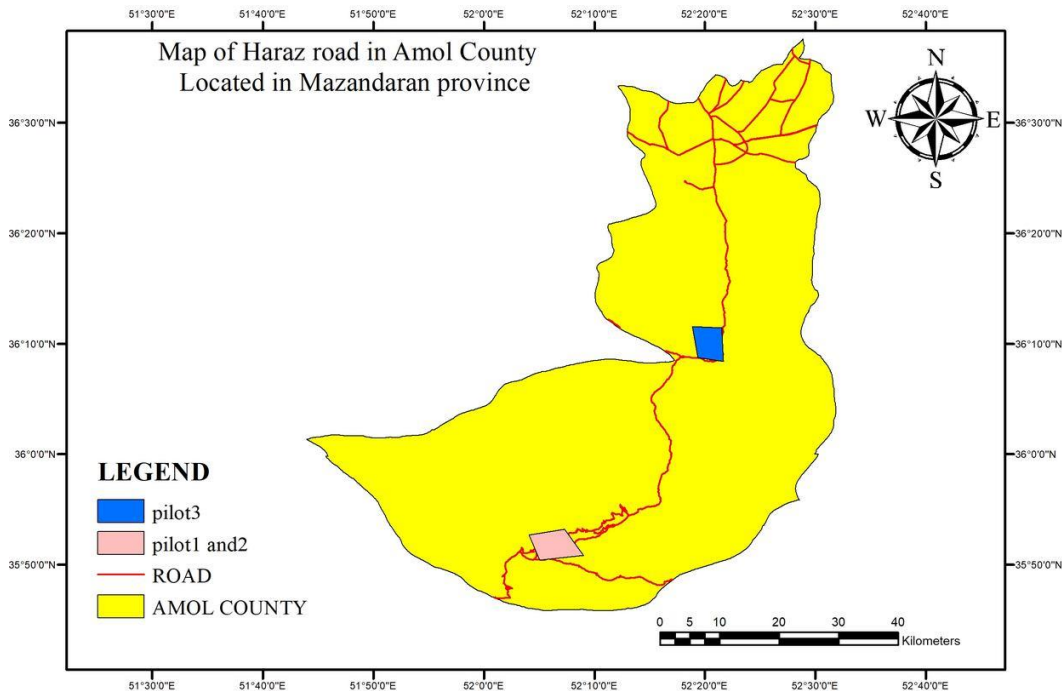

Figure 1. The studied area

2.2. Data

The data used in this study falls into general data of land and satellite data. The satellite data is collected from the European Space Agency and land data from the Office of Regional Water Studies of Mazandaran and the National Mapping Organization. Later on, the preprocessing and preparation operations on each of them will be mentioned.

2.2.1. Radar Sensor Data

The Sentinel 1 satellite was launched on April 3, 2014 by the European Space Agency. This solar satellite tracks a near-polar orbit at an altitude of 693 km. About 175 minutes is needed for the satellite to spin around the earth for a full round and it takes 12 days to re-capture from anywhere on the planet. In this study,

Sentinel 1 satellite imagery was used in the period from June 2016 to November 2016 from the Sarayan area.

Sentinel 1 SA1 Sensor

SA1 is a microwave sensor that captures C-wavelength in different modes. This sensor can, by interpolating the precision of less than one millimeter, show the displacement of the surface of the earth.

Table 1 shows the Sentinel 1 SA1 images used in this study, along time intervals and spatial basis lines.

Table 1. Sentinel 1 SA1 images used in the series with details

Table	Image state	Image mode
13/03/2015	Descending	IW_SSV
30/04/2015	Descending	IW_SSV
24/05/2015	Descending	IW_SSV
24/03/2015	Ascending	IW_SSV
17/04/2015	Ascending	IW_SSV
11/05/2015	Ascending	IW_SSV
24/04/2015	Ascending	IW_SSV
18/05/2015	Ascending	IW_SSV
11/06/2015	Ascending	IW_SSV
30/04/2015	Descending	IW_SSV
24/05/2015	Descending	IW_SSV
17/06/2015	Descending	IW_SSV

2.2.2. Rockfall Data

Based on the data for 2015 in April, May and March 2014, there have been rockfalls on Haraz Road in three different areas, used for this study.

2.3. Methods

2.3.1. Differential Radar Interferogram Technique

This is a method for combining SAR images from radar sensors mounted on a satellite or aircraft to create elevation maps, displacement and ground changes, or determine target speed. INSAR is capable of detecting displacements with a precision of millimeters, whereas DEM obtained from the laser is an accuracy altimeter 10 centimeters. In order to determine the switching of the Altimeter laser, the second DEM of the region should be reduced from the first DEM. Thus, the precision of determining displacement is 10 centimeters, which is less accurate than InSAR. Thus, the Altimeter Laser can provide more accurate DEMs and less precise mapping than InSAR. However, it is important to note that the Laser Altimeters takes up a small amount of bandwidth, and it has to overlap a large number of impressions to form a DEM comparable to DEM derived from InSAR.

2.3.2. DInSAR Method

DinSAR's differential reference vector expresses an estimate of surface changes (both in terms of surface and altitudes) by interferometry. The base for this is similar to the terrain mapping for data collection in the preparation of a map of the lattice size that was prepared 5 years ago and a map of the raster map prepared a week ago (Raster map made of pixels whose numerical values of pixels represent the altitudes). If the two maps are exactly the same, two images of an array of zero will be obtained from pixel-to-pixel difference.

If some values in the resulting image (non-zero image difference) indicate that there has been a change, the amount of change is proportional to the brightness value of the pixel in the resulting image (differential). Indeed, here we have used the map of the first (old) roster curve to remove topographic effects from the newer map. Likewise, it can be used for two DEMs from SAR images prepared before and after an important event such as a quake. The difference between the two interferometer causes the variation in the level of the quake. To produce two DEMs, four SAR images are needed in SLC format. As the first DEM derived from the interferometer should show a good approximation of the height of the earth, then it should be by a pair the radar image is produced with long open lengths. Thus, the second DEM derived from the iterphrometry should have the highest level of detail. A shorter open-coupled image should be obtained. In case of Target (such as the iceberg), the open length for the second pair of SAR images in the SLC format must be shorter. The length of the open line should be 300 m, 20 m and 5 m to generate DEM to study the motion of the earth and the applications of motion analysis (Paul, 2011).

2.3.3. Interferometer Processing

To provide interferogram with proper coupling of SLC images, relatively high coherence, accurate orbital parameters and appropriate open-ended line lengths can be processed. In a process aimed at producing a DEM, it should be used over longer spatial and shorter intervals, but in operations like this one, the purpose of which is to produce a displacement map, it should be selected at a given time interval (can be a year) data that has a low open length so that higher levels of symmetry between phases can be evaluated at 1 t and 2 t.
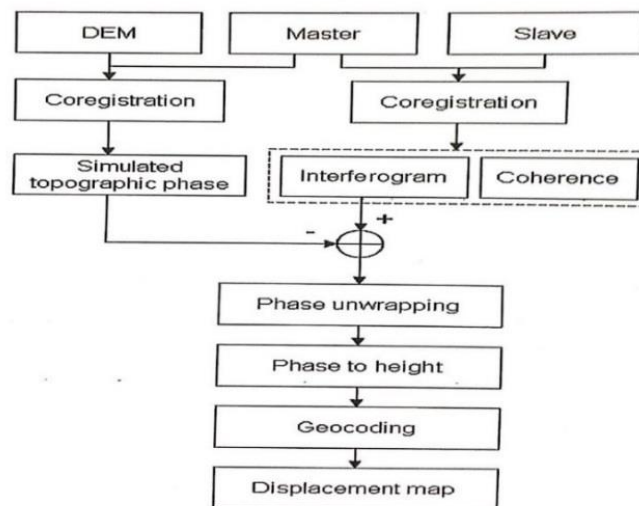

Figure 2. Processing stages in the production of interferogram and the displacement map in the DInSAR method

Mathematically speaking, an interferogram is produced by multiplying an SLC image in the complement antimatter of other SLC image. Remember that in SLC images, the open-distribution features of 1 pixel are represented by a 32-bit mixed pair.

Regarding this, the interferogram provides ground displacements in the interval between two shooting times in form of a displacement image not calibrated to a specific surface level or a definite image system. This is because the interferogram is expressed in the direction of the suffering of the mile; this is due to the fact that most SAR systems are patchy. Thus, first, the interferogram should be converted to horizontal (meaning vertical vision from above). The next step involves the wrapping of the interfrometransfer map. According to the above mentioned elements of the interferometric interactions and the relationships discussed in previous sections, interferogram was generated using sentinel1 sensor images using SARScape software for each of the studied regions.

3. Results

This part explains the details of the methods used to reach the research objectives. Using the data and method described in detail in the materials and methods, the results and outputs from the processing of Sentinel 1 images were examined. Initially, interferometry differential radar technique was used to calculate interferogram, and then using the interferogram of the map, two-axis was calculated and the maps were moved in each step. The research steps are described in Figure 2. Interfere-meters were performed in each of the upper and lower passes of the images for individual interferometry, and were discussed in different regions, the interferogram logs are shown below. The details of the produced interferogram are shown in Table 2:

Table 2. Baseline details

Pilot number	Image type	Image mode	Date	Temporal Base line(day)	Spatial Base line (meter)
Pilot 1 and 2	Ascending	IW_SSV	13/03/2015	48	145.11
		IW_SSV	30/04/2015		
		IW_SSV	30/04/2015	24	89.35
		IW_SSV	24/05/2015		
	Descending	IW_SSV	24/03/2015	24	12.60
		IW_SSV	17/04/2015		
		IW_SSV	17/04/2015	24	43.5
		IW_SSV	05/11/2015		
Pilot 3	Ascending	IW_SSV	24/04/2015	24	74.25
		IW_SSV	18/05/2015		
		IW_SSV	18/05/2015	24	73.63
		IW_SSV	11/06/2015		
	Descending	IW_SSV	30/04/2015	24	84.25
		IW_SSV	24/05/2015		
		IW_SSV	24/05/2015	24	76.32
		IW_SSV	17/06/2015		

3.1. Interferogram Production

The interferometer contains the phase difference between two images. The altitude is determined at each point of the region at the time interval between the two images by the phase difference check. The interlacing is made by the mixed blend of the original image in conjunction with the dependent image.

Removal of the effect of photographed topography due to interferometry using the digital earth model (DEM), the effect of the topographic phase can be eliminated from the interferometer, the more accurate the DEM and the orbital information of DORIS, the better the removal process is done. The results of this step

are to remove power from phase and generate power file, dpf, int, sint, dint, and shp srdem power.tif. It should be noted that the difference between int and dint is that there is topography in the int file, but there is no topography in the dint. There may be three attributes in the int file called Ramp, Jump, Bamp. The phase changes and looks like a dome. If Bamp is available, the fringe is formed in the form of concentric circles with the same diameter.

3.2. Applying Filter

The resulting differential interferometer contains some noises. The element producing these noises can be different, with two main factors affecting their creation. The first factor is the time difference between the two main and dependent images. Sometimes, changes in the area that occur between the time intervals of the two images are all about the noise that can be attributed to the construction of residential areas or agricultural activities in the region. The second major factor is the effect of the creation of noise. The point of reference is that the noise level in the images is directly related to the spatial basis, the higher the number, the more noise encounter in the interferometer.

Filtering has been used to remove and reduce noise. Due to the high efficiency of Goldstein's filter, it was used in the study. The result of applying the Goldstein filter is the production of interferometric filter, with more margins in comparison with non-filtered interferometric filter with significantly reduced noise level. The special feature of this filter is acting selectively, and the filtering operation is performed locally, the type of performance of the Goldstein filter is affected by the interferogram correlation, in some cases the degree of correlation is low, the amount of pixels is more affected. And in cases where the correlation is high, it affects the limited number of pixels which is made simultaneously with the filtering of the image of symmetry.
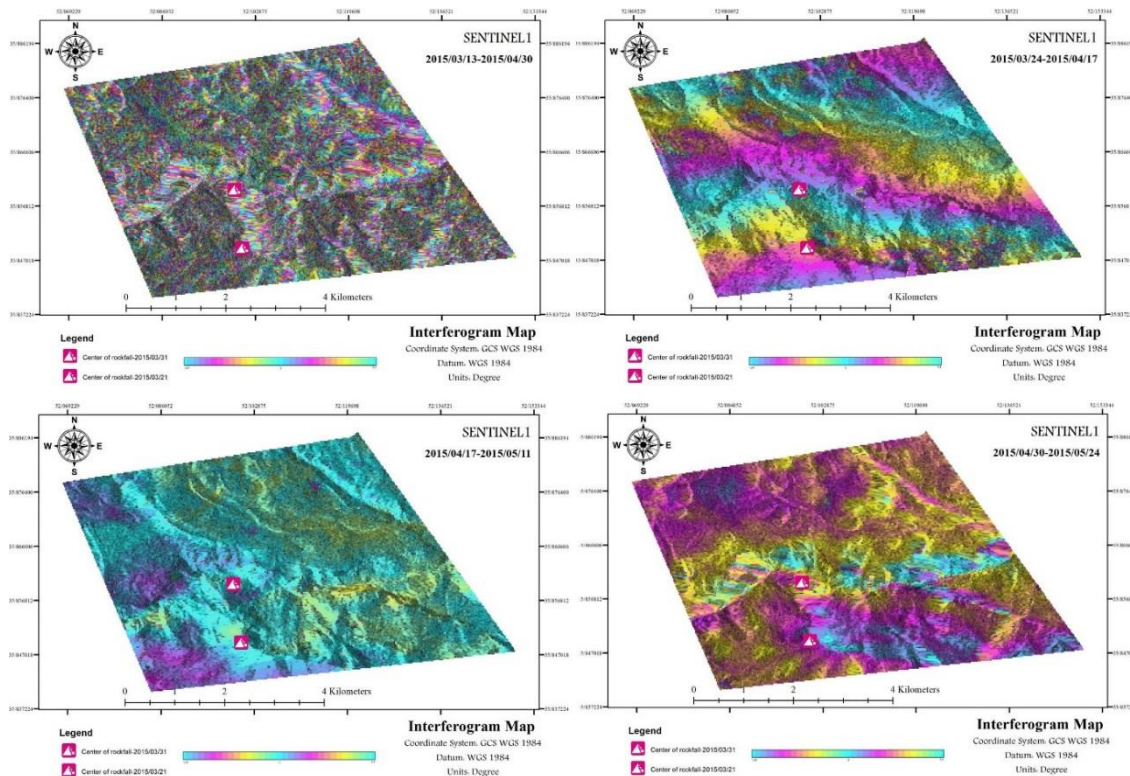

Figure 3. Interferogram Map

In the days March 20, 2015 and April 3, 2015, two elevations occurred at a distance of 2 km in the area of Haraz road, as shown in Figures 3 and 4, of the interferometer for the low pass state and in Figures 5 and 6, it is related to the high-pass state.
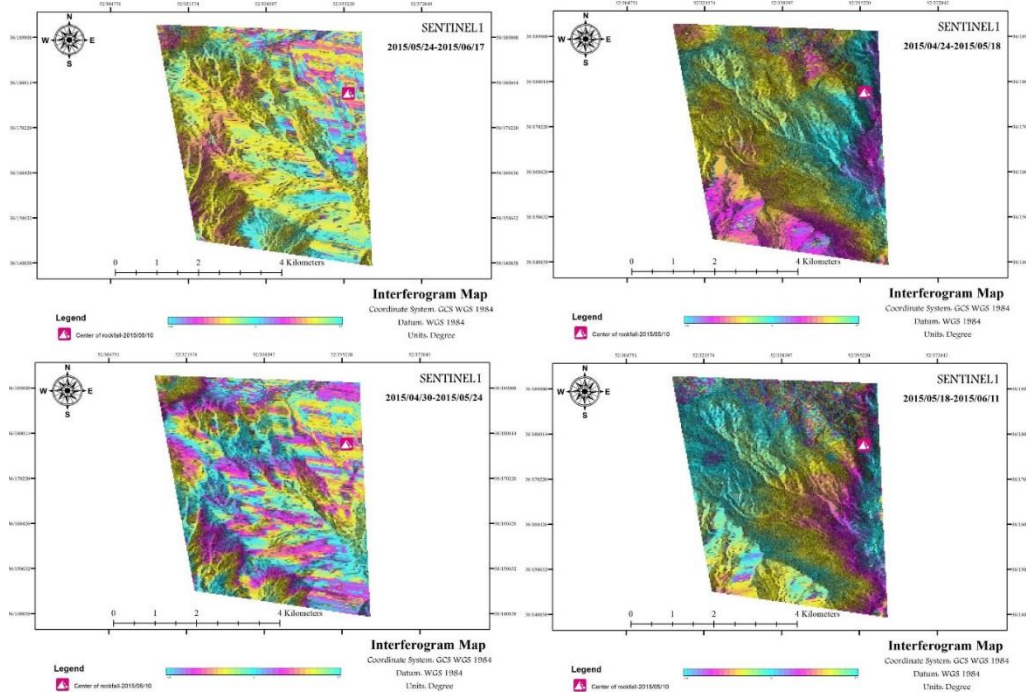

Figure 4. Interferogram map

One of the outputs of the interferometry radar technique is the coherence of the images used in the interferometer, as seen in Figures 5 and 6. The symmetry image is affected by the correlation between the coupled powers of the image. It has to be noted that the coherency image expresses the correlation between the original and dependent image signals. The degree of coherence is between 0 and 1, the pair of images whose zero-degree symmetry is zero, there is no signal-dependent relationship between them, and when the degree of symmetry is one, the signal dependency between the two images is 100%. The higher the degree of symmetry between the coupled images, the better the couple of images for the differential interferometry are, and an increase in the quality of the interlaced is witnessed.

$$\gamma = \frac{\left| \sum S_1(X).S_2(X) \right|}{\sqrt{\sum |S_1(X)|^2 . \sum |S_2(X)|^2}} \tag{1}$$

S_1 is the mixed value of the original SAR image, and S_2 is the mixed quantity of the SAR image, and γ is the degree of coherence between the two images. The degree of coherence expresses the accuracy of the results obtained, so that in images whose magnitude of coherence is close to 5.0 or higher, they are suitable images for interlacing, but in cases with values less than this, one can use them to construct interlacing (Anderson et al., 2008).
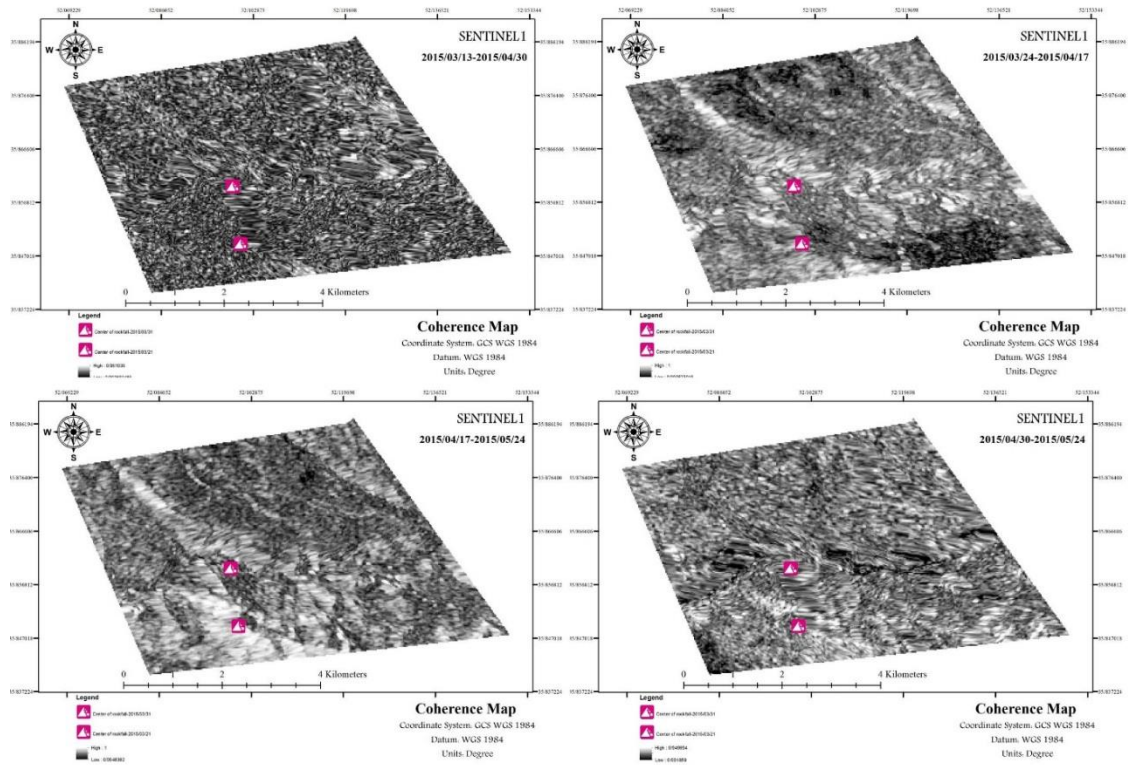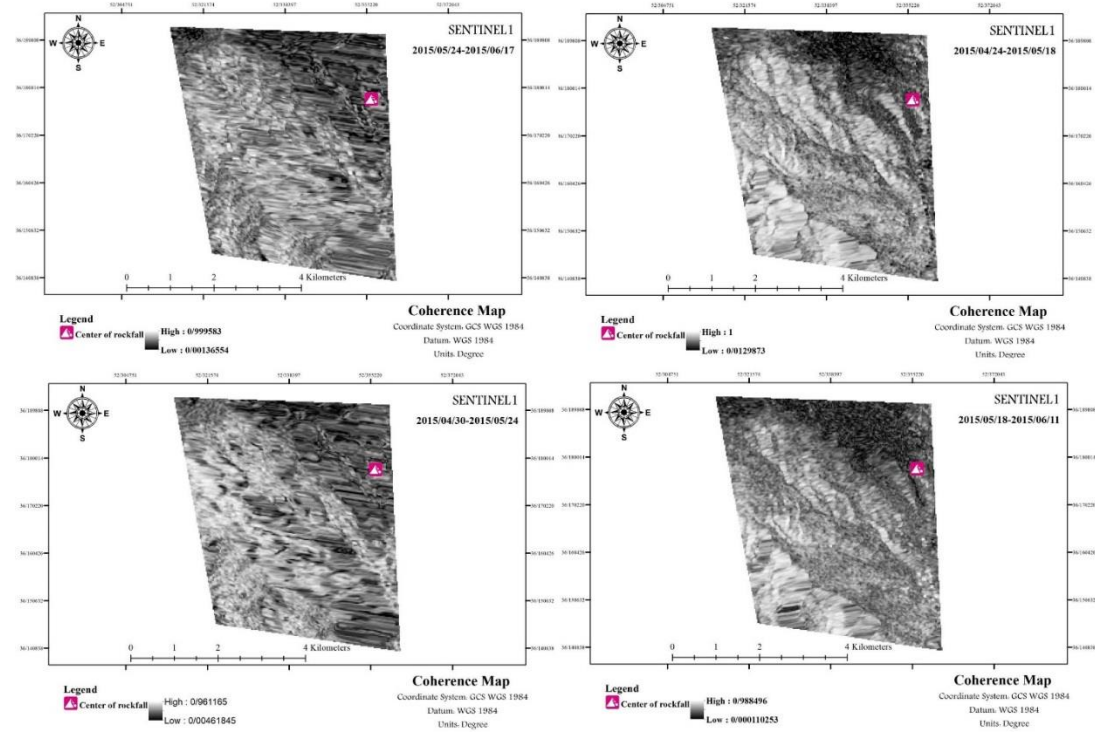
Figure 5. Coherence map

Figure 6. Coherence map

3.3. Sentinel 1 Sensor Displacement Values

After interferometry method on Sentinel 1 images and creating interlacing and after final processing in SARSCAPE software, they were converted to vertical displacement values in meters.

3.4. Absolute Phase Transformation to Displacement

The changes in the phase show the variations in height are half as wavelength, as the rockfall wavelength of the Sentinel 1 sensor is 5.6 centimeters. Changes of $\pi 2$ equal lead to height change of 8.2 cm. With the removal of the orbital phase and the phase of the vibration of the platform, the absolute phase of the result can easily be converted to altitudinal displacements. In phase-to-altitude conversion, for each pixel, the value is equal to the magnitude of the elevation of that point in terms of metric. In subsidence maps, the negative values show the downward movement (subsidence). The entire process is used to the coupled images of Sentinel1 and results in the creation of descending maps at the time of taking pictures.
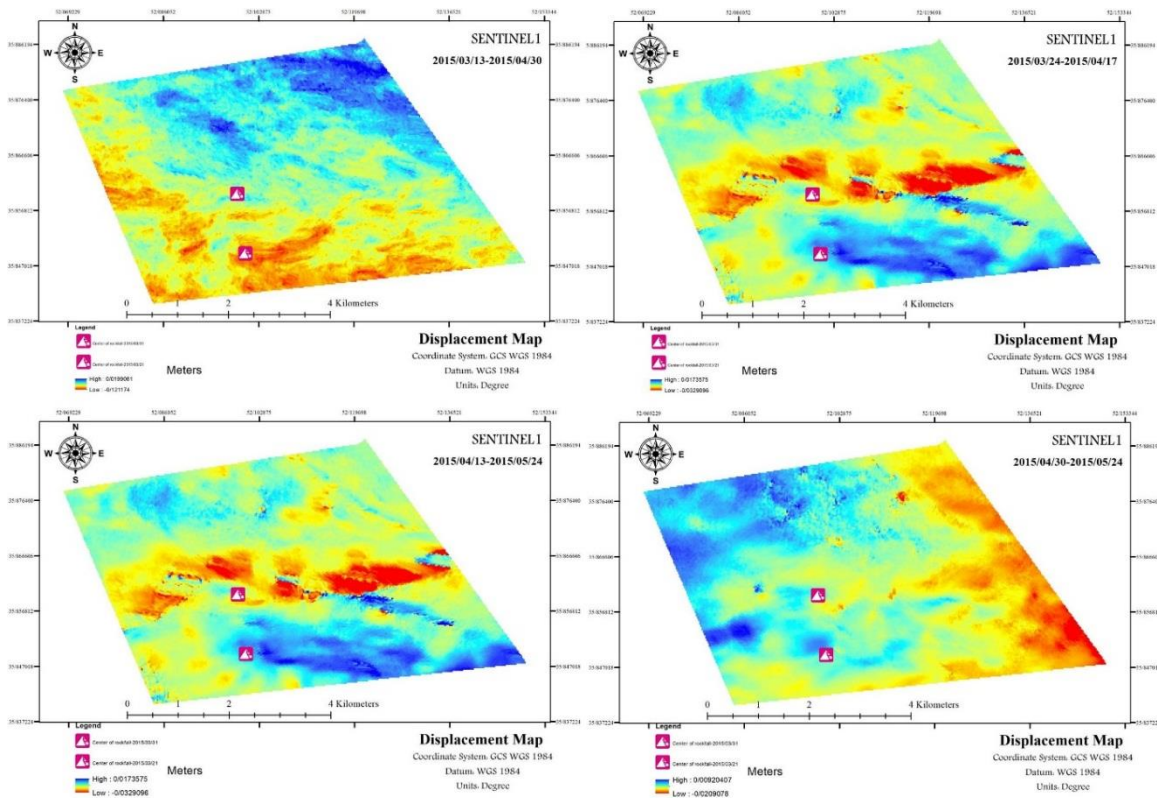

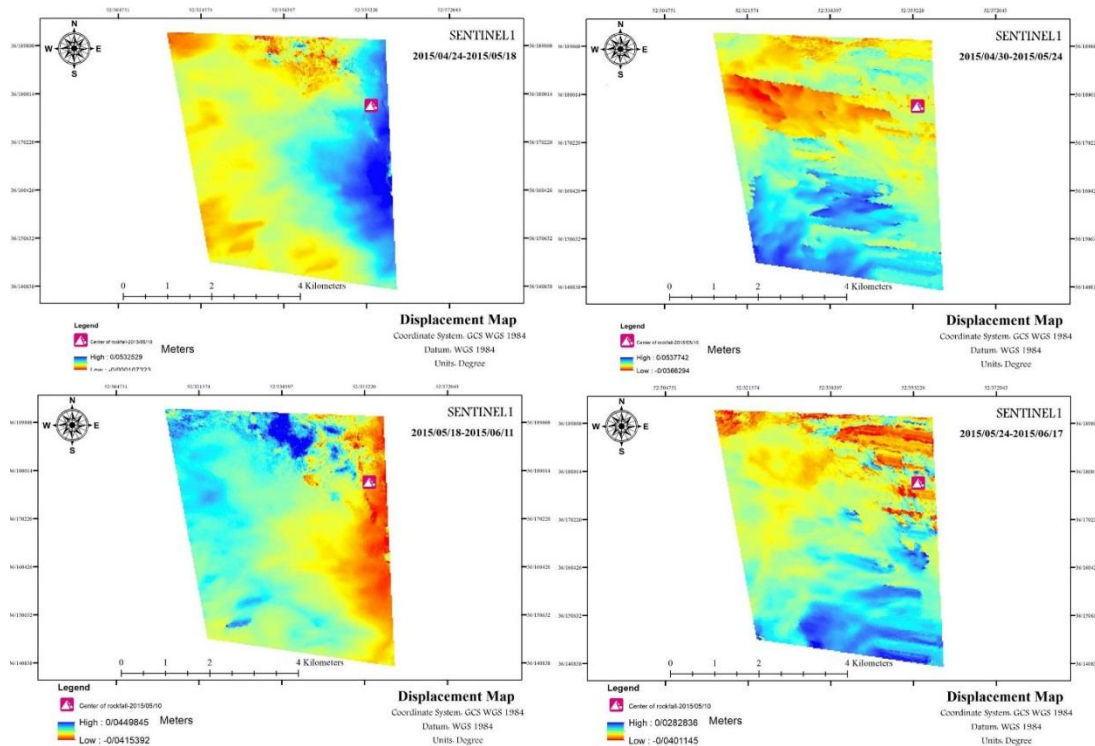**Figure 7**. Vertical map of the Earth's surface

Figure 8. Vertical map of ground level

4. Discussion and Conclusion

Although rockfalls are physically affected by the slopes, they are subject to uncertainty and probability issues that must be calculated. A definitive polar modeling has problems with describing and evaluating complex natural processes, such as rockfall. Using interferometric radar method in this study, due to the adverse effects of massive movements and rock falls on the socioeconomic and natural systems, the need to understand areas sensitive to rockfall to avoid the risk and prevent the occurrence of financial losses, environmental, the initiation of protective and preventive measures (Krum, 2001). The fall of the rocks is the result of the separation of large and small parts of the rocky slopes. The small and large pieces of massive rock phenomena simultaneously fall into large masses, called "fall" (Mahmoudi, 2011), as other phenomena of geomorphology, the result of several factors and also the result of the interaction of different factors on each other. The material of the bed of the massive movements, the slope of the valley domain, the land use, the fault, the lines of communication and drainage, and so on are among the factors influencing the occurrence of these phenomena. Tomas, Vinowich and Anderson (1995) stated that massive motions in rock slopes, sandstone formations and limestone were introduced with more rockfalls. Compared to the landslide phenomenon, few studies have been constructed in Iran regarding fall. In the study, Gholami (2004) examined the risk of rockfall using GIS and remote sensing along Haraz road from Vana to Plor. In this study, four factors of lithology, slope, elevation, and road distance were considered for decision makers and reaction to falling rocks. Bayati Khatibi (2007) has examined the zoning of high-risk and mountain slopes of the communicative network of villages located in Garnukuchai basin, where 10 factors were considered for zoning official susceptible areas. After weighing all the factors, the sensitivity of different parts of the area with five classes of sensitivity were obtained. Shirzadi, Mousavi and Kavian (2010) conducted a study entitled "The GIS of the Regional Model of Rockfall through Mountain Roads" with the help of the overlap index in Salavat turn in Abad of Kurdistan, using the rockfall density and allocating expert weights to the factors, showed a map of the risk of rockfalls in the study area. In this study, the accuracy of the zoning map for hazard locating of rockfall was "70%". Madal Dost and Ooladzadeh (2010) used their research in 3D

modeling the area of Imamzadeh Ali Jadat Haraz GIS as base for determining the path of rockfall in the environment. In this study, the descriptive statistics of the spill points, including the difference in length (m), the minimum length of the path, the maximum length of the path, the average length of the path and the distance to the point were determined and the distribution of the risk of rockfalls, rock placement and rock hazard zonation were achieved. Based on the discussions, it is shown that the use of radar interferometry with the help of INSAR algorithm in this study has a good capacity for determining the rate of land surface movement in the short and long terms. The wavelength C was introduced at the range of the study. Processed interferograms only have a short time line to reduce the lack of time correlation and their spatial bases are taller than the usual one, since the goal of the processing is a large number of interferograms in such a way that the intergroup chips are not discrete, but interferograms with the length of the base line. The high point is under the influence of topographic error. In the study, three different pilots of rockfall in two high and low passes were prepared before and after the rockfall of the interferometer. The findings showed that during interferogram extractive rockfall, spectacles have significant changes in the central part of rockfall. Moreover, the coherence maps created during these times have been modified in the direction of fall move. The above cases leading to the displacement maps at the time of the rockfall showed significant changes explained in details in the images. There was no accurate ground information on the volume of rockfall that the case made it impossible to compare satellite and ground data. Rockfalls are a major hazard in rock cuts for highways and railways in mountainous terrain. While rockfalls do not pose the same level of economic risk as large scale failures which can and do close major transportation routes for days at a time, the number of people killed by rockfalls tends to be of the same order as people killed by all other forms of rock slope instability.

Reference

Afzali, A., Sharifi Kia, M., & Shayan S. (2013). Assessing the vulnerability of infrastructure and settlements to the phenomenon of subsidence in the plain of Damghan. *Two letters of application form of geomorphology*, (1), 70-85.

Amighpey, M., Arabi, S., Talebi, A., & Djamour, (2006). Elevation changes of the precise leveling tracks in the Iran leveling network, *Scientific report published in National Cartographic Center (NCC) of Tehran, Iran.*

Motagh, M., Walter, T. R., Sharifi, M. A., Fielding, E., Schenk, A., Anderssohn, J., & Zschau, J. (2008). Land subsidence in Iran caused by widespread water reservoir overexploitation. *Geophysical Research Letters, 35*(16).

Chatterjee, R. S., Fruneau, B., Rudant, J. P., Roy, P. S., Frison, P. L., Lakhera, R. C., ... & Saha, R. (2006). Subsidence of Kolkata (Calcutta) City, India during the 1990s as observed from space by Differential Synthetic Aperture Radar Interferometry (D-InSAR) technique. *Remote Sensing of Environment, 102*(1-2), 176–185.

Raucoules, D., Colesanti, C., & Carnec, C. (2007). Use of SAR interferometry for detecting and assessing ground subsidence. *Comptes Rendus Geoscience, 339*(5), 289-302.

Esmaili, M., & Motagh, M. (2009). Remote sensing measurements of land subsidence in Kerman Valley, Iran, 2003-2009. In *AGU Fall Meeting Abstracts*.

Galloway, D. L., Hudnut, K. W., Ingebritsen, S. E., Phillips, S. P., Peltzer, G., Rogez, F. & Rosen, P. A. (1998). Detection of aquifer system compaction and land subsidence using interferometric synthetic aperture radar, Antelope Valley, Mojave Desert, California. *Water Resources Research, 34*(10), 2573-2585.

Haghighat Mehr, P., Voldan Zagh, M. J., Tajik, R., Jabari, S., Sahebi, M. R., Islami, R., Ganjian, M., & Dehghani, M. (2012). The analysis of the time series of Hashtgerd subsidence using radar interferometry and global positioning system, *Journal of Geosciences*, (85).

Hajizadeh A.H., Nasim Mahlah, M. A., Farzaneh S., Rastegar A. M., Seyyed Razaei, H. (2013). Principles of Microwave Remote Sensing (Radar Interferogram) with Emphasis on Earth Sciences. *Satellite Publishing, Tehran.*

Hoffmann, J., Zebker, H. A., Galloway, D. L., & Amelung, F. (2001). Seasonal subsidence and rebound in Las Vegas Valley, Nevada, observed by synthetic aperture radar interferometry. *Water Resources Research, 37*(6), 1551-1566.

Poland, J. F., Ireland, R. L., Lofgren, B. E., & Pugh, R. G. (1975). Land subsidence in the San Joaquin Valley, California, as of 1972.

Li, C., Tang, X., & Ma, T. (2006). Land subsidence caused by groundwater exploitation in the Hangzhou-Jiaxing-Huzhou Plain, China. *Hydrogeology Journal, 14*(8), 1652-1665.

Motagh, M., Djamour, Y., Walter, T. R., Wetzel, H. U., Zschau, J., & Arabi, S. (2007). Land subsidence in Mashhad Valley, northeast Iran: results from InSAR, levelling and GPS. *Geophysical Journal International, 168*(2), 518-526.

Motagh, M., Walter, T. R., Sharifi, M. A., Fielding, E., Schenk, A., Anderssohn, J., & Zschau, J. (2008). Land subsidence in Iran caused by widespread water reservoir overexploitation. *Geophysical Research Letters, 35*(16).

Motagh, M., Djamour, Y., Walter, T. R., Wetzel, H. U., Zschau, J., & Arabi, S. (2007). Land subsidence in Mashhad Valley, northeast Iran: results from InSAR, levelling and GPS. *Geophysical Journal International, 168*(2), 518-526.

Motagh, M., Djamour, Y., Walter, T., Moosavi, Z., Arabi, S., & Zschau, J. (2006). Mapping the Spatial and Temporal Pattern of Landsubsidence in the City of Toos, Northeast Iran, Using Theintegration of InSAR, Continuous GPS and Precise leveling. *Geophysical Research Abstracts,. 8*, 07881.

Pacheco, J., Arzate, J., Rojas, E., Arroyo, M., Yutsis, V., & Ochoa, G. (2006). Delimitation of ground failure zones due to land subsidence using gravity data and finite element modeling in the Querétaro valley, México. *Engineering Geology, 84*(3-4), 143-160.

Mather, P. M., & Koch, M. (2011). Computer processing of remotely-sensed images: an introduction. John Wiley & Sons.

Pope, J. P., & Burbey, T. J. (2004). Multiple-aquifer characterization from single borehole extensometer records. *Groundwater, 42*(1), 45-58.

Richards, J. A. (2009). Remote sensing with imaging radar (Vol. 1). *Berlin: Springer*.

Hunt, R. E. (2007). Geologic hazards: a field guide for geotechnical engineers. *CRC Press*.

Schoeneberger, P.J. & Wysocki, D.A., (1997). Geological of geology , American Geological Institute,Alexandria, National Soil Survey Center, 4th Ed, p 769. ISBN 0-922152-34-9

Sharifi Kia, M. (1991). Determination of the extent and amplitude of ground submarine by radar interferometry (D-InSAR) method in Navek-Bahreman plain. *Journal of Planning and Space Design, 16*(3), 55-77.

Sharifikia, M. (2006). DEN Generation & Morphology Feature Extraction – Using InSAR, PGD Project Submitted to CSSTEAP.

Sharifikia, M. (2009). D-InSAR Data Processing and Analysis for Mapping Land Subsidence Phen omenon In Rafsanjan Area, Iran M.Tech Thesis, Submitted to Andra University-India.

Sharifikia, M., DEM Generation & Morphology Feature Extraction -Using InSAR, PGD Project Submitted to CSSTEAP, 2006.

Shemshaki, A., Blourchi, M. J., & Ansari, F. (2005). Preliminary report on Tehran subsidence. *Engineering Geology Scientific report to the Geological Survey of Iran, Tehran*.

Tony, W. G., Martin, C., & Fred, G. B. (2005). Sinkhole and Subsidence. *Springer and Praxis Publishing Ltd. UK -Germany.*

Zebker, H. A., Rosen, P. A., Goldstein, R. M., Gabriel, A., & Werner, C. L. (1994). On the derivation of coseismic displacement fields using differential radar interferometry: The Landers earthquake. *Journal of Geophysical Research: Solid Earth, 99*(B10), 19617-19634.

Quantifying Geotechnical Changes in the Rafsanjan Plain in Time Series and Finding Out Their Causes Using Radar Remote Sensing Techniques

Jalal Hassanshahi[a*], Ali Sarkargar Ardakani[b]

[a]Ms in GIS and Rs, Natural resources and watershed management organization, Kerman, Iran
[b]Associate Professor, Department of RS, Imam Hossein University, Tehran, Iran

Abstract

Subsidence is the earth's surface movement towards down relative to a datum such as sea level. The main reason of subsidence in Iran is groundwater overuse which if not managed correctly, it causes irreparable damages. Therefore, the first step in solving this problem is identification of subsidence areas and estimating the rate which will have a significant role in controlling this phenomenon. One of the most suitable methods of identification of subsidence is using Interferometric Synthetic Aperture Radar (InSAR)technique. This method is superior to other detection T in terms of cost, precision, extent of the study area and time and it can provide an accurate estimate of the area. In this research, zone of the Rafsanjan plain has been investigated between 2006 and 2010. In order to calculate subsidence rate, SAR data related to the ASAR sensor in C-band and ALOS PALSAR in L-band were used. Generalized linear models in C-band and L-band with values of 0.91 and 0.89 and RMSE coefficient of 0.37 and 0.61 represented a strong linear relationship. Also the relationship between subsidence and the changes inpiezometric levels (groundwater extraction) in the study area showed that for each 4.7 centimeters groundwater level decrease, there has been 1 centimeter subsidence.

---

* Corresponding author. Tel: +98-9132915062.
Email address: hassanshahijalal@gmail.com.

1. Introduction

According to the United States institute of geology, land subsidence is sinking or downward settling of ground's surface which can be with a small horizontal displacement vector (USGS, 2011). Land subsidence is sudden or gradual sinking of the ground's surface due to changes in shape and displacement of particles (Rahnama et al., 2006) caused by natural factors (volcanoes, sinkholes in soluble rocks, wrinkles) and human factors (mining, construction, extraction of groundwater, oil and gas) (Roy et al., 2005). Although this phenomenon occurs in many sequences and frequencies, usually its understanding and measuring are not possible. For this reason, in most areas, this event is just known when it affects surface morphology as well as facilities and equipment. Sometimes this phenomenon has a wide range because of exacerbation and stimulation of its trigger factors such as increased pressure in exploitation or operation beyond the capacity of groundwater resources of the plains. In addition to creating many morphological outcrops in earth's surface, subsidence becomes a threat to human life. Creating sinkholes, foundation movement, tilting tall buildings etc. are the most common damages caused by the intensified subsidence. Sometimes these risky situations can be catastrophic because of special conditions of locations and proximity and having a hazardous infrastructure as a result of other natural hazards like earthquake. In other words subsidence and natural hazards in a place together can turn small disasters to great catastrophes (Sharifikia, 2012). There has been land subsidence in Iran since many years ago and some studies have been conducted in some areas. Among these areas, Rafsanjan was one of the first areas in which this phenomenon was identified (Geology institute, 1998). The closest research in terms of geographic location to the studied area is a research by Sharifikia titled "Determination of the rate and extent of land subsidence in the Noogh-Bahreman plain using radar data in C- and L- band between 2005 and 2010". In this research, subsidence has been calculated with an average annual of about 30 centimeters in an area of 281 square kilometers in the middle part of the plain. Also by comparing the rate of subsidence with changes in level of exploited water in peizometric wells, it was concluded that in this plain every 3.2 centimeters ground water lowering can cause a subsidence of 1 centimeter. Haghighatmehr et al. (2013) in a survey named "Time series analysis of Hashtgerd subsidence using radar interferometry and global positioning system", used SAR interferometry (InSAR) and global position system (GPS) in order to study the subsidence in Hashtgerd plain that has been affected by subsidence due to excessive groundwater extraction. Additionally, in order to analyze the deformation time series, they used small baseline subset (SBAS) algorithm and they performed time series analysis using 6 interfrograms calculated from 4 ENVISAT ASAR data spanning 4 months in 2008. Time series results showed the area is subsiding continuously. moreover mean LOS deformation velocity map obtained from time series analysis revealed a considerable subsidence rate of 48 mm per month. To assess the time series analysis results, a dense GPS network consisting of 18 measuring stations was established. The GPS stations were collecting the data simultaneously with radar data acquisitions. Then horizontal and vertical components of the subsidence were extracted from GPS measurements. The comparison of InSAR and GPS time series showed the high compatibility of the results demonstrating the high performance of InSAR technique. Heshmati and Almodaresi (2014) in another paper named "Modeling subsidence of the Neishabour plain using time series and DINSAR technique" studied Neishabour plain between 2003 and 2010. In order to calculate subsidence rate, SAR data related to ASAR sensor prepared in C-band was used. The amount of displacement using GPS data in Neishbour statin was compared with the amount of displacement using ASAR data. They did not have a significant difference. Also the relation between subsidence and changes in peizometric surface (groundwater extraction) showed for every 3 centimeters lowering of peizometric surface there has been 0.816 centimeter subsidence.

The Research objectives:

Increasing population and fulfilling the needs of today's human societies have led to more attention to exploitation of water resources especially in warm and dry areas such as Iran. Due to the climatic conditions of Iran, it is necessary that development plans and exploitation of water resources for various uses (drinking, industrial and agriculture) in different regions of the country to be identified to achieve optimal and sustainable exploitation of water resources. Subsidence affects a vast area but it is not easy to recognize and generally in cases where the facility and buildings are damaged, it will be identifiable. Subsidence event is preventable and at the time of occurrence, we are able to reduce its trend or even stop it. In this research, it

is tried to identify and manage the areas involved in subsidence before the subsidence destroys the main infrastructures and causes casualties and financial losses. Finding a significant relationship between groundwater reduction and subsidence rate is the next step.

In this research, a significant relationship between groundwater level changes and surface deformation has been found using Interferometric synthetic aperture radar. The main question of this research is:

1- Can the relationship between ground water reduction and subsidence rate using Interferometric synthetic aperture radar and C- and L- band images be modeled?

To answer this question, two hypotheses are proposed:

1- Satellite radar images in the range of microwave with wavelengths of C- and L- band are appropriate for calculating of subsidence rate.

2- There is a significant linear relationship between groundwater reduction and subsidence rate.

Since the Rafsanjan plain is one of the most critical plains in the country in terms of overuse of groundwater, the phenomenon of subsidence is quite tangible, but no research has been done in the central part of the Rafsanjan plain using this method and C- and L-band data so far. Also the proof of the relationship between the subsidence in the Rafsanjan plain and groundwater extraction is one of the aspects of innovation of this research.

2. Materials and Methods

2.1. Used data

Used data in this paper is divided into two categories, terrestrial and satellite data. Terrestrial data was obtained from the Kerman Regional Water Studies Office and satellite data was prepared from the European Space Agency.

Table 1. Details of the used ASAR sensor images in the Rafsanjan plain

Space headway (meter)	Time headway (day)	Date	Image mode
188/958	419	2006	ASA_IMS
		2008	ASA_IMS
50/933	144	2008	ASA_IMS
		2010	ASA_IMS

Table 2. Details of the used ALOS PALSAR sensor images in the Rafsanjan plain

Space headway (meter)	Time headway (day)	Date	Image mode
375.36	695	2007	JAXA-FBS
		2009	JAXA-FBS
698.74	1050	2007	JAXA-FBS
		2010	JAXA-FBS

According to statistical obtained from Kerman Regional Water Studies Office between 1384 and 1389 in the area of study, there has been 31 piezometric wells. In this statistic, the number which is related to the piezometric surface shows water surface elevation from earth's surface and its unit is in meters.

2.2. Area of the study

Rafsanjan city is located in the northwest of Kerman province. Its geographical coordinates are $54° 56′$ to $43° 56′$ eastern longitude of Greenwich meridian and $29° 55′$ to $31° 17 ′$northern latitude. Its area is about 7678 square kilometers and it is accounted for 4.19 percent of the province's total area. It is limited to Bafgh in Yazd province from the north, to Sirjan and Bardsir from the south, to Anar and Shahr-e- Babak from the

west and to Zarand from the northeast. The city center is located at 1469 meters above sea level. The lowest point is in the output of the Rafsanjan plain, in Noogh region with 1260 meters and the maximum height of the city is in Raviz Mountains and Sarcheshmeh, 2900 meters above sea level. Rafsanjan has different names which are related to its underground resources. For example, Rafsankan or Rafsank consists of two words, Rafsank means copper and Kan means mine and Rafsanjan is Arabic. Sarcheshme copper mine known Chashmefiroozehei (turquois eye) is the largest open pit mine in the world. Also Rafsanjan is the largest pistachio producer in the world and because of its high quality pistachios, it is a well-known city in the world. In this city there are 80000 hectares of pistachio gardens which are irrigated by 1300 agricultural wells. Also the world's largest adobe house is located in Rafsanjan, one of the most beautiful ancient monuments with 110 rooms. This historical city has the richest copper mines and Sarcheshmeh copper complex is the third largest copper processing plant in the world. The area of study in this paper is central part of the Rafsanjan plain with an area of 2680 square kilometers.
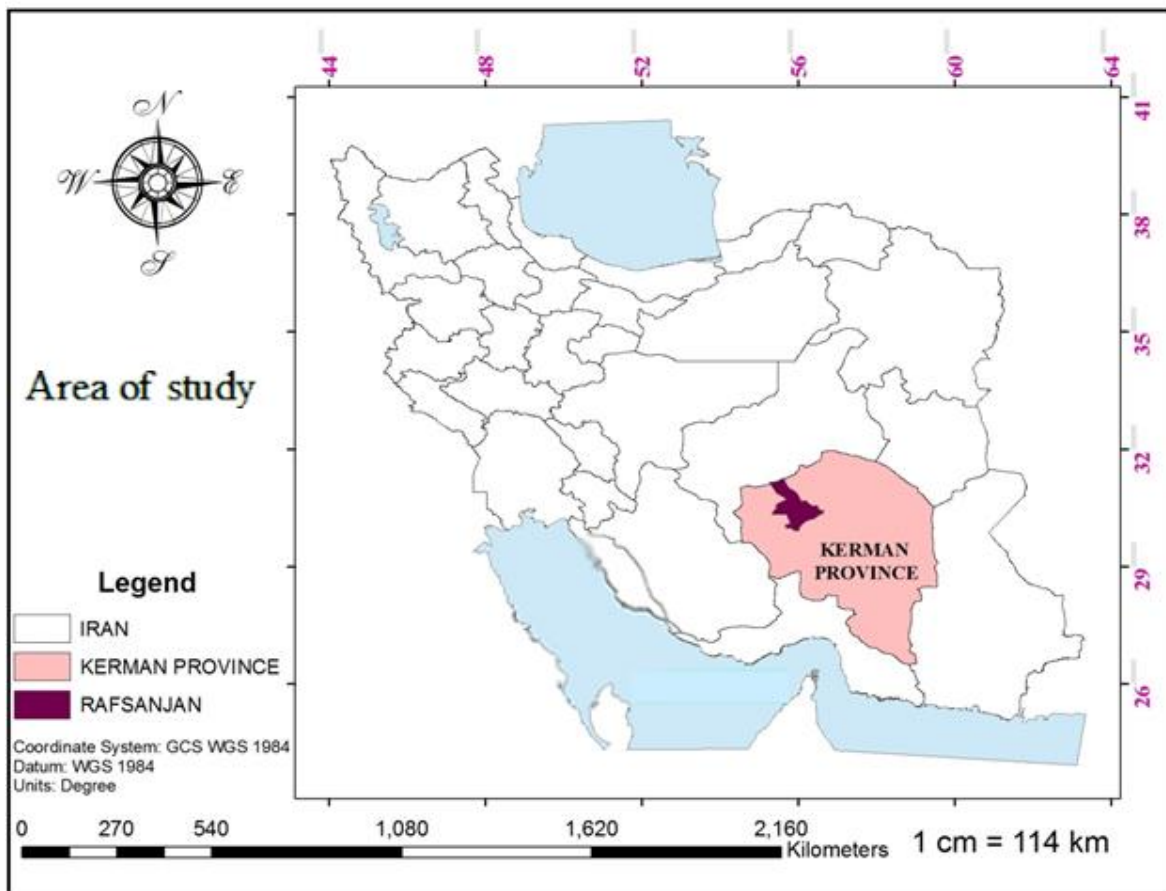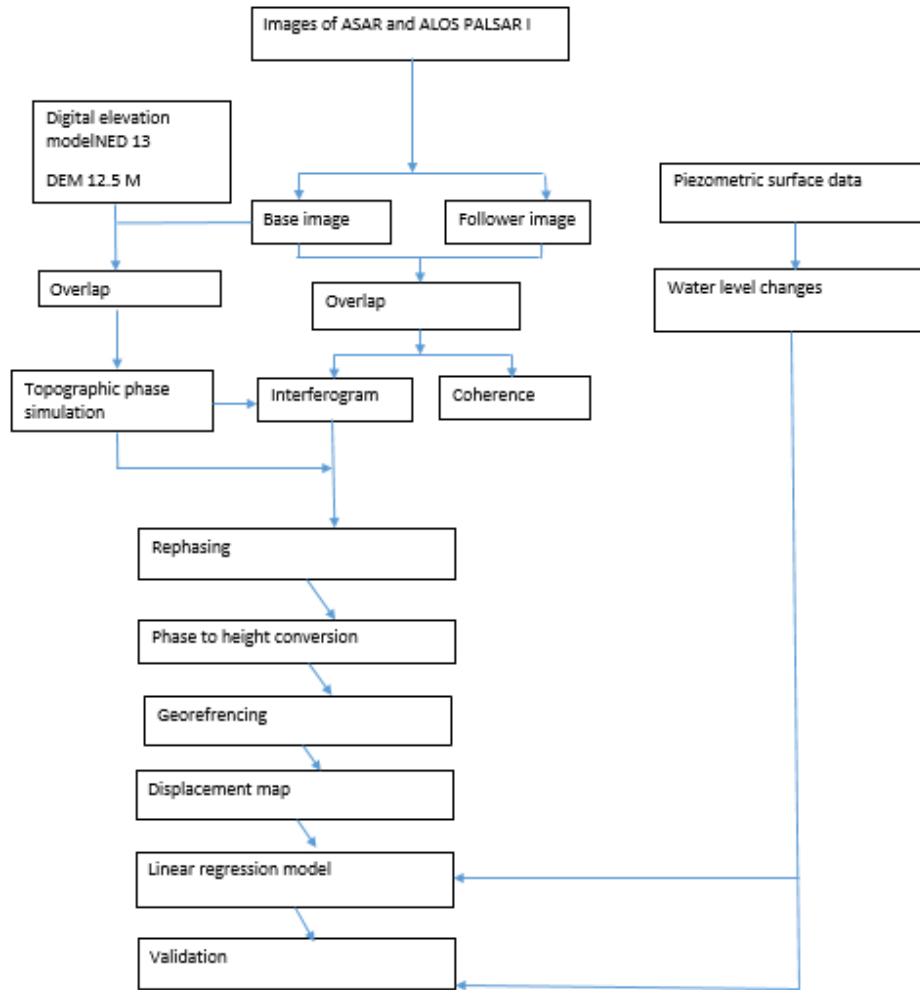

Figure 1. Area of the study

Figure 2. Work flowchart

2.3. Differential Synthetic Aperture Radar Interferometry technique

Differential interferometry (DinSAR) gives an estimate of surface variation (both flat and altitude) by interferometry. The basis of this is similar to ground surveying for data collection in preparing a contour map based on raster which was prepared 5 years ago and a contour map based on raster that was made a week ago (a raster map is made up of pixels, each containing a value that indicates elevation). If two maps are exactly the same, an array of zero will be obtained from minus pixels of two images. If some values in obtained image (difference of two images) are not zero, it means there has been a change. The rate of changes is proportional to the pixel brightness value in the obtained image. In fact, here the first (previous) contour map based on raster has been used to remove topographic effects of the new map. The same can be done for two DEMs obtained from SAR images which are prepared before and after an important event such as an earthquake. The difference between two images obtained from interferometry represents changes in the surface caused by the earthquake. Four SAR images in SLC format are needed to create two DEMs. Since the first DEM obtained from inter ferometry should indicate a good approximation of ground level altitude; it should be created by a pair of radar images with long wavelength. As the second DEM obtained from interferometry should show most of the details of the surface, it should be created by a radar image with short wavelength. In places where a target (for example: an iceberg) is moving, wavelength should be short for the second pair of SAR images with SLC format. The wavelength should be 300 meters, 20 meters and 5 meters respectively for production DEM, study of land displacement and movement analysis (Paul, 2011).

In order to succeed in DinSAR method, low correlation between two interferogram should be as small as possible. In water areas and forest areas, low correlation occurs quickly so that separating of effects of deformation of the earth, land subsidence and ice mass movement from the effects of low correlation is impossible. Long wavelengths have less low correlation than short wavelengths, so that they penetrate more in canopy of plants and they are less influenced by the geometry of plant canopies (Paul, 2011).

2.4. Linear regression method

Statistical models such as regression run better for small sample sizes when theory or experiment shows a systematic relationship between dependent and independent variables. Linear regression has been used by many researchers to estimate various parameters. In this paper, linear regression method has been used in MATLAB software environment. Linear regression may be simple or multiple. Simple linear regression consists of a dependent variable and an independent variable. A regression equation is an equation which shows the relationship between dependent and independent variables and the value of the dependent variable can be estimated using the independent variable.

3. Results and Discussion

In this part results and output from ASAR and ALOS PALSARI images processing have been used. At first, displacement rate was obtained using differential synthetic aperture radar interferometry technique and then its linear equation was calculated using correlation between displacement rate produced by two sensors and terrestrial data of piezometric levels. At each step, produced maps were validated.

3.1. Values of ASAR sensor displacement

Interferograms were generated using DinSAR method. Then they were converted to vertical displacement values in meters after final processing in SARCAPE software. Displacement maps obtained from ASAR sensor images in C-band have been showed in figures 3 and 4.
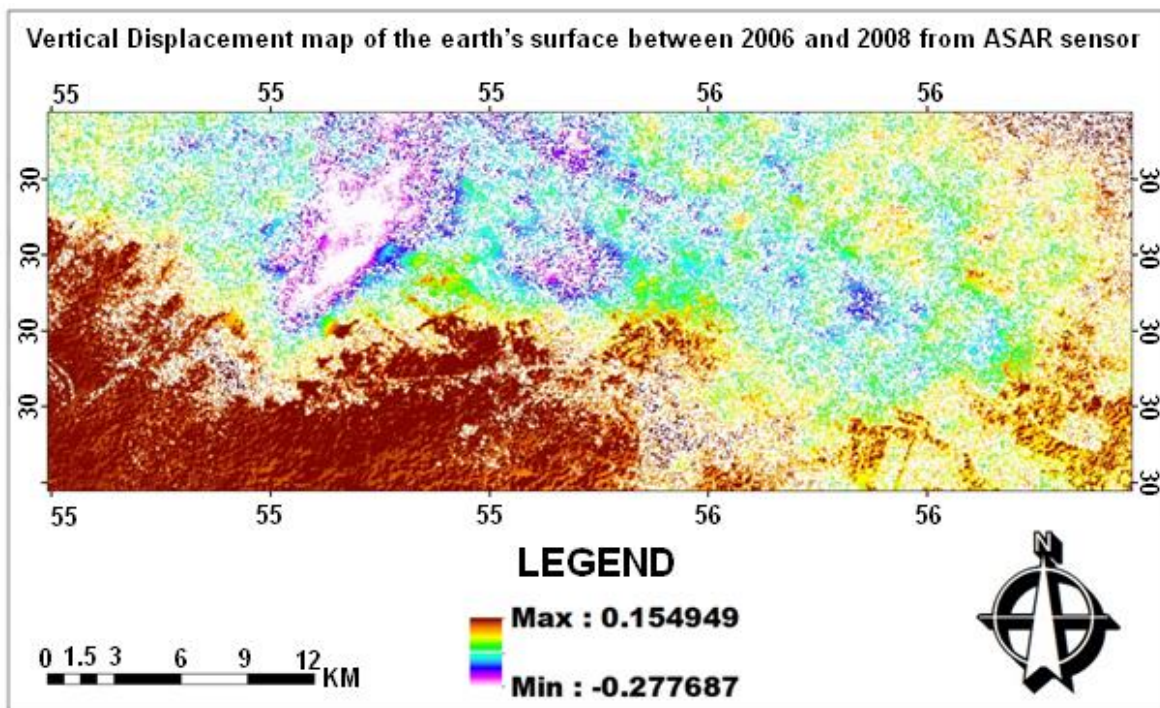

Figure 3. Displacement map

Map of the vertical displacement of the earth's surface between 2006 and 2008 from the ASAR sensor
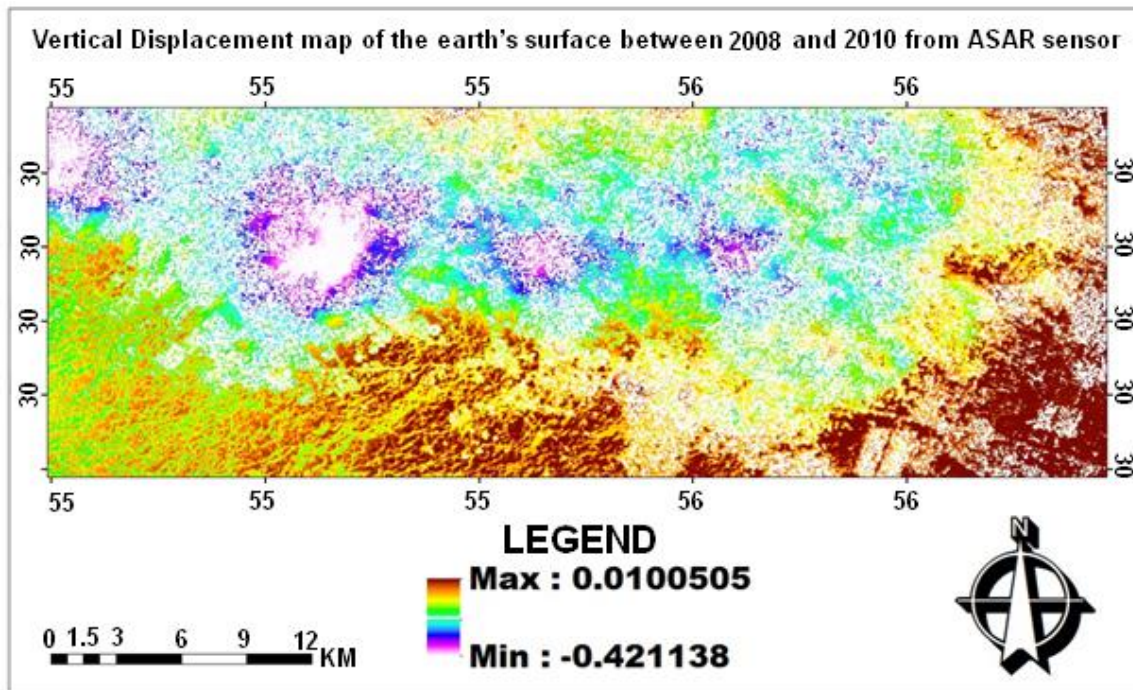

Figure 4. Displacement map

Map of the vertical displacement of the earth's surface between 2008 and 2010 from the ASAR sensor

3.2. Values of ALOS PALSARI sensor displacement

After performing the interferometric method on ALOS PALSAR images and creating interferograms and after final processing in SARCAPE software, interferograms were converted to vertical displacement values in meters. Displacement maps obtained from ALOS PALSAR in L-band have been shown in figures 5 and 6.
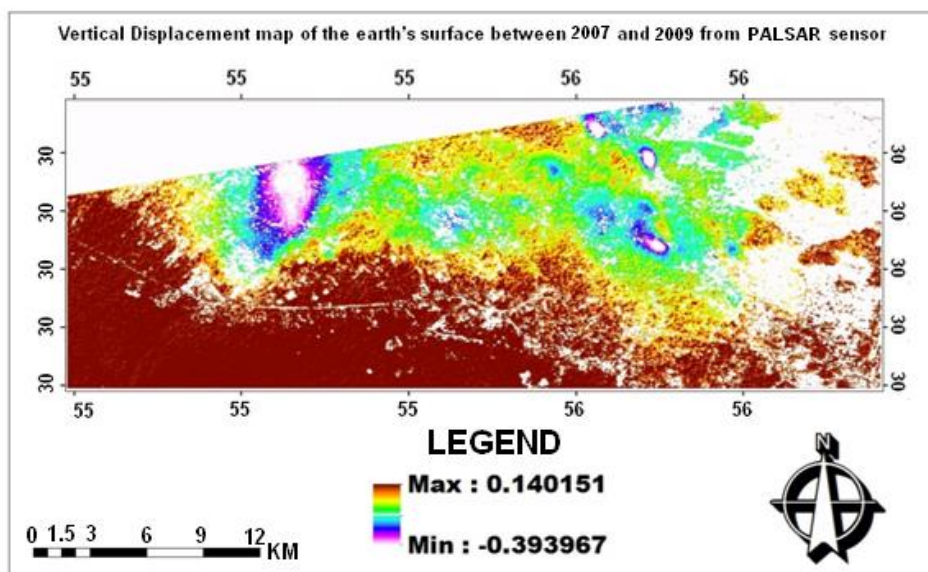

Figure 5. Displacement map

Map of the vertical displacement of the earth's surface between 2007and 2009 from the ASAR sensor
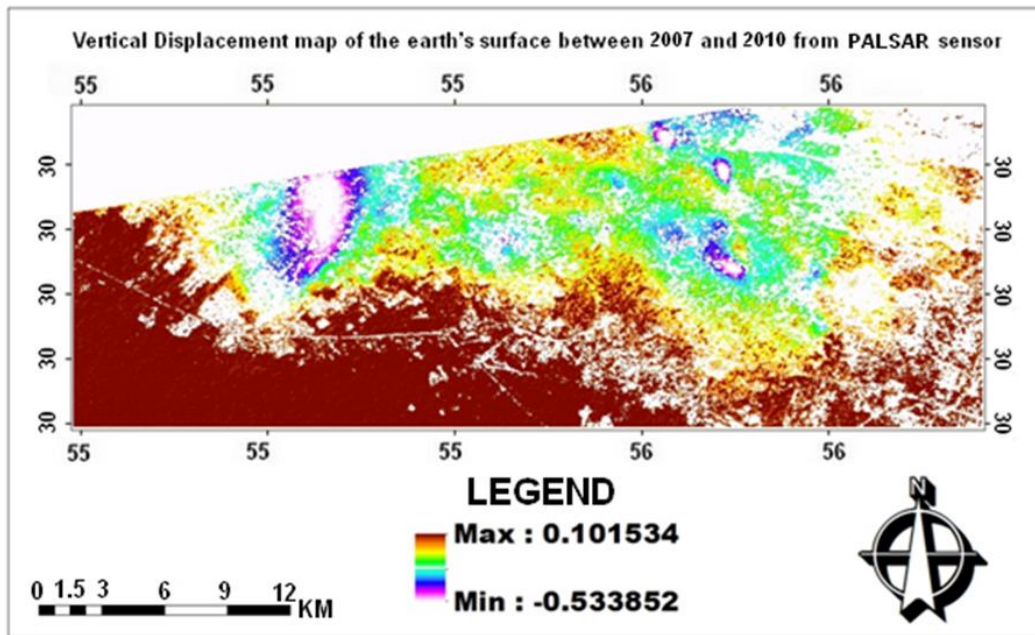

Figure 6. Displacement map

Map of the vertical displacement of the earth's surface between 2007and 2010 from the ASAR sensor

3.3. Statistical description

3.3.1. Variable of piezometric surface changes

The frequency diagram of variable of piezometric surface changes, generally and without considering the year of measurement is given below. According to diagram 2, the largest amount of groundwater extraction (piezometric surface changes) is from 2006 to 2008 with an average of 233 centimeters and its lowest amount is from 2008 t0 2010 with an average of 179 centimeters.
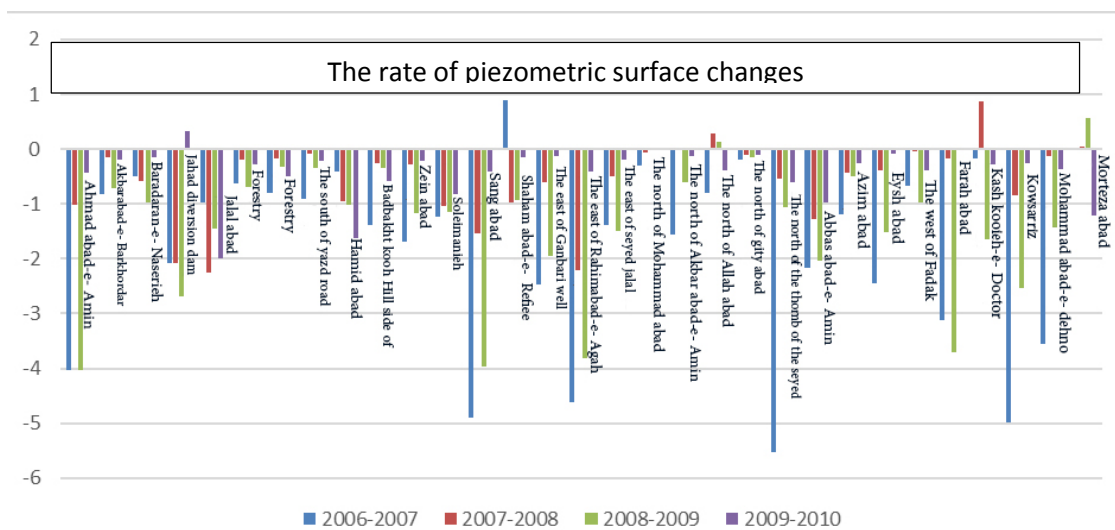
Graph 1. Variable frequency of changes in water levels in piezometric wells

Table 3. Description of the variation of changes in piezometric surface

| Number	Maximum	Minimum	Standard deviation	Average	
124	5.53	0.089	0.11224	1.0388	Underground excavation
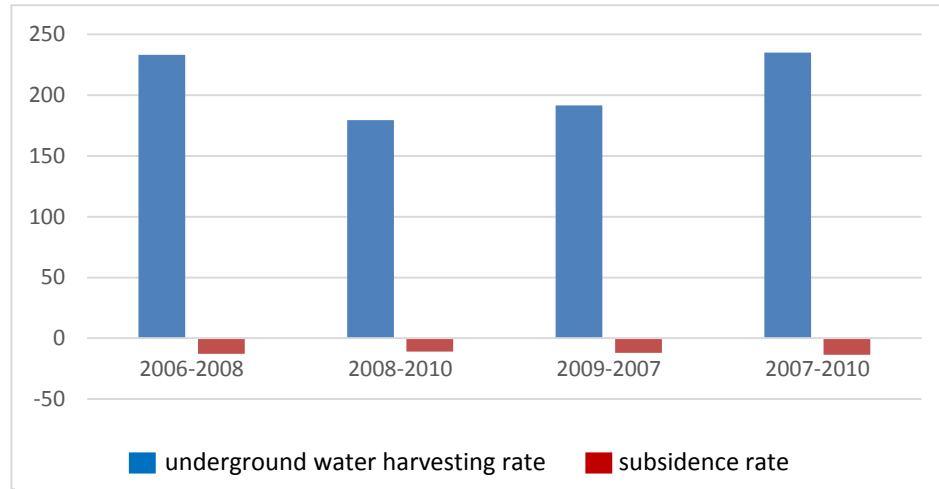
Graph 2. The mean of underground water harvesting and land subsidence variables in different years

3.4. Linear regression modeling

3.4.1. Modeling for c-band data

At first using data of the rate of well levels changes and subsidence rate obtained from synthetic radar interfrometric technique for ASAR sensor in c-band, a linear regression was created by MATLAB software. Subsidence rate was considered as a dependent variable and the amount of groundwater withdrawal (piezometric surface changes) from earth's surface was defined as an independent variable. This linear regression model was originally defined for the years 2006 to 2008, then for 2008 to 2010 and finally for 2006 t0 2010. Obtained results are shown in diagram 3. It shows a linear relationship with coefficient r^2 equal to 0.89 and RMSE equal to 0.62 which they have strong and positive correlation and this linear relationship is obtained : Y=0.035X + 4.701. In this equation X is the rate of groundwater extraction and Y is subsidence rate. The confidence level is 99 percent.
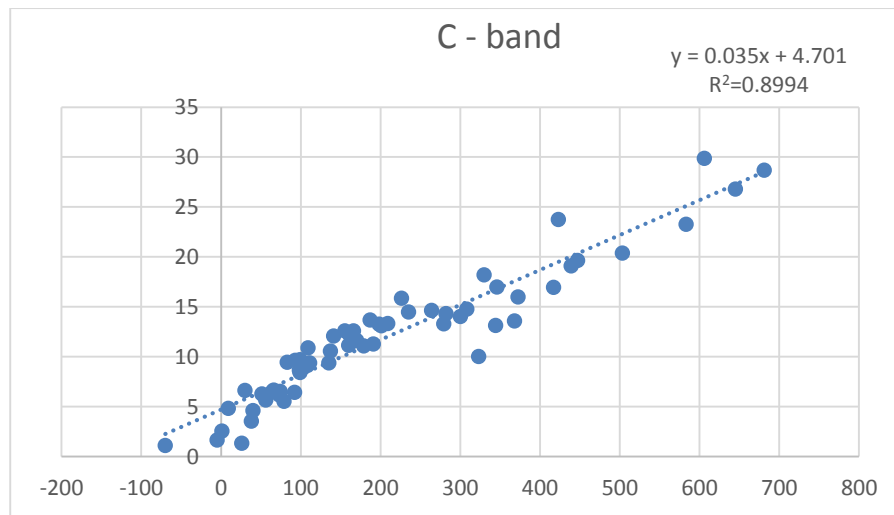
Graph 3. The correlation between underground excavation and subsidence in C- band between 2006 and 2010

3.4.2. Modeling for L-band data

Like c-band data, for PALSAR sensor data in L-band, a linear regression model was created between subsidence rate as a dependent variable and the amount of groundwater extraction (piezometric surface changes) as an independent variable by MATLAB software. This linear regression model was created at first for the years between 2007 and 2009, then for 2009 to 2010. Results are observed in diagram 4 which represents a linear relationship with r^2 equal to 0.91 and RMSE equal to 0.37 that the correlation between them is strong and positive. And this linear relationship is created: Y=0.035X+5.282 X is the amount of groundwater extraction and Y is subsidence rate. The confidence level is 99 percent.
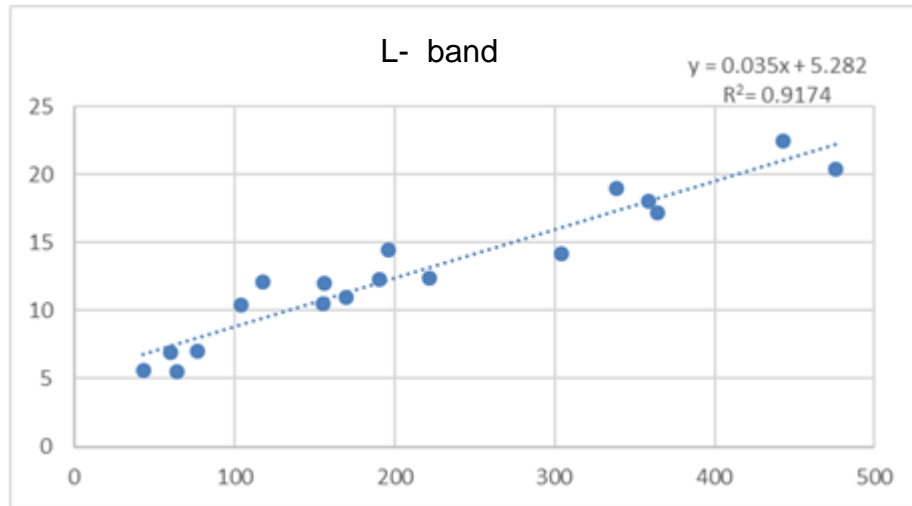
Graph 4. The correlation between underground excavation and subsidence in L- band between 2007 and 2010

4. Conclusions

From the above context, it is apparent that synthetic radar inferometric technique is suitable for determining the rate and extent of subsidence in the studied area. Environmental dryness moderated the effect of phase shift caused by atmospheric compounds especially moisture and provided an accurate measure of the phase difference caused by surface displacement. Also, lack of vegetation minimized decoherence challenge in the phase of radar images and made it possible to measure phase changes for C- and L-band data at annual intervals. This finding emphasizes the effectiveness of this method in studying changes in earth's crust in most parts of the country. Findings using this method showed that changes in piezometric surface or the amount of groundwater extraction had a close relationship with subsidence. The most important reason of subsidence in sedimentary basins in arid and semi-arid regions is falling groundwater tables because of excessive extraction of these resources. According to the results obtained by differential synthetic aperture radar interferometry method in the Rafsanjan plain, between 2005 and 2010, there were 27 to 53 centimeters of subsidence and according to the results of linear regression model, for each 4.7 centimeters decreasing groundwater levels, there was 1 centimeter subsidence. This indicates that subsidence has a direct linear relationship with the rate of groundwater extraction by human factors like agriculture etc. In order to compare this paper with other researches, Sharifikia's research (2012) entitled "Determining the rate and extent of land subsidence in the Noogh- Bahreman plain using radar data in C- and L- band between 2005 and 2010" can be mentioned as the closet research in terms of geographical situation to the studied area. average annual subsidence of about 30 centimeters in an area of 281 square kilometers in the middle part of the plain was estimated. Moreover, comparison of the rate of subsidence with water level changes extracted from piezometric wells represents that every 3.2 centimeters ground water lowering is able to create a subsidence of 1 centimeter in this plain. In another research from Heshmati and Almodaresi (2014) entitled" Modeling subsidence of the Neishabour plain using time series and

DINSAR technique", the Neishabour plain has been studied between 2003 and 2010. It is proved that the relationship between subsidence and the amount of changes in piezometric surface (groundwater withdrawal). Also they determined that for each 3 centimeters decrease of piezometric surface, there was 0.816 centimeter subsidence. The results of these two studies are very close to the results of the present research.

As mentioned at the beginning of the article, in this research, a question is raised with two hypotheses and the answers are as follows:

The answer of hypothesis 1: Since microwave ranges with long wavelength of C- and L-band have more influence and they are less affected by the atmosphere, they are suitable for studying earth's surface changes. In fact, as the wavelength increases, the penetration power goes up. And longer wavelengths pass through the surface, so they have more control over the surface and show the changes better.

The answer of hypothesis 2: According to the results of this research, the precision of correlation coefficients between changes of piezometric surface and the rate of subsidence in C- and L-band is 91 and 89 percent and it is 0.37 and 0.61 for RMSE. These results are acceptable and have a fairly good accuracy.

In response to the main research question, according to the statements above and obtained results, it is possible to model the relationship between the amount of lowering groundwater level and the rate of subsidence using linear regression model. This model for C-band data in the area studied is a linear relationship that can be written in form of: $Y=0.35X+4.701$. And for L-band data, it is a linear relationship as: $Y=0.35X+5.282$ in which X is the amount of groundwater extraction and Y is the rate of subsidence. The confidence level is 99 percent.

References

Haghighatmehr, P., Jaladanzouj, M. J., Tajik, R.,Jabari, S.,Sahebi,M. R., Eslami, R.,Ganjian, M. &, Dehghani, M. (2013). Time series analysis of Hashtgerd subsidence using Radar Interferometry and Global Position System. *Geoscience*, 22 (85), 105-114.

Paul, M. M. &Magaly, K. (2011). Computer Processing of Remotely-Sensed Images, *An Introduction.John Wiley & Sons*.

Roy, E. H. (2005). Geologic Hazards-A Field Guide for Geotechnical Engineers.*Taylor & Francis Group*.

Sharifikia, M. (2012). Determination the rate and extent of land subsidence in Noogh- Bahreman plain using radar data in C- and L- band between 2005 and 2010. *Spatial planning*, 16 (3). 55-77 .

USGS (United States Geological Survey), Research and Review Information Located, Assess on September 2011*: http://water.usgs.gov/ogw/pubs/fs00165*.

Rahnama, M. B. & Kazemifar, F. (2006). Land subsidence because of ground water level drop in Rafsanjan plain. Third congress on irrigation and drainage networks management, *Shahid Chamran university, Ahvaz* .

Heshmati, Sh. & Almodaresi, A. (2014). Modeling subsidence of Neishabour plain using time series and DINSAR technique. *First congress on application of advanced models of space analysis (Remote sensing and GIS) in testing of the land, Islamic Azad university, Yazd Branch.*

JRORS
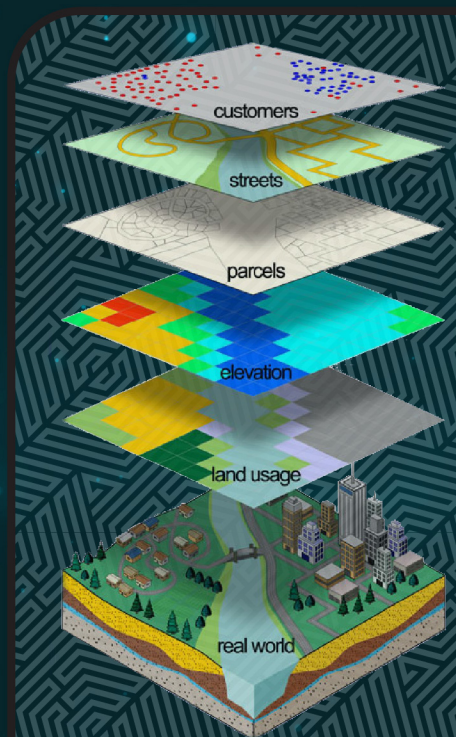## JOURNAL OF RADAR AND OPTICAL REMOTE SENSING

ISLAMIC AZAD
UNIVERSITY, YAZD BRANCH

IRANIAN ASSOCIATION OF GEOMORPHOLOGY

JOURNAL OF RADAR AND OPTICAL REMOTE SENSING

customers
streets
parcels
elevation
land usage
real world

Price: 700000 Rls